5

Testing spatial IMF variations with self-consistent dynamical modelling

Abstract

We present spatially resolved measurements of the stellar initial mass function (IMF) in three nearby early-type galaxies, using MUSE integral field spectroscopy. We carry out full spectral fitting of these data using the updated stellar population models by Conroy et al. (2018) and the spectral fitting code PyStaff by Vaughan et al. (2018). We find IMF variation to be mass dependent, with our low mass galaxy having an IMF mismatch parameter consistent with a Kroupa IMF at all radii, while our two higher mass galaxies are consistent with IMFs heavier than Salpeter at all radii. In one of these objects we find evidence of an IMF gradient, being super-Salpeter in the centre and declining to Kroupa-like in the outskirts. We calculate the stellar mass-to-light ratio (M/L) as a function of radius, accounting for spatial variations in age, metallicity and IMF. Including these measured M/L gradients in dynamical models constrained by stellar kinematics extracted from the *same* observations, has the effect of worsening the fits to the kinematics. Typically the M/L values calculated from stellar population modelling are higher than the M/L required to match the dynamics, indicating that, while the stellar population models used to account for variations in age, metallicity and IMF provide excellent fits to the spectroscopic data, systematic uncertainties in the implied mass-to-light ratios remain. Removing the exact normalisation of the M/L, but accounting for the *gradient* in M/L across our objects, allows us to reproduce the observed kinematics with similar accuracy as a conventional constant M/L approach, but has the effect of increasing the dark matter fractions derived from dynamical modelling, and also potentially decreasing the mass of the central black hole. These results highlight the difficulties remaining in stellar population modelling and the importance of correctly accounting for stellar population gradients in dynamical models.

5.1 Introduction

The stellar mass-to-light ratio M/L has long been known to vary within galaxies. Gradients in colour, as well as in spectroscopic measurements of various line indices imply gradients in stellar population properties such as age and metallicity (Barbera et al., 2005, Kuntschner et al., 2010, Peletier & Valentijn, 1989). Recent studies suggest the stellar initial mass function (IMF) may also

vary spatially within galaxies, which would further boost these M/L gradients.

The difficulty in constraining the IMF spectroscopically means that not many resolved studies have been carried out to date. Various indices exist which are differentially sensitive to giants and dwarfs, allowing constraints to be placed on the IMF. Gradients in these gravity sensitive indices have been observed, however the cause of these gradients is still hotly debated. A number of studies claim IMF gradients in the ETG population, whereby massive ETGs have bottom heavy IMFs in their centres, declining to Milky Way-like at large radii (Martin-Navarro et al., 2014, Martín-Navarro et al., 2015, Parikh et al., 2018, Sarzi et al., 2018, van Dokkum et al., 2017). However others find this variation in gravity sensitive indices is instead due to gradients in individual element abundances (Alton et al., 2017, McConnell et al., 2016, Vaughan et al., 2016, Zieleniewski et al., 2017). A further complication is the somewhat contradictory results obtained using different tracers: for example Parikh et al. (2018) obtain different results using the Wing-Ford FeH band versus using sodium Na I 8200. Understanding the competing effects of age, metallicity, abundance variation and IMF on each of the indices is a complex task, requiring the comparison of accurate stellar population models to high quality data.

In Chapter 4 we tested the effects of including spatial variation in the stellar mass-to-light ratio on the outputs of dynamical models. We measured the spatial M/L variation in our galaxies due to age and metallicity gradients, at fixed IMF, using the standard tool of full spectral fitting with pPXF. We found that neglecting these M/L gradients did not bias the dynamically-derived properties. However, when also including the M/L variation which would be caused by the IMF gradients observed by van Dokkum et al. (2017, hereafter VD17), we find a strong effect on the derived dark matter fractions and black hole masses. We also find that if we take the M/L normalisation at face value, the kinematics strongly disfavour this level of IMF variation. However, the investigation in Chapter 4 was limited to considering fiducial variations in M/L taken from other studies, rather than from our data itself.

Here, we perform a self-consistent analysis, where we measure M/L gradients due to age, metallicity *and IMF* directly from the same data from which we extract the kinematics. Due to the high quality of our MUSE spectroscopy, we can obtain spatially resolved maps of various stellar population properties, including IMF. The extended spectral range of MUSE includes IMF sensitive features such as Na 8200, TiO2 and the calcium triplet CaT, as well as the classic optical features Hβ and [MgFe] to constrain age and metallicity. Critically, it also contains Na D, which allows us to constrain sodium abundance, crucial when using Na 8200 to probe the IMF (Spiniello et al., 2012). Having measured M/L gradients due to age, metallicity and IMF, we can incorporate this variation into our dynamical models, and analyse the effects.

This chapter is laid out as follows: in Section 5.2 we describe the fitting procedure we use to derive stellar population properties of our galaxies. In Section 5.3 we measure radial profiles of various stellar population properties, and convert these into radial profiles of the stellar M/L, which we incorporate into dynamical models in Section 5.4. In Section 5.5 we discuss the implications of our findings.

5.2 Full spectral fitting using PyStaff

We carry out full-spectral fitting of our MUSE cubes using the PYTHON package `pystaff` (PYTHON Stellar Absorption Feature Fitting[1] (Vaughan et al., 2018). PyStaff uses the most updated version of the stellar population models by Conroy et al. (2018, hereafter C18). These models make spectral predictions covering the full optical to near-infrared wavelength range (0.37-2.4 μm) for old ages (1-13.5 Gyr) and a wide range of metallicities ($-1.5 <$ [Fe/H] < 0.3). They are also available for

[1]available at https://github.com/samvaughan/PyStaff

a large number of different initial mass functions, while also allowing for variation in individual element abundances.

The C18 models use the MESA Isochrones and Stellar Tracks (MIST; Choi et al., 2016, Dotter, 2016), a new comprehensive set of stellar evolutionary tracks and isochrones. The MIST isochrones cover all relevant evolutionary phases, and have been extensively tested against observational constraints (Baldwin et al., 2017, Choi et al., 2016). The high-quality empirical spectral libraries used are MILES for the optical (Cenarro et al., 2007, Falcón-Barroso et al., 2011, Sánchez-Blázquez et al., 2006) and the extended IRTF library for the near-infrared (Villaume et al., 2017), both of which are smoothed to a common dispersion of $\sigma = 100$ km/s. Elemental response functions are computed for each age and metallicity using the ATLAS and SYNTHE model atmosphere and spectrum synthesis package (Kurucz, 1970, 1993), assuming a Kroupa IMF. These theoretical response functions are computed for 19 individual elements.

PyStaff fits this suite of stellar population models to an input spectrum using the affine-invariant Markov Chain Monte Carlo PYTHON package `emcee`[2] (Foreman-Mackey et al., 2013). The complete parameter space consists of 39 parameters. These include the recession velocity v_{syst} and velocity dispersion σ; the stellar age t and stellar metallicity $[Z/H]$; abundance variations for 19 individual elements[3], including Ca, Na, and Ti, which are important for constraining the IMF in our wavelength range; the kinematics and strengths of the emission lines Hα, Hβ, NII, SII, OIII and OI; four parameters relating to the sky subtraction; a parameter for rescaling the size of the error bars; and finally, two low-mass IMF slopes x_1 and x_2. The IMF is parametrised as a three-part power law following Equation (5.1):

$$\xi(m) = \begin{cases} C_1 m^{-x_1}, & 0.08\mathrm{M}_\odot \leq m < 0.5\mathrm{M}_\odot \\ C_2 m^{-x_2}, & 0.5\mathrm{M}_\odot \leq m < 1\mathrm{M}_\odot \\ C_3 m^{-2.3}, & 1\mathrm{M}_\odot \leq m < 100\mathrm{M}_\odot \end{cases} \tag{5.1}$$

such that x_1 and x_2 fix the low-mass slopes of the IMF, the high mass slope is fixed to Salpeter, and the normalising constants C_i are chosen to ensure that the IMF is always continuous.

We wish to find the free parameters which best reproduce the full MUSE spectrum for each of our Voronoi bins. Within `emcee`, we initialise the walkers in a ball around our input guess at the model parameters, which, where possible, are taken from our pPXF fits of these spectra (see Chapter 3). The (flat) priors on each parameter (given in Appendix C) are set to restrict the regions explored by the walkers to the values covered by the stellar population models, so that we do not extrapolate outside the region where we can make an accurate model.

The main steps in the fitting process are as follows: first we log rebin the galaxy and template spectra to have the same, constant velocity step. We then set up interpolators for the log-rebinned templates, so that we can create a model template for any arbitrary values of age, metallicity, IMF, and abundances. This model template is convolved with a Gaussian LOSVD of width σ and velocity v_{syst}. The galaxy spectrum is split into four regions, each of which is fit simultaneously. The wavelength ranges we fit between are 4750 – 5600 Å, 5600 – 6800 Å, 6800 – 7200 Å and 8100 – 8700 Å. Flux calibration differences between the data and model are accounted for by fitting multiplicative Legendre polynomials to the ratio of the data and model.

For any arbitrary set of parameters θ, the result is a continuum-corrected template spectrum, convolved with a particular LOSVD, which we compare to the input spectrum D according to

$$\ln p(\theta|D,\sigma) = -\frac{1}{2}\sum_\lambda \left[\frac{(D_\lambda - f(\theta)_\lambda)^2}{s_\lambda^2} + \ln(2\pi s_\lambda^2) \right] \tag{5.2}$$

[2]available at https://github.com/dfm/emcee

[3]the full list of elements is: Na, Ca, Fe, C, N, Ti, Mg, Si, Ba, O, Cr, Mn, Ni, Co, Eu, Sr, K, V, and Cu

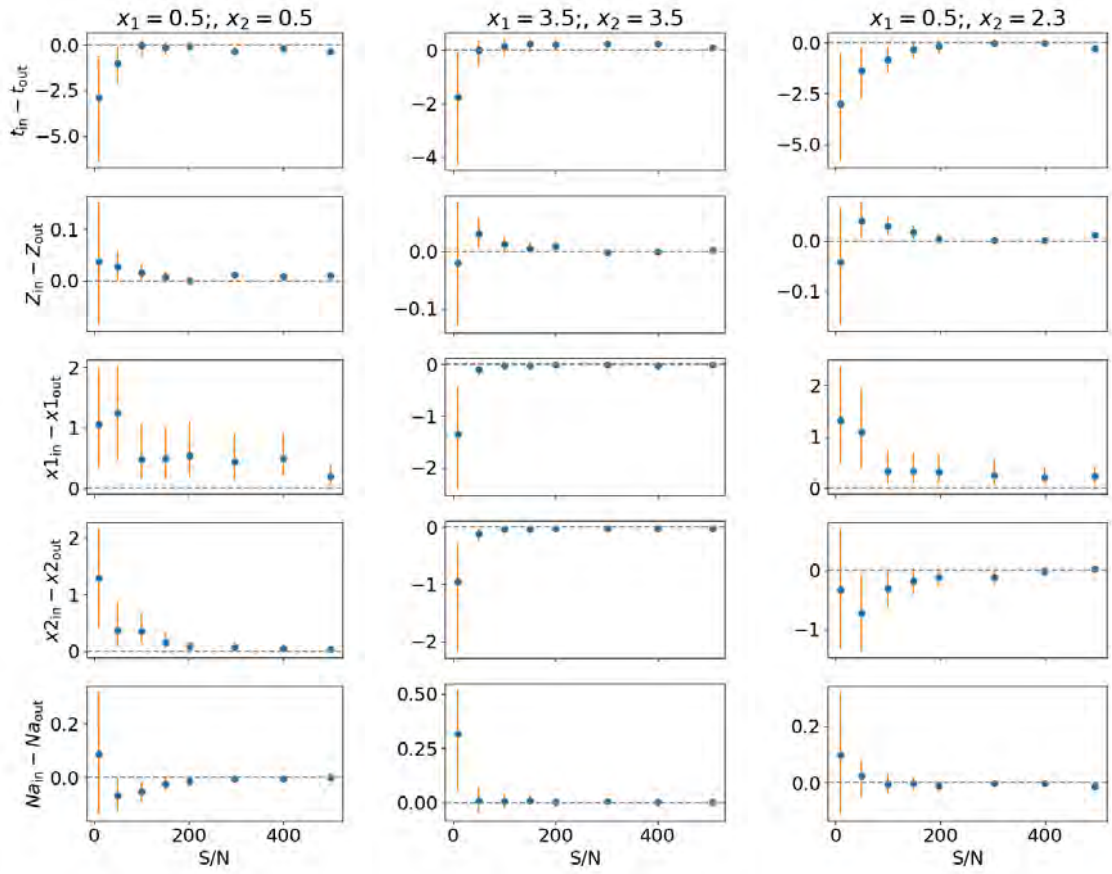

Figure 5.1: Mock tests: Comparison of the input versus the recovered parameters for three input spectra with different IMFs. Left: a bottom-light IMF with low mass slopes x_1=x_2 = 0.5; Middle: a bottom-heavy IMF with low mass slopes x_1=x_2 = 3.5; Right: x_1 = 0.5, x_2 = 2.3

where $s_\lambda^2 = (i + e^\beta) \times \sigma_\lambda^2$ allows the the variance spectrum (σ_λ^2) to be rescaled using the free parameter β. A more detailed description of PyStaff is given in Vaughan et al. (2018).

We carry out the fits to our Voronoi binned galaxy spectra using 400 walkers, each of which takes 5000 steps. We discard the first 4000 steps as burn-in, in order to remove any reliance on the initial positions. We inspect the trace to ensure convergence. For a number of arbitrarily chosen bins, we also run the MCMC multiple times with different starting values, as well as running for many more steps (20,000 steps, with 15,000 discarded as burn-in), and verify that our results are unchanged.

5.2.1 Monte Carlo Simulations

In order to determine which signal-to-noise ratio (S/N) is required to recover our parameters of interest, we carry out Monte Carlo simulations which test PyStaff's ability to recover known properties of mock data. To this end, we generate mock spectra of various signal-to-noise ratios (S/N) using the C18 models, and then attempt to recover the input properties using the full set of C18 templates. We are mostly interested in the recovery of the low-mass IMF slopes x_1 and x_2 from our (old, approximately solar metallicity) galaxy spectra. We thus generate three different sets of mock spectra: the first set have $x_1 = x_2 = 0.5$, (i.e. a bottom-light IMF with both low-mass slopes equal); the second set have $x_1 = x_2 = 3.5$ i.e. a bottom-heavy IMF with both low-mass slopes equal); and the third set have $x_1 = 0.5; x_2 = 2.3$. All have age $t = 13.5$ Gyr, and solar metallicity.

In Figure 5.1 we show the results. For the three cases, we plot the age, metallicity, IMF slopes and sodium abundance at various S/N. Age, metallicity and elemental abundances are typically

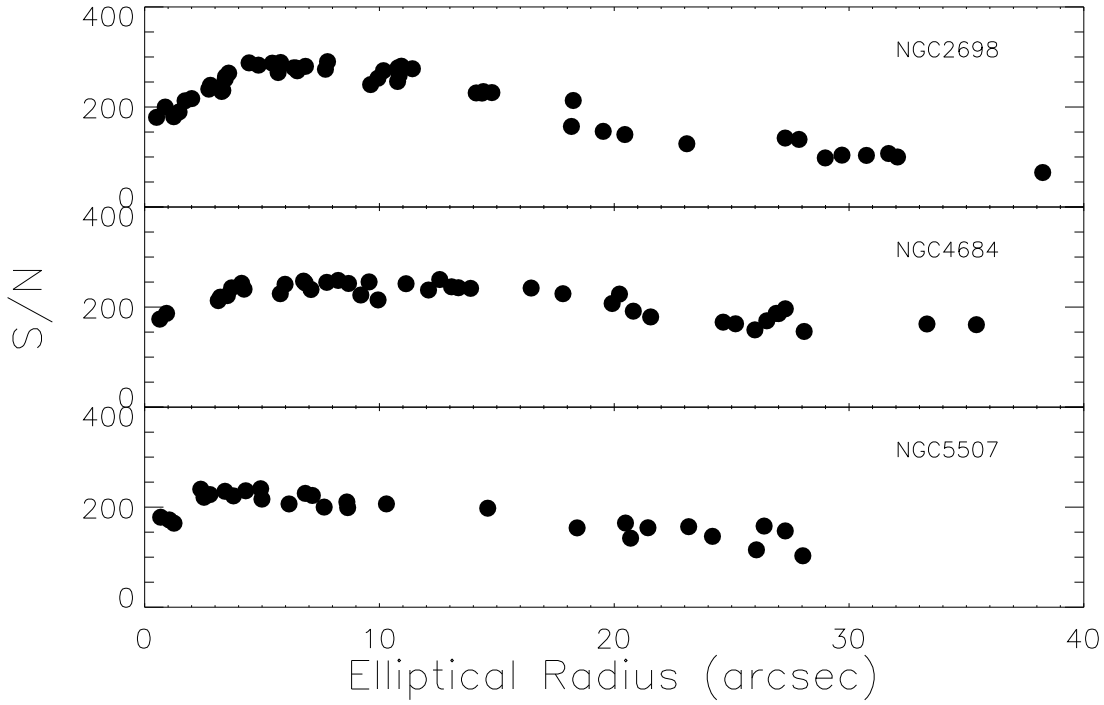

Figure 5.2: Empirically measured signal-to-noise (S/N) as a function of radius, calculated from full spectral fitting using pPXF. S/N is calculated as the ratio of the median flux to the standard deviation of the residuals from the best fitting model. Plotted against the same elliptical radius as in previous chapters.

recovered well, except at the very lowest S/N (S/N=10). We see that if the IMF is bottom-heavy, both x_1 and x_2 can be more easily recovered at all S/N. This is likely due to the fact that the signature of the low-mass dwarfs would be more pronounced for a very bottom-heavy IMF. If the IMF is bottom-light, it is more difficult to constrain, especially in the lowest mass range (x_1), which makes sense because these lowest mass stars contribute so little to the light. In the extremely bottom-light case ($x_1 = 0.5$), there is a bias in the recovery of x_1 at low S/N, in that it tends to be higher than the input value. As our sample is selected from the ATLAS^{3D}survey, they already have dynamically determined IMF mass normalisations (Cappellari et al., 2013a,b, McDermid et al., 2015), all of which are consistent with being heavier than Kroupa ($x_1 = 1.3$, $x_2 = 2.3$). As such, we do not expect the bias in recovering extremely light IMFs to affect our results.

5.3 Recovering the IMF from spatially resolved IFU data

We Voronoi bin our MUSE spectra to a target S/N of 200 in order to carry out a spatially resolved analysis of the IMF in these objects. As we show in Section 5.2.1, we are typically able to recover our parameters of interest at this S/N unless the IMFs are extremely bottom-light, which we do not expect for our galaxies, given their velocity dispersions, and dynamically measured IMF normalisations. We show the empirically measured S/N of our spectra in Figure 5.2, which we calculate as the ratio of the flux in each spectrum to the standard deviation of the residuals from full spectral fitting.

For each galaxy, we show an example fit to one of our Voronoi bins (Figure 5.3). The spectra are all well fit, with residuals typically on the order of 1% across the whole spectral range. Further fits are given in Appendix C for every 10th spectrum, ordered by radius. We show the posterior

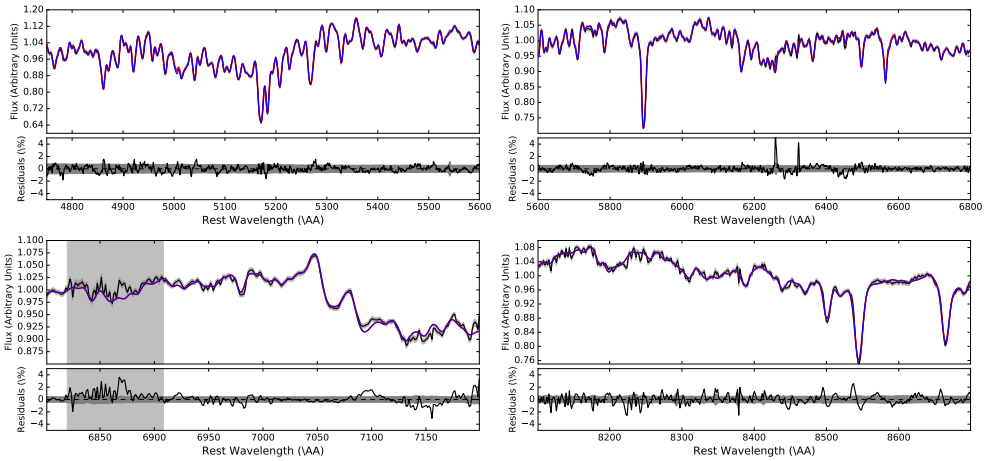

(a) NGC2698

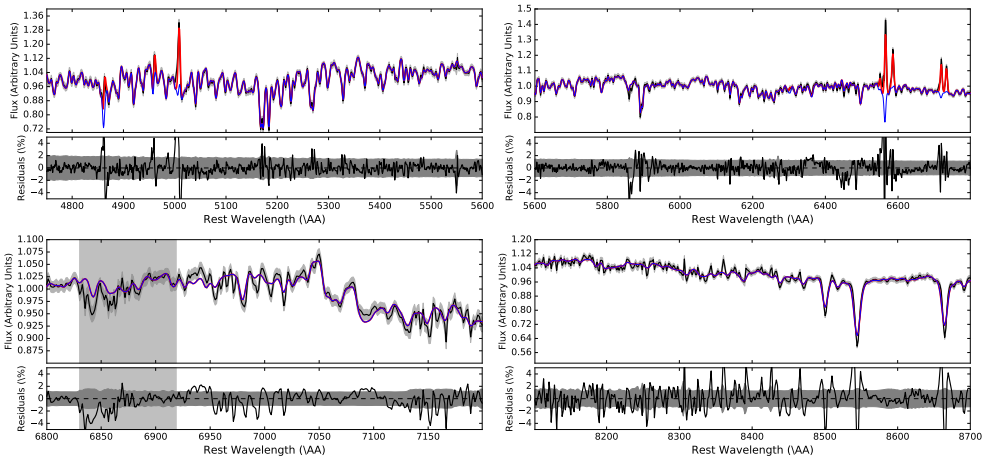

(b) NGC4684

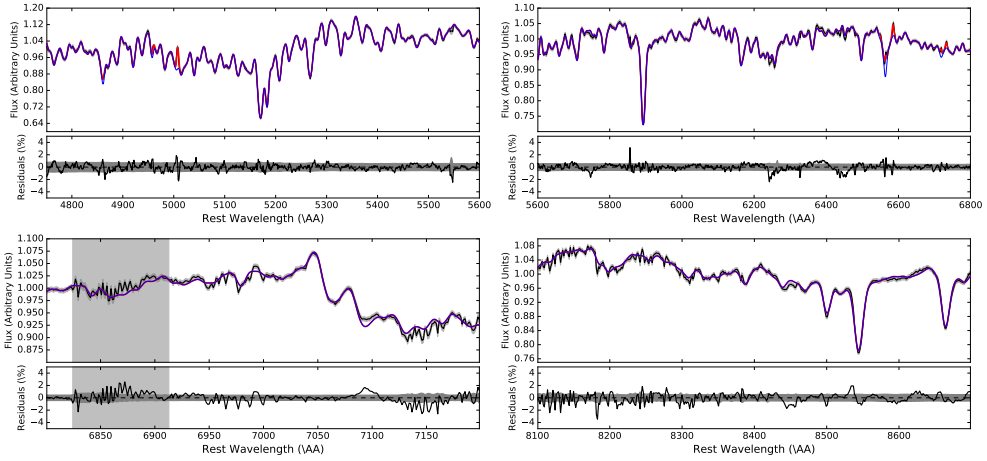

(c) NGC5507

Figure 5.3: Example Voronoi binned spectra (black) and best fitting stellar models (blue). Ionized gas emission is included in the fit and is shown in red. The residuals are shown beneath each panel. Shaded light grey boxes show regions of strong telluric contamination which are excluded from the fit.

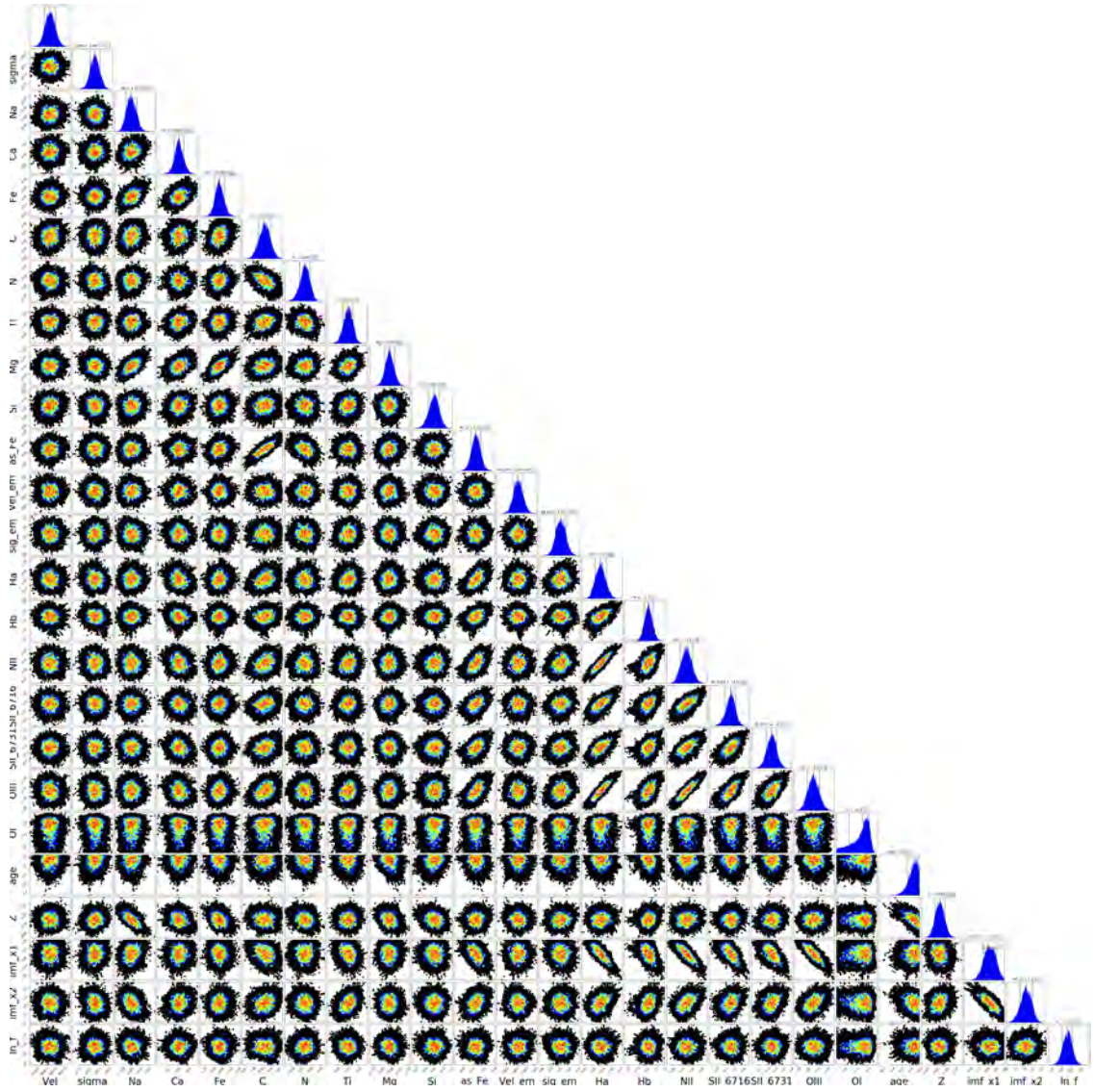

Figure 5.4: The posterior distribution for a single Voronoi bin from NGC 5507. Parameters are all well constrained except for the strength of the OI emission line.

distribution for one representative spectrum from NGC 5507 in Figure 5.4, to illustrate the extensive parameter space explored. Typically we find most parameters to be well constrained. Some covariances exist between parameters : the most obvious are the correlations between the two IMF slopes x_1 and x_2, the known degeneracy between age and metallicity, a correlation between the IMF slopes with age and metallicity, as well as a correlation between C and "as_Fe" (as_Fe gives the combined abundance of O,Ne and S). Interestingly, some emission lines (Hα, Hβ, NII, SII, OIII) are also correlated with one another, and with the lowest mass IMF slope x_1, however for most bins, the emission fluxes are negligible. Many of the parameters are nuisance parameters which are of no interest in this study, but are useful to include to explore the degeneracies and additional uncertainties they may cause. Due to the large number of parameters in the model, we plot the posterior distributions only for those parameters which we use to calculate our stellar population estimates of M/L, which is the focus of this chapter (i.e. the age, metallicity, and the two low-mass IMF slopes). These corner plots can also be found in Appendix C for each 10th spectrum. For completeness, we tabulate the best fitting values of age, metallicity, and IMF slopes, as well as the abundance of a number of elements which contribute in the MUSE wavelength range. We also include radial profiles of a number of these elements. These can all be found in Appendix C.

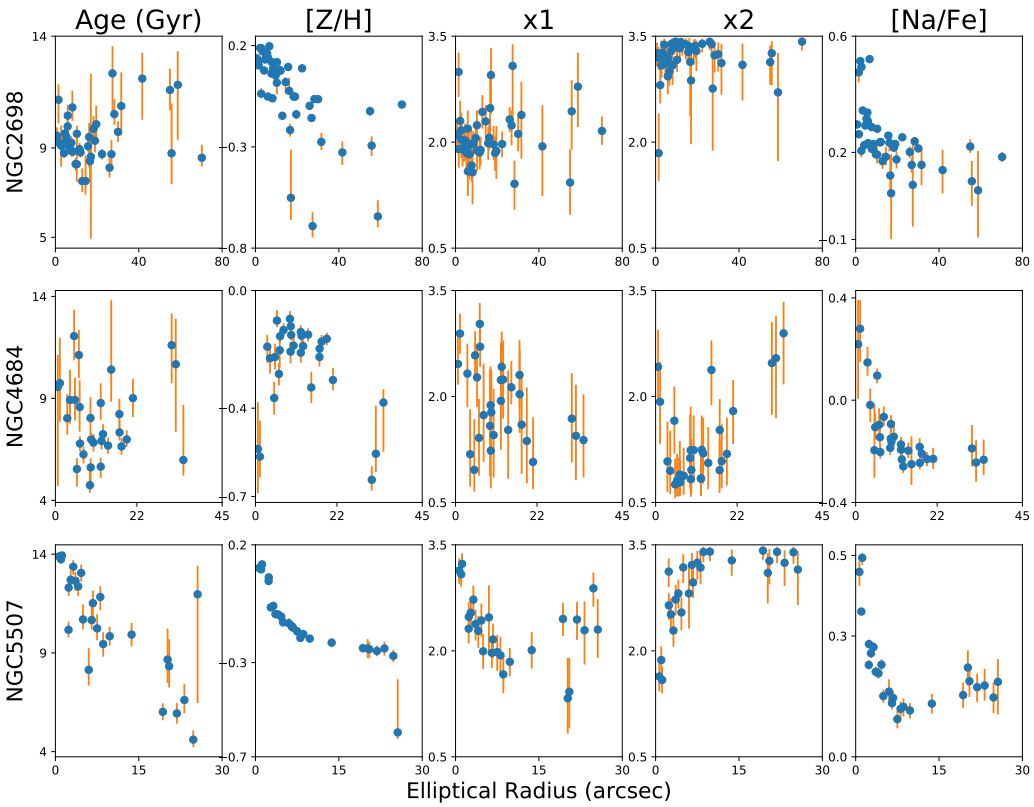

Figure 5.5: Radial profiles in age, metallicity, the two low-mass IMF slopes x_1 and x_2, and sodium abundance for NGC 2698 (top), NGC 4684 (middle), and NGC 5507 (bottom).

5.3.1 Radial profiles

In Figure 5.5 we show the radial profiles of the age, metallicity, IMF slopes, and sodium abundance. The errors on these parameters are the 16th and 84th quartiles of the MCMC output. All galaxies display strong negative gradients in their metallicity and sodium abundance. NGC 5507 also has a strong negative age gradient, and clear gradients in x_1 and x_2, which display opposite behaviour to one another in that x_1 decreases with radius while x_2 increases.

Given the best fitting values of age, metallicity and the two low mass IMF slopes for every Voronoi bin, we can also compute the M/L as a function of radius. x_1 and x_2 are the slopes of the IMF between $0.08 - 0.5\mathrm{M}_\odot$ and $0.5 - 1\mathrm{M}_\odot$ respectively, while the IMF slope above $1\mathrm{M}_\odot$ is fixed to the Salpeter value of 2.3. Given the three IMF slopes, we first calculate the mass associated with each population by integrating under this function. We then generate a model spectrum of the best-fitting age, metallicity and IMF, and integrate this spectrum within the SDSS r-band filter to obtain the luminosity of the best-fitting population. We calculate errors on M/L by randomly sampling the age, metallicity and IMF slopes 500 times within the errors, and recalculating M/L. We show these M/L profiles in Figure 5.6, along with the M/L one would obtain for a galaxy with the same best-fitting age and metallicity, but a Milky-Way like (Kroupa) IMF, and the IMF mismatch parameter α, which is the ratio of these two values.

NGC 2698 and NGC 4684 do not show clear profiles in their M/L, due to the large scatter in their ages and IMF slopes. NGC 5507, on the other hand, displays exactly the strong M/L gradient seen by VD17 (see their Fig. 10, bottom right panel) in their sample of six galaxies, due to the obvious gradients in age, metallicity and IMF slopes. The IMF mismatch parameter α is 2.40 ± 0.5

in the centre of NGC 5507, indicating an IMF heavier than Salpeter, and very similar to the central value obtained by VD17 in their sample. This gradually decreases with radius, remaining heavier than Salpeter out to about 1 R_e. NGC 2698 has a mismatch parameter consistent with an IMF heavier than Salpeter at all radii, while NGC 4684 is consistent with a Kroupa IMF at all radii.

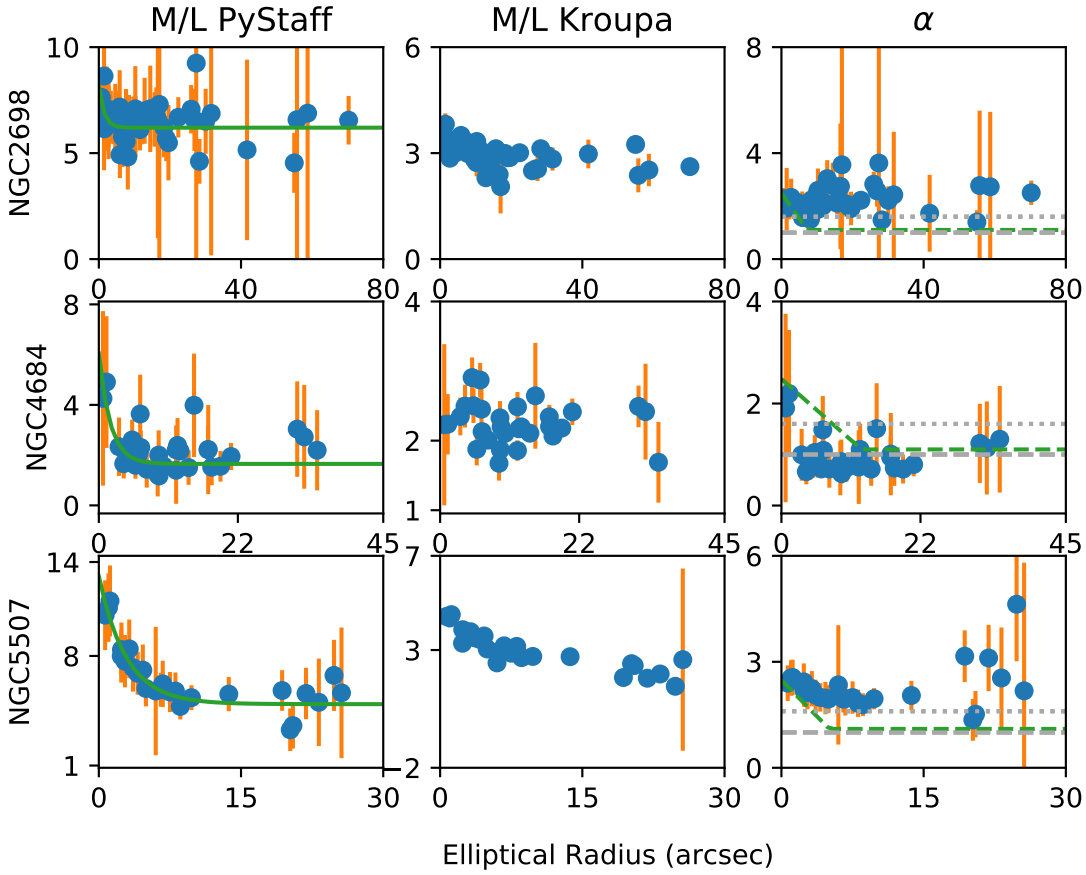

Figure 5.6: Radial profiles in the mass-to-light ratio calculated from the best fitting age, metallicity and IMF obtained from full spectral fitting with PyStaff (left); M/L calculated from the best fitting t, Z but assuming a Kroupa IMF (middle); and the IMF mismatch parameter $\alpha = (M/L)/(M/L_{\rm Kroupa})$. We fit profiles to our derived M/L (first column, green). The α profile measured by VD17 is also shown (final column, green) plus the values of the mismatch parameter for Salpeter and Kroupa IMFs (grey dashed lines).

5.4 Utilising our measured M/L in dynamical models

Now that we have measured the M/L as a function of age, metallicity and IMF directly from the data, we are in a position to revisit the dynamical modelling we carried out in the previous chapter. In the same way we did in Section 4.3.3, we fit a profile to our M/L values (shown in the left column of Figure 5.6). We then multiply our SDSS imaging by this profile, and refit an MGE to the "mass image" as done in Section 4.3.3. The mass MGEs are plotted and tabulated in Appendix C. We then use this as input to our JAM modelling. Similar to our model (e) in Chapter 4, we parametrise the stars using this stellar mass MGE, the dark matter as a spherically-symmetric NFW halo, and our mass model is the sum of these two components, plus a point mass black hole. In what follows, we adopt two approaches. Firstly, we assume that the absolute stellar mass inferred from PyStaff is accurate, and thus the only free parameters in the mass model are

dark matter fraction and black hole mass. How well such a model can fit the kinematics will inform us on the accuracy of the masses inferred from stellar population fitting when including a variable IMF. In the second approach, we allow the stellar mass to be re-scaled when fitting the kinematics. This allows us to evaluate if an additional normalisation correction is required and how large it is. Furthermore, by comparing the quality of fit to that of a conventional JAM model with no assumed spatial M/L variations, we can explore whether the additional information on the radial stellar M/L from spectral fitting improves the dynamical model fit, or not.

5.4.1 Building self-consistent dynamical models

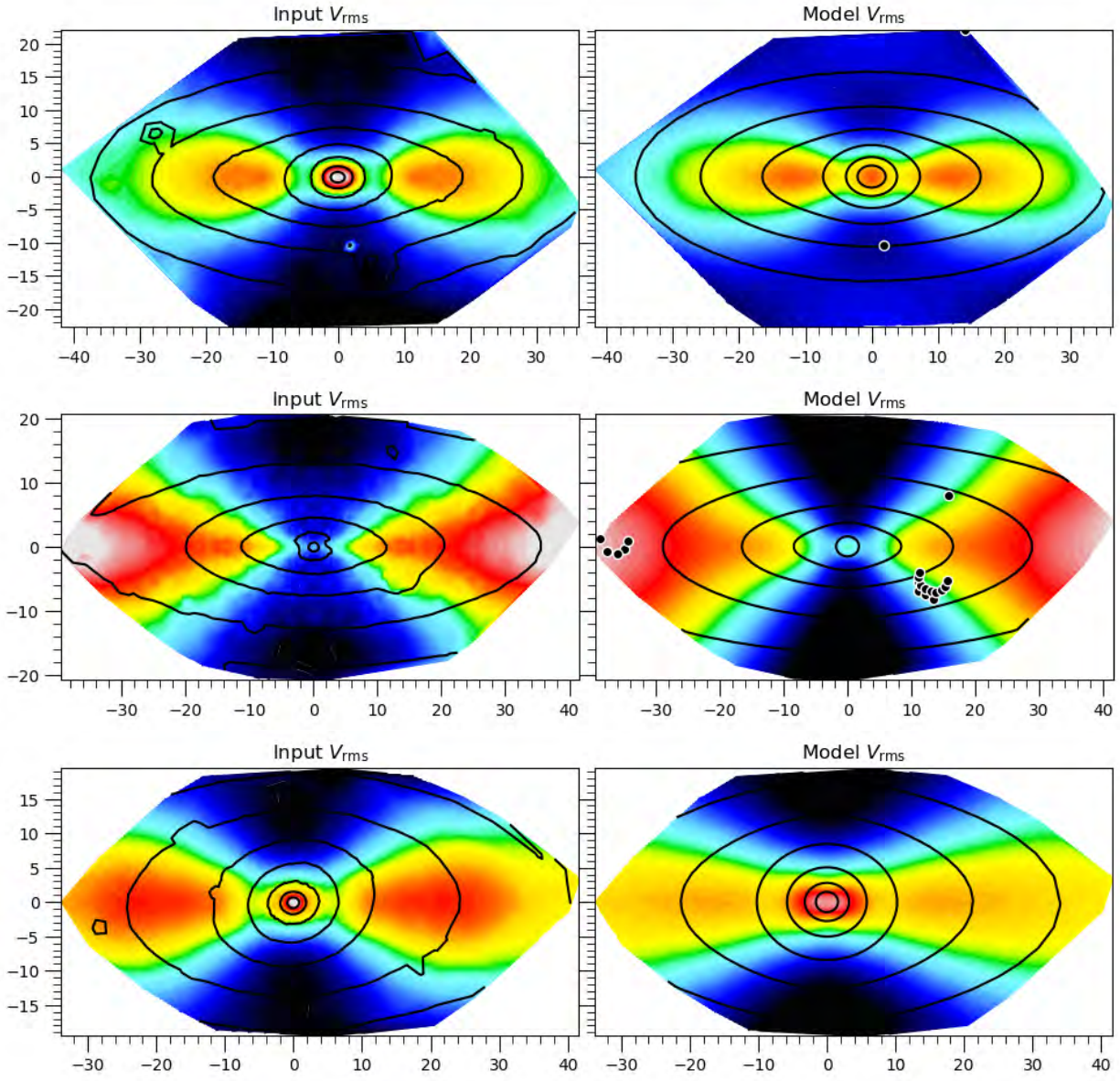

Figure 5.7: Comparison of the observed $V_{\rm rms}$ (left) with the best fitting model $V_{\rm rms}$ (right) for NGC 2698 (top) NGC 4684 (middle) and NGC 5507 (bottom). The mass model is made up of an NFW halo with fixed inner slope $\gamma = -1$, a black hole of mass mbh, and the stellar mass model, which is created by scaling our SDSS imaging by our fitted M/L values and fitting an MGE to the resulting "mass image". No re-scaling of the stellar mass is applied in the model fit.

We begin by comparing the JAM models to the data under the assumption that the stellar mass is completely understood due to the measurement of M/L from the data. The reduced $\chi 2$ values

and best fitting properties are given in Table 5.1, along with the results of the mass follows light (model a) and stars+NFW halo (model b) case from Chapter 4 for reference. (We briefly remind the reader of the benchmark models from Chapter 4: model b explicitly accounts for dark matter, meaning that the tabulated value of M/L for this (our benchmark model) is that which is allocated solely to the stars. Model a accounts for dark matter as well, it simply assumes that the dark matter distribution exactly follows the light distribution. This $M/L_{\rm dyn}$ then, is the *total* M/L, including both the stars and dark matter, i.e. our benchmark model gives the stellar M/L derived from the dynamics, while the mass follows light case gives the dynamically-derived upper limit on the M/L, which is due to the stars plus any dark mass present, such as dark matter or a black hole.)

In Figure 5.7 we compare the observed $V_{\rm rms}$ to the kinematics predicted by the JAM models. The model $V_{\rm rms}$ predicted for NGC 2698 and NGC 4684 both appear qualitatively similar to the observed $V_{\rm rms}$, although there are discrepancies - in particular, the model for NGC 2698 does not reproduce the drop between the central peak and outer lobes (although this is common to previous models), and in NGC 4684 the low $V_{\rm rms}$ in the outskirts extends too far in towards the centre. However NGC 5507, with its strong M/L gradient, is clearly unable to reproduce the observations with this mass model, borne out by the $\chi 2$ given in Table 5.1, which is a factor 5 worse than the benchmark model.

In Figures 5.8 to 5.10 we show the resulting posterior distributions for the three galaxies. We see that NGC 2698 and NGC 5507 require minimal dark matter and very light black holes compared to previous models. Comparing the M/L profiles shown in Figure 5.6 with the mass scalings applied by JAM in the benchmark and mass follows light case explains this. NGC 2698 has a largely flat $M/L(t, Z, \Gamma)$ profile, with typical values of approximately 6.2. This is $\approx$ 30% higher than the (constant) inferred stellar M/L of 4.5 allocated to the stars in the benchmark case, but only $\approx$ 5% higher than the total M/L derived in the mass follows light case (Table 5.1), explaining why the model is still able to provide a relatively good fit to the kinematics for this galaxy, as long as it does not include any dark matter. NGC 4684's $M/L(t, Z, \Gamma)$ profile is largely flat, except for the central few arcseconds, with values of $M/L \sim 2$, which is similar to the inferred stellar M/L derived by JAM in the benchmark model (model b). In the case of this galaxy, the best-fitting JAM model can compensate for the increased central stellar mass by lowering the mass of the black hole, while maintaining a similar dark matter fraction to the benchmark case. NGC 5507 has $M/L(t, Z, \Gamma)$ values approximately 5-6 in the outskirts, similar to the *total* M/L of 6.3 in the mass follows light case. However, this galaxy has a very steep gradient within 5″, reaching central values of $\approx$13 (3 times the constant stellar M/L derived in the benchmark case, and still twice the M/L assumed even including contributions from dark matter or a black hole) explaining why this model does not do a good job at reproducing the observations. We can infer from this and the model kinematics that the stellar mass is too high in the centre, causing JAM to prefer negligible dark mass in order to not overpredict the central $V_{\rm rms}$ even further. However, this lack of dark matter causes the best-fitting model to underpredict the $V_{\rm rms}$ at large radii, where dark matter could contribute a larger fraction of the mass. We explore this more quantitatively in the next section, where we allow JAM to rescale the stellar mass, and study the effects.

5.4.2 Rescaling the stellar mass

If we assume the slope of the $M/L(t, Z, \Gamma)$ profile to be correct, but allow for systematic errors in the overall normalisation, we can allow JAM to re-scale the stellar mass profile, as we did in Chapter 4 in the case of model (d). That is, our total mass model is made up of a spherical NFW halo; a central black hole; and our model of the stellar mass, where the stellar mass model is obtained by multiplying our SDSS imaging by the $M/L(t, Z, \Gamma)$ profile from PyStaff, and then *re-scaling* this stellar mass model in order to best reproduce the galaxy kinematics. The free parameters of this model are i, β, α_*, $f_{\rm DM}$ and mbh, where α_* is the scaling applied to the stars.

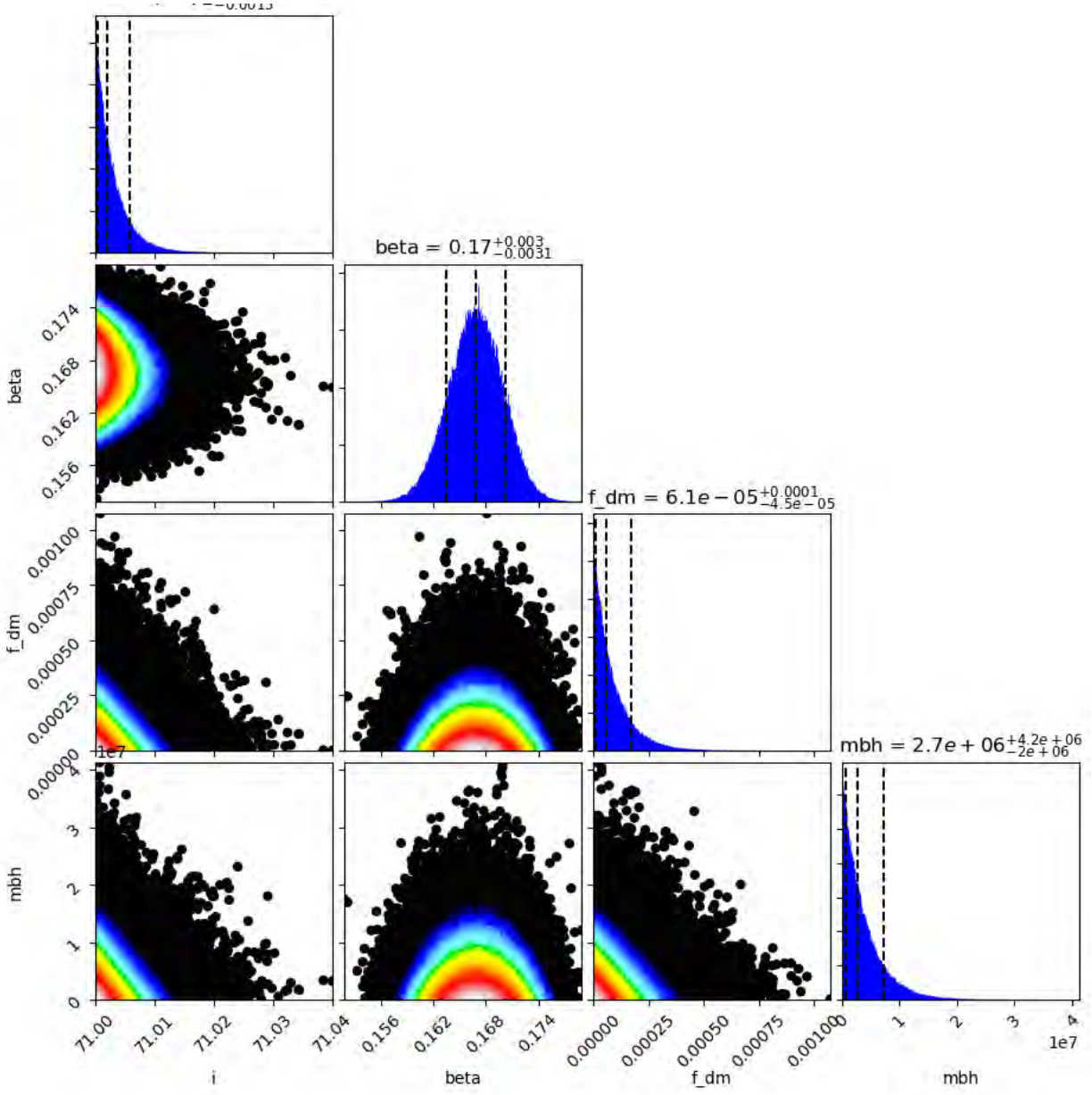

Figure 5.8: The posterior distribution of the JAM modelling presented in Figure 5.7,for NGC 2698. The mass model is made up of an NFW halo with fixed inner slope $\gamma = -1$, a black hole of mass mbh, and the stellar mass model, which is created by scaling our SDSS imaging by our fitted $M/L(t, Z, \Gamma)$ values and fitting an MGE to the resulting "mass image".

In Figure 5.11 we compare the resulting kinematics with the data. We see from the kinematics and the reduced $\chi 2$ values given in Table 5.1 that the rescaled models are able to reproduce the data well, typically giving very similar results to our benchmark (constant M/L) case in terms of goodness of fit.

We show the posterior distributions in Figures 5.12 to 5.14. The stellar mass is always scaled down ($0 < \alpha_* < 1$), confirming our inference that the stellar mass was too heavy to match the kinematics (i.e. that the $M/L(t, Z, \Gamma)$ values used to convert light into mass were too high). As described above, we see that for NGC 4684, the $M/L(t, Z, \Gamma)$ values measured by PyStaff were not too far off ($\alpha_* = 0.9 \approx 1$)). However, both NGC 2698 and NGC 5507 had $M/L(t, Z, \Gamma)$ values from PyStaff which were 30% too heavy for the kinematics ($\alpha_* = 0.7$).

Comparing again to the benchmark case (model b), the parameter most affected by inclusion

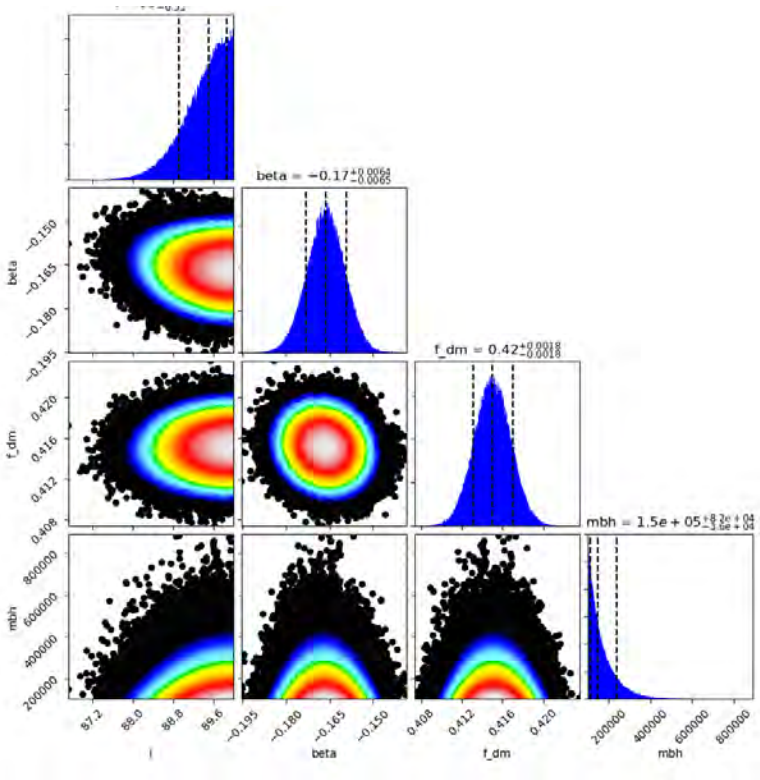

Figure 5.9: As in Figure 5.8, but for NGC 4684.

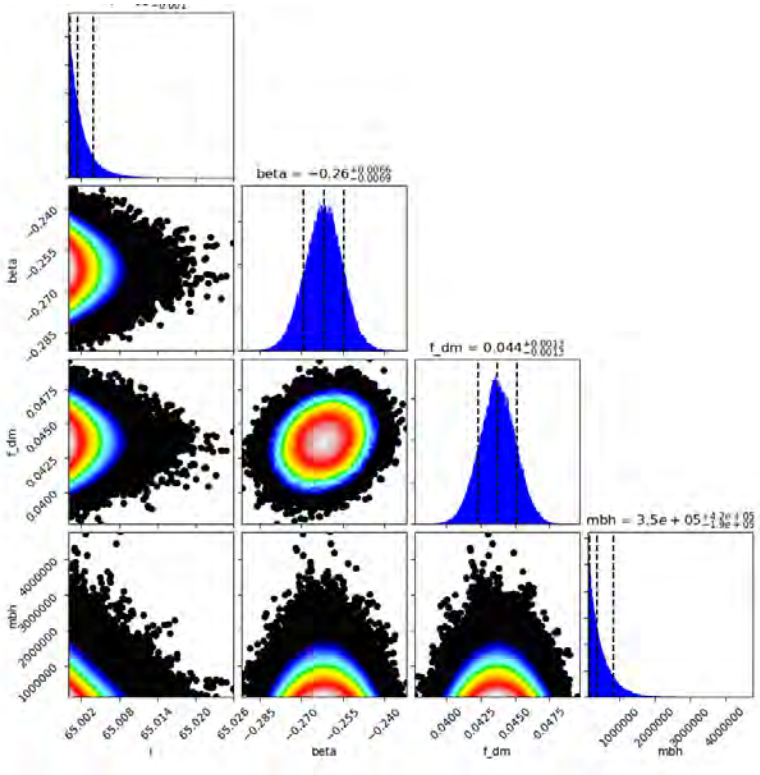

Figure 5.10: As in Figure 5.8, but for NGC 5507.

Table 5.1: Results of the various JAM models

Model	i	β	mass scale factor	f_{DM}	mbh	$\chi 2/DOF$
	$^\circ$	-	-	-	$M_\odot$	-
bounds	[i_{min}, 90]	[-0.5, 0.5]	[0, 20]	[0, 1]	[-2.5, 0]	[1e5, 5e10]
NGC2698						
mass follows light (model a)	70.1 ± 0.0	0.20 ±0.00	5.9 ± 0.0	-	-	3.8
benchmark (model b)	70.5 ± 0.0	0.10 ±0.01	4.5 ± 0.0	0.15 ± 0.00	2.9E+09	2.5
PyStaff model (i)	71.0 ± 0.0	0.17 ±0.00	-	0.00 ± 0.00	2.7E+06	5.1
PyStaff model (ii)	70.5 ± 0.0	0.10 ±0.01	0.7 ± 0.0	0.19 ± 0.00	2.8E+09	2.5
NGC4684						
mass follows light (model a)	78.2 ± 0.1	0.00 ±0.00	3.0 ± 0.0	-	-	1.9
benchmark (model b)	78.3 ± 0.3	0.12 ±0.01	2.3 ± 0.0	0.37 ± 0.01	1.2E+07	0.7
PyStaff model (i)	89.5 ± 0.5	-0.17 ±0.01	-	0.42 ± 0.00	1.5E+05	1.2
PyStaff model (ii)	83.0 ± 0.6	-0.02 ±0.01	0.9 ± 0.0	0.50 ± 0.01	1.7E+05	1.1
NGC5507						
mass follows light (model a)	64.0 ± 0.0	0.00 ±0.00	6.3 ± 0.0	-	-	5.4
benchmark (model b)	64.0 ± 0.0	-0.25 ±0.01	4.4 ± 0.0	0.20 ± 0.00	1.8E+09	1.7
PyStaff model (i)	65.0 ± 0.0	-0.26 ±0.01	-	0.04 ± 0.00	3.5E+05	8.4
PyStaff model (ii)	64.0 ± 0.0	-0.23 ±0.01	0.7 ± 0.0	0.26 ± 0.00	8.7E+08	1.8

All models are made up of a central black hole, a spherical NFW dark matter halo, and a mass model as described below.
The mass follows light model uses a constant M/L to convert light to mass, assuming all mass follows the same distribution as the light. The mass scale factor is $M/L_{\rm dyn}$: the total M/L due to both stars and dark matter [$M_\odot/L_\odot$].
The benchmark model assumes a constant stellar M/L. The mass scale factor is M/L_* [$M_\odot/L_\odot$].
PyStaff model (i) uses our measured $M/L(t,Z,\Gamma)$ profile to convert stellar light to mass, and does not allow this mass model to be re-scaled.
PyStaff model (ii) uses our measured $M/L(t,Z,\Gamma)$ profile to convert stellar light to mass, but then allows the stellar mass model to be rescaled during JAM modelling in order to better fit the kinematics. The mass scale factor is α_*, which is the scaling applied to the stellar mass model to best reproduce the observed kinematics.
Note that some parameters are very tightly constrained, leading to a quoted error of 0.0 when rounded to 1 decimal place.

of the $M/L(t,Z,\Gamma)$ gradients is the dark matter fraction $f_{\rm DM}$. Including the gradients measured directly from the data has the effect of boosting the dark matter fractions by 30% due to the steepening of the stellar mass profile, and the corresponding need for a more dominant dark matter contribution. The black hole masses for NGC 2698 and NGC 5507 are not strongly affected, however the central rise in $M/L(t,Z,\Gamma)$ in NGC 4684 is again compensated for by a substantially less massive black hole.

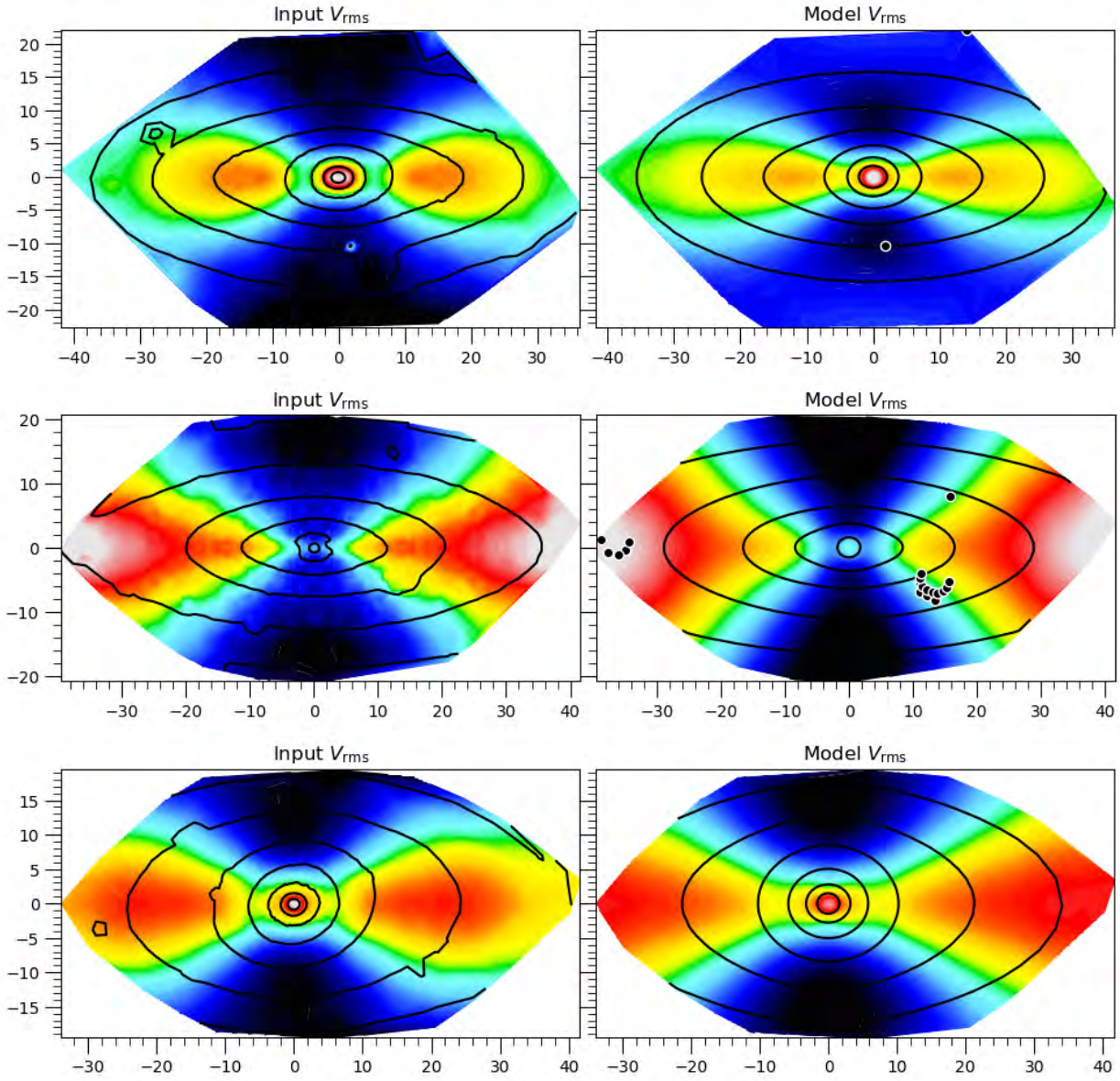

Figure 5.11: Comparison of the observed $V_{\rm rms}$ (left) with the best fitting model $V_{\rm rms}$ for NGC 2698 (top) NGC 4684 (middle) and NGC 5507 (bottom). The mass model is made up of an NFW halo with fixed inner slope $\gamma = -1$, a black hole of mass mbh, and the stellar mass model, which is rescaled to achieve the best fit to the observed kinematics.

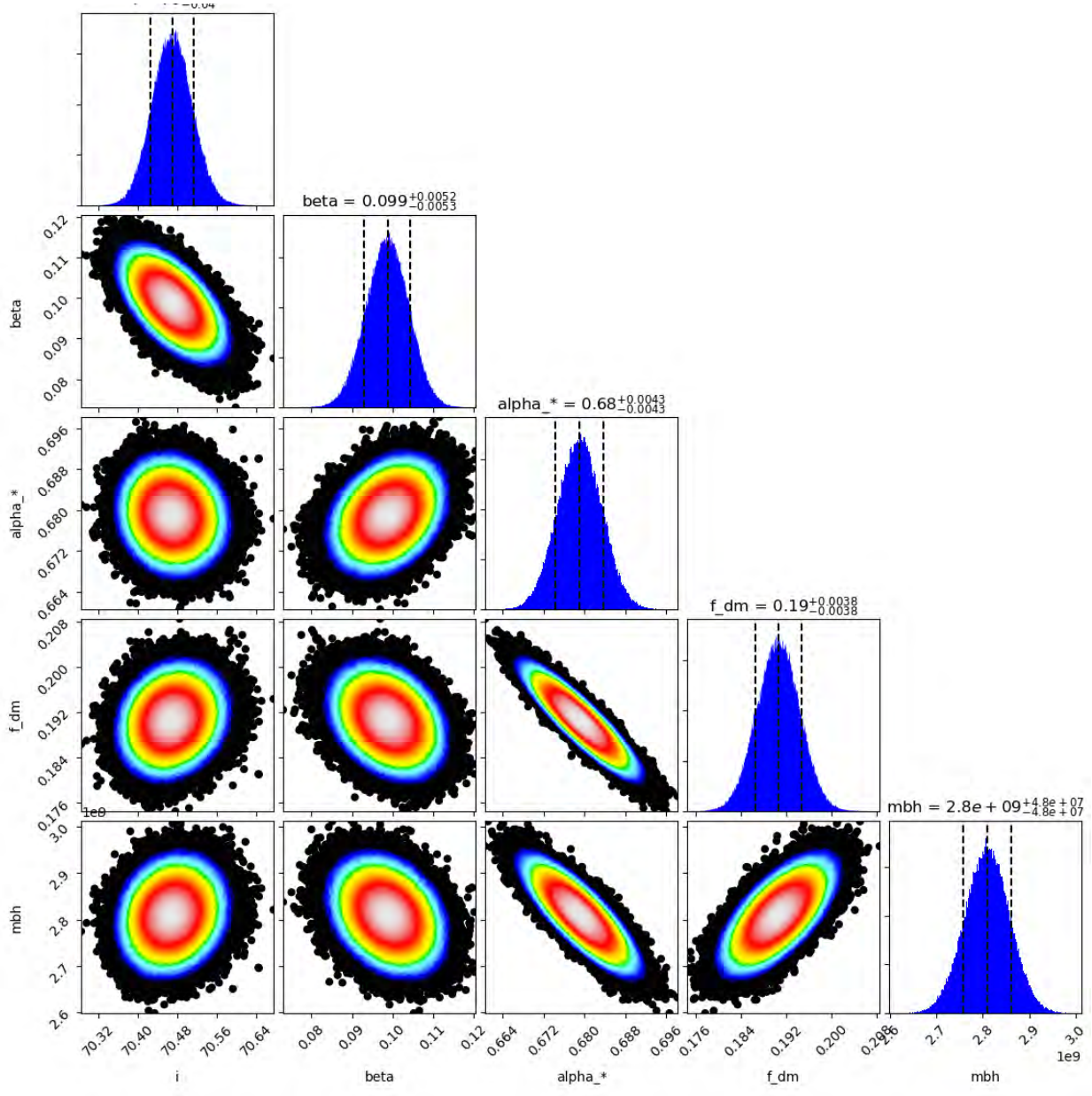

Figure 5.12: The posterior distribution of our JAM modelling for NGC 2698. The mass model is made up of an NFW halo with fixed inner slope $\gamma = -1$, a black hole of mass mbh, and the stellar mass model, which is created by scaling our SDSS imaging by our fitted M/L values and fitting an MGE to the resulting "mass image". The stellar mass model is then rescaled within the JAM modelling in order to obtain the best fit to the kinematics.

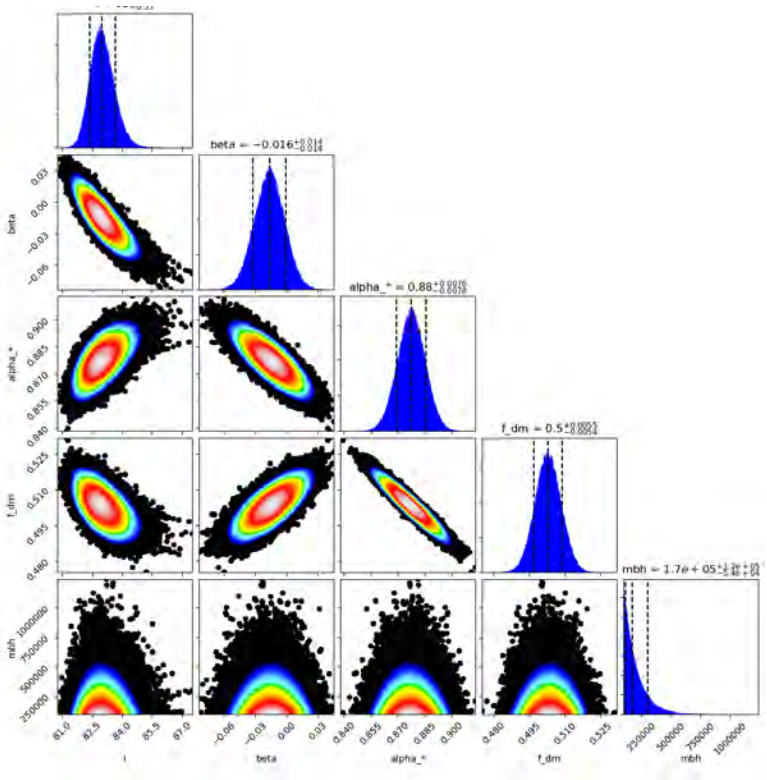

Figure 5.13: As in Figure 5.12, but for NGC 4684.

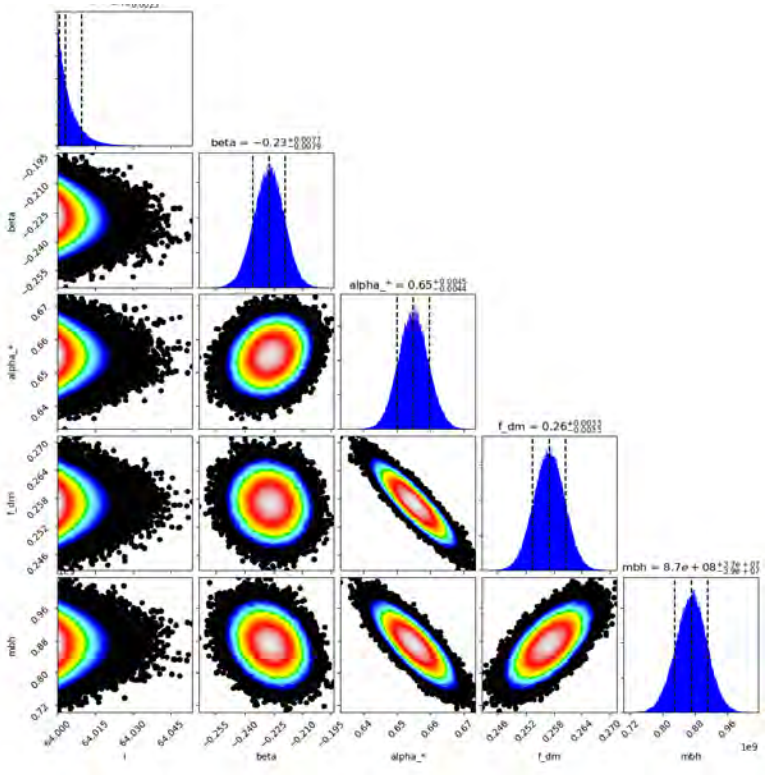

Figure 5.14: As in Figure 5.12, but for NGC 5507.

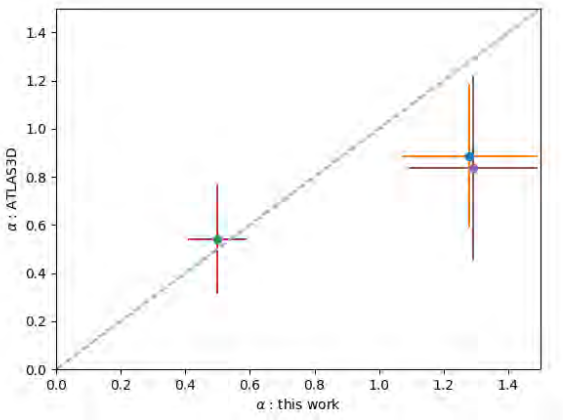

Figure 5.15: Comparison of the global IMF mismatch parameter from ATLAS^{3D} with the values obtained in this work. We take a weighted average of our points.

5.5 Discussion

Radial gradients in the IMF mismatch parameter $\alpha = (M/L)/(M/L_{\rm ref})$ have now been measured spectroscopically in a number of studies. These studies typically find bottom heavy IMFs in the central regions of early-type galaxies (Martín-Navarro et al., 2015, Parikh et al., 2018, Sarzi et al., 2018, Vaughan et al., 2018, van Dokkum et al., 2017) which decline as a function of radius, with indications that the normalisation and steepness of the gradients may be mass dependent (Martín-Navarro et al., 2015, Parikh et al., 2018). Our stellar population analysis broadly supports this picture: NGC 2698 (σ = 193 km s^{-1}) has a spectroscopically-derived IMF mismatch parameter heavier than Salpeter at all radii; NGC 5507 (σ = 164 km s^{-1}) is centrally heavier than Salpeter and declines radially outward; while NGC 4684 (σ = 70 km s^{-1}) has a mismatch parameter consistent with Kroupa at all radii. This is also consistent with the IMF-σ trend from purely dynamical studies (see, for example, Figure 3.1 which shows the the global mismatch parameter derived for these galaxies as part of the ATLAS^{3D} survey).

However, converting the stellar light to mass using the $M/L(t, Z, \Gamma)$ measured directly from the data results in worse fits the observed kinematics. Allowing JAM to rescale the stellar mass results in mass scale factors between 0 and 1, implying that the $M/L(t, Z, \Gamma)$ values obtained from PyStaff were heavier than is allowed by the kinematics. Previously, the mismatch between spectroscopically and dynamically derived M/Ls has been explained by IMF variation (e.g. Cappellari et al., 2012). Specifically, galaxies with $M/L(t, Z)_{\rm SP}$ *heavier* than $M/L_{\rm dyn}$ were justified as requiring a lighter IMF than the one used to derive $M/L(t, Z)_{\rm SP}$. However, in this case, we have measured IMF along with age and metallicity directly from the data, and yet $M/L(t, Z, \Gamma)_{\rm SP}$ is still 30% heavier than allowed by the kinematics in two of our three galaxies.

Our targets are selected from the ATLAS^{3D} survey, so they have *global* mismatch parameters derived in Cappellari et al. (2012). This mismatch parameter $\alpha = (M/L_{\rm dyn,*})/(M/L_{\rm Salp})$, is defined as the ratio of the (global) dynamical stellar M/L estimate compared to a global stellar population based M/L estimate, assuming a fiducial Salpeter IMF. Our spatially resolved IMF mismatch parameter from PyStaff (Figure 5.5) is defined as $(M/L)/(M/L_{\rm Kroupa})$ i.e. it is the M/L excess compared to the M/L calculated assuming a fiducial Kroupa IMF. In order to compare the two, we convert our $M/L_{\rm Kroupa}$ to $M/L_{\rm Salp}$ using the mass normalisation difference of 1.6. We take a weighted average of our radial points (as the profiles are largely flat), and compare this with the global value from Cappellari et al. (2012). This comparison is shown in Figure 5.15. NGC 4684 is in good agreement with the Cappellari et al. (2012) global value. This fits with what we saw when we allowed JAM to rescale the stellar mass : the mass scale factor for NGC 4684 was approximately

unity, implying the fitted $M/L(t, Z, \Gamma)$ was close to the dynamical one. However NGC 2698 and NGC 5507 have global mismatch parameters which are higher than the Cappellari et al. (2012) values (approximately 1.3 compared to 0.85). This means that according to the ATLAS^{3D}dynamical study, these two galaxies have an IMF approximately 85% as heavy as Salpeter, while according to our spectroscopic study alone, they are 30% heavier than Salpeter. However, as we showed before, our own dynamical modelling also disagrees with our spectroscopically derived $M/L(t, Z, \Gamma)$, preferring to scale the stellar mass down by 30% in order to reproduce the kinematics, which brings them back into agreement with ATLAS^{3D}. Thus, while the trend towards heavier IMF mass normalisation in higher mass galaxies appears similar between dynamically and spectroscopically derived stellar masses, applying the techniques self-consistently reveals a significant residual mass normalisation difference, in the sense that stellar population models over-predict the stellar mass by 30% in our higher-mass galaxies.

This is similar to the results of Smith (2014, hereafter S14), who compare dynamical IMF estimates from (Cappellari et al., 2013b, hereafter A3D) with stellar population estimates from (Conroy & van Dokkum, 2012, hereafter CVD), and find that while the two techniques agree on average, they disagree on a galaxy-by-galaxy basis. S14 suggests a number of possible causes for this discrepancy: errors in one or both techniques; the two methods could be sensitive to different aspects of the IMF; or radial IMF variation. The A3D and CVD studies compared by S14 probe the IMF on very different galaxy scales. The stellar population IMF measurements of CVD were done in a central aperture of $R_e/8$, while the dynamical modelling from A3D typically covered $\sim 1R_e$. Our results, based on fully self-consistent modelling on the same high-quality IFU data, suggest that radial gradients in the IMF (and other stellar population properties) are not the cause of the discrepancy between stellar population and dynamical IMF estimates, as we account for them explicitly in our dynamical models.

This may instead indicate that systematics in either the dynamical or stellar population modelling used to derive the M/L are the cause. One possible explanation is that the parametrisation of the IMF in the stellar population models we use could be incorrect. La Barbera et al. (2013) and Lyubenova et al. (2016) nicely showed that it is possible to obtain a similarly good fit to IMF-sensitive spectral features but get a very different $M/L_{\rm SP}$, depending on the assumed form of the IMF. In particular, Lyubenova et al. (2016) used the strong constraint that the total $M/L_{\rm dyn}$ must be larger than the stellar $M/L_{\rm SP}$ to rule out a single power-law form for the IMF. This was done by comparing the (global) stellar population M/L estimates from index measurements to a (global) dynamical M/L estimate, both obtained using the same CALIFA data. We expand upon this work by including spatial variation in stellar population parameters, explicitly modelling the dark matter and black holes, as well as constraining the IMF using full spectral fitting. We also find that the stellar population M/L estimates are heavier than allowed by the dynamics (for our particular parametrisation of the IMF), as Lyubenova et al. (2016) found in the case of a unimodal (single slope power law) IMF. Specifically, we measured $M/L_{\rm SP}$ assuming a form where the IMF is described by a two-part power law below $1M_\odot$, with the low-mass slopes free to vary, and the high mass end fixed to the Salpeter slope of 2.3, potentially indicating that this description of the IMF is too restrictive.

5.6 Conclusion

We carry out a self-consistent study of the stellar population and dynamical properties of three nearby early-type galaxies using high quality, spatially resolved MUSE spectroscopy. We measure stellar population properties on the same data from which we extract our kinematics. We measure the IMF as a function of radius, using state of the art stellar population models, which we fit directly to the entire spectral range using MCMC methods. Using the spectroscopic approach, we

find our lowest mass galaxy has an IMF consistent with Kroupa at all radii, while our higher mass galaxies are bottom heavy, with one declining as a function of radius.

These results are quantitatively similar to results obtained by other authors, who find mass-dependent radial IMF gradients to be a feature of ETGs. However the $M/L(t,Z,\Gamma)$ values implied by our spectroscopic age, metallicity and IMF measurements are typically higher than dynamically determined M/L values measured from the same data. As the stellar population M/L estimate cannot be heavier than the total M/L determined from the dynamics, we suggest that systematic uncertainties remain in the stellar population models. Including our measured $M/L(t,Z,\Gamma)$ *gradients* in dynamical models, but allowing the absolute normalisation to be re-scaled has the effect of increasing dark matter fractions by 30% on average. Black hole masses can also be affected in the case of strong M/L gradients. This highlights the importance of correctly accounting for the presence of M/L gradients in dynamical modelling.

6 Conclusion

This thesis has focused on gaining insights into the formation and evolution of early-type galaxies through the analysis of their stellar populations and dynamics. Specifically, we aimed to address a number of open questions in the field of ETG evolution, namely: (i) How accurate are near-infrared stellar population synthesis models, and what is the impact of different prescriptions for the luminous but short-lived TP-AGB phase? (ii) What are the impacts of a spatially varying stellar initial mass function on the mass distribution of early-type galaxies, and (iii) By incorporating a spectroscopically-derived spatially varying mass to light ratio that depends on age, metallicity and IMF, are we able to build fully self-consistent dynamical models that accurately predict the observed stellar kinematics from the same observations?

6.1 Near-infrared stellar population synthesis models

In Chapter 2 we carried out a detailed comparison of four commonly used stellar population synthesis models that provide moderately high resolution spectral energy distribution predictions from optical through infrared wavelengths. Near-infrared wavelengths are important for studying dust-obscured objects, as well as critical in constraining the contribution of low-mass stars to the integrated light of galaxies, and will be commonly used in the era of the James Webb Space Telescope. However the most commonly used models, when applied to the same data, give highly discrepant results. Past works on this issue find that it is due to their differing treatments of the thermally pulsing asymptotic giant branch (TP-AGB) phase, which can dominate intermediate age populations (Lançon, 1998) and strongly affect derived properties (Maraston et al., 2006, Zibetti et al., 2013).

We carried out an analysis using high S/N near-infrared spectroscopy of a small sample of ETGs, spanning a range of ages, at approximately solar metallicity and abundances. This sample selection was based on isolating the contribution of the TP-AGB, a strongly age dependent phase, to the near-infrared spectra of galaxies. In this work, however, we find that the largest differences between the models are caused by the choice of stellar spectral library, rather than the specifics of the TP-AGB inclusion in the models. We find that high resolution spectral libraries result in better fits to the data, and more self-consistent star formation histories when comparing optical and near-infrared predictions. Near-infrared stellar spectral libraries currently still lag behind the optical in terms of resolution and coverage of parameter space, however a number of high quality

spectral libraries are under active development at the moment. The IRTF Spectral Library (Rayner et al., 2009), for example, spans $0.8 - 5.0\mu$m at a resolution $R \sim 2000$ and S/N ~ 100. The library currently contains ~ 300 mainly solar-metallicity late-type stars, but has been extended by Villaume et al. (2017) to span a range of $T_{\rm eff}$, log g, and metallicity, specifically for the purpose of incorporating this library into stellar population models. Similarly, the X-Shooter Spectral Library (Chen et al., 2014) currently contains more than 200 stars with continuous wavelength coverage from the near UV to the NIR ($0.3 - 2.4\mu$m), at a resolution of $R \sim 10,000$, with the final sample expected to contain over 700 stars of a wide range of spectral types. When these next-generation libraries are incorporated into stellar population models, it should immediately rectify some of the discrepancies between the current near-infrared models, which at present seem to be driven by differences in the spectral libraries such as resolution and parameter coverage. Our analysis indicates that higher spectral resolution libraries (at least equal to the resolution of the observations being analysed) give more self-consistent optical-NIR star formation histories. In addition, this work highlights the importance of having both broad spectral coverage and enough spectral resolution to measure individual absorption lines, as well as the utility of using multiple stellar population models to explore the systematic differences.

While we found the model treatment of the TP-AGB phase had only a limited effect on the derived properties, this may be due to the low mass fraction of stars in this age range present in our sample. The young mean ages derived at optical wavelengths for a number of the galaxies in our sample are likely due to a frosting of young stars on top of a dominant old population. A next logical step would be to extend this work to galaxies with a higher mass fraction of intermediate age populations such as nearby young star clusters, or galaxies at high redshift, where we expect a larger contribution from TP-AGB stars to the integrated light. Future tests of stellar population models in this wavelength range could also expand to include galaxies with a wider range of metallicity and abundance than the solar metallicity sample we study here, particularly as strengths of various 'TP-AGB features' are strongly dependant on metallicity (Maraston, 2005).

6.2 IMF variation in early-type galaxies: incorporating stellar population gradients into dynamical models

Three techniques are typically used to constrain the IMF in unresolved populations: those based on stellar population modelling, dynamics, and strong lensing. While the overall consensus from all three techniques is one of systematic IMF variation across the ETG population, significant discrepancies exist between the methods when applied to the same galaxies (Smith, 2014). Previous works have mostly used integrated measurables, treating the IMF as a uniform property within a galaxy, and focusing on systematic differences between galaxies. In this work, we carry out a spatially resolved study of IMF variation within galaxies, and we incorporate spatial variations in age, metallicity and IMF into our dynamical models.

In Chapter 4 we measure gradients in age and metallicity from high quality MUSE spectroscopy of three nearby ETGs. Converting these age and metallicity gradients into gradients in M/L allows us to create models of the stellar mass free from the simplifying assumption of a constant M/L usually made in dynamical modelling. We find that including these $M/L(t, Z)$ gradients in our dynamical models has a minimal effect on dynamically-derived properties. However, if we also include the added M/L variation due to the IMF gradients recently observed in a number of nearby ETGs by van Dokkum et al. (2017), this has a large impact on the outputs of our dynamical models.

The strong IMF gradients, being super-Salpeter in the galaxy centres, and declining to Milky Way-like in the outskirts, have the effect of boosting the central M/L by a factor approximately 2.5, and steepening the M/L profile compared to assuming a constant IMF. This significantly steepens

the stellar mass profile compared to what one would obtain with a constant M/L. The knock-on effect when including this in dynamical models is that it requires an increase in the fraction of dark matter within an effective radius of $\approx 50\%$ in order to compensate for this missing mass in the outer regions. This means that if IMF gradients are a common feature in the ETG population, dark matter estimates derived from dynamical studies assuming a constant M/L would have to be revised upward. Large surveys such as ATLAS^{3D} and CALIFA make this assumption in their dynamical modelling for simplicity, and have typically derived low median dark matter fractions within an effective radius (e.g. 13% in ATLAS^{3D}Cappellari et al. 2013a. Changing this number would have important implications for the nature of dark matter (Spergel & Steinhardt, 2000), models of halo formation such as adiabatic contraction (Blumenthal et al., 1986, Gnedin et al., 2004), and galaxy formation, through the dependence of the dark matter distribution on processes such as supernova feedback (Navarro et al., 1996). A greater contribution from dark matter may also contradict the common assumption when carrying out various types of modelling, which is to assume that dark matter can be neglected in the central regions of galaxies. We show here that the dark matter fraction within an effective radius under the assumption of a varying IMF is between $30 - 55\%$ in our sample.

Strong M/L gradients due to a varying IMF can also decrease black hole masses derived from dynamical modelling by up to a factor 2. Making strong statements on black hole masses is beyond the scope of this work, due to our small sample, and the difficulties in accurately constraining black hole mass with seeing-limited data. However, we note that what we observe is largely consistent with expectation: if IMF variation is centrally concentrated, this assigns more central mass to stars, and will reduce the black hole mass. Indications are that the IMF is systematically heavier at high σ, and the M-σ relation is a key scaling relation that is used to calibrate black hole properties in simulations, making this an interesting topic for future work.

6.3 IMF variation in early-type galaxies: fully self consistent stellar population and dynamical modelling

In Chapter 5 we used a Markov Chain Monte Carlo approach to simultaneously fit for the IMF and various individual element abundances, as well as age and metallicity across our galaxies. This allowed us to perform the first fully self-consistent, spatially resolved, stellar population and dynamical modelling analysis including IMF variation. We measured radial variation in the IMF using stellar population modelling, which we described in terms of the IMF mismatch parameter $\alpha = (M/L)/(M/L)_{\rm Kr}$. Our galaxies exhibit a range of IMF gradients, being shallow and consistent with Kroupa for our lowest mass galaxy, but with steepening gradients and increasing IMF normalisation for our higher mass galaxies. This is consistent with previous spectroscopic studies who find mass dependent IMF gradients to be a feature of ETGs (Parikh et al., 2018, van Dokkum et al., 2017). Of particular interest was one galaxy, for which we derived a very steep profile of $M/L(t, Z, \Gamma)$, very similar to the one derived by van Dokkum et al. (2017) for their sample of nearby ETGs. However, when we incorporated our measured $M/L(t, Z, \Gamma)_{\rm SP}$ values into our dynamical models, we found we obtained worse fits to the kinematics. Comparing the $M/L(t, Z, \Gamma)_{\rm SP}$ values we obtained from fitting the spectra to the $M/L_{\rm dyn}$ we obtained from the dynamical modelling, we find the stellar population based estimates are typically higher than those obtained from the dynamics, requiring the stellar mass to be rescaled downwards in order to match the galaxy kinematics.

The inconsistency between IMFs measured using stellar population and dynamical modelling methods on the same data is in agreement with the study of Smith (2014), indicating that one or both methods fail to account for their respective IMF degeneracies, or that the methods measure intrinsically different things. We rule out aperture effects and radial IMF variation as the cause

of the discrepancy, as we incorporate spatially resolved IMF measurements into our dynamical models, and the inconsistency between the two methods remains.

This may indicate that systematics in the stellar population models used to derive the $M/L_{\rm SP}$ are the cause. Lyubenova et al. (2016) used the strong constraint that the total (global) dynamical M/L must be larger than the global stellar population M/L to rule out a single power-law form for the IMF using the MILES models (Vazdekis et al., 2010, 2012) applied to data from the CALIFA survey. Similar to the findings of this study, our work may imply that the specific IMF shape we use to derive $M/L_{\rm SP}$ could be incorrect. Specifically, we measured $M/L_{\rm SP}$ assuming a form where the IMF is described by a two part power law below $1M_{\odot}$, with the low-mass slopes free to vary, and the high mass end fixed to the Salpeter slope of 2.3. An obvious extension would involve expanding this analysis to test other types of IMF shapes, such as the single and double power law IMFs used in the MILES models, or a completely non-parametric form such as that explored in Conroy et al. (2017).

This work highlights the importance of self-consistent studies, which incorporate stellar population constraints into dynamical modelling of the same data set, thus free from any data-induced systematics. The potentially large effects of stellar population gradients on dynamically-derived quantities (which are typically presented as being independent of stellar population modelling), and the inconsistency between the two approaches, indicates further analysis is needed in order to accurately recover various galaxy properties using the two techniques. This would require high S/N integral field spectroscopy spanning a wide wavelength range, in order to provide accurate constraints on the stellar population properties of interest. The diverse gradients we see within our sample is testament to the need for this type of work to be carried out on a large sample of galaxies. This is becoming feasible with the advent of large integral field surveys such as MaNGA, which provide spatially resolved information for statistically significant samples of galaxies of diverse morphological types. This is a vast improvement over previous imaging surveys, which were available for large samples, but typically lacked spectroscopic information, or were limited to single aperture spectra. Utilising next-generation data sets such as this for self-consistent IMF studies should add some clarity to the current state of affairs.

A

Appendix A: Tabulated optical and near-infrared star formation histories, and near-infrared line strength indices from Chapter 2

Table A.1: Results for the near-infrared fits using a Calzetti extinction curve.

	BC			FSPS			V16			M11		
Galaxy	$\chi^2_{\rm red}$	E(B-V)	$t_{\rm av}$	$\chi^2_{\rm red}$	E(B-V)	$t_{\rm av}$	$\chi^2_{\rm red}$	E(B-V)	$t_{\rm av}$	$\chi^2_{\rm red}$	$E(B-V)$	$t_{\rm av}$
IC0719	12.74	0.07	9.88	68.91	0.20	7.87	5.06	0.10	9.98	14.19	0.16	13.83
NGC3032	12.33	0.00	2.91	40.99	0.04	7.77	2.72	0.00	9.78	6.42	0.05	3.03
NGC3098	10.20	0.06	11.70	47.10	0.16	8.24	2.64	0.08	12.33	7.91	0.13	13.11
NGC3156	13.51	0.00	3.78	50.17	0.05	7.50	3.79	0.00	10.24	11.45	0.00	13.91
NGC3182	9.46	0.05	13.79	74.44	0.19	6.67	4.44	0.09	12.43	12.23	0.15	14.08
NGC3301	15.47	0.00	13.89	74.75	0.12	6.23	5.49	0.03	12.75	15.58	0.08	13.14
NGC3489	23.50	0.00	12.81	127.67	0.11	6.71	11.68	0.03	10.56	26.13	0.08	13.74
NGC4379	20.29	0.04	12.16	168.35	0.18	7.18	8.99	0.09	11.98	26.00	0.14	14.47
NGC4578	14.11	0.04	13.44	185.24	0.17	7.39	5.94	0.08	11.31	20.40	0.13	14.46
NGC4608	10.84	0.02	8.26	89.35	0.14	6.01	2.77	0.04	11.08	11.86	0.09	14.00
NGC4710	14.38	0.53	7.75	18.64	0.57	7.81	2.63	0.54	7.74	7.06	0.57	3.55
NGC5475	15.04	0.00	12.67	52.36	0.12	7.36	3.05	0.03	10.60	11.48	0.09	12.94

Columns give:
reduced $\chi 2$ ($\chi 2$ divided by the degrees of freedom)
the colour excess due to extinction $E(B-V)$
the mass weighted mean age $t_{\rm av}$

Table A.2: Results for the optical fits using a Calzetti extinction curve.

	BC			FSPS			V16			M11		
Galaxy	$\chi^2_{\rm red}$	E(B-V)	$t_{\rm av}$	$\chi^2_{\rm red}$	E(B-V)	$t_{\rm av}$	$\chi^2_{\rm red}$	$E(B-V)$	$t_{\rm av}$	$\chi^2_{\rm red}$	$E(B-V)$	$t_{\rm av}$
IC0719	7.39	0.46	12.35	3.42	0.51	9.03	4.21	0.48	10.55	3.09	0.45	12.53
NGC3032	4.68	0.21	1.00	5.56	0.24	1.00	4.56	0.22	1.00	7.47	0.09	1.00
NGC3098	8.26	0.36	9.15	3.93	0.39	6.30	5.14	0.37	7.33	3.74	0.34	11.16
NGC3156	4.04	0.31	1.01	2.80	0.34	1.12	2.59	0.32	1.12	7.26	0.19	1.00
NGC3182	15.39	0.14	13.86	6.67	0.22	12.05	8.11	0.17	12.75	7.94	0.15	13.83
NGC3301	11.12	0.33	6.77	4.67	0.36	5.23	6.99	0.34	6.19	3.75	0.28	7.97
NGC3489	7.88	0.29	12.57	2.79	0.32	8.54	3.63	0.30	10.41	2.96	0.24	8.75
NGC4379	12.71	0.29	13.46	4.67	0.35	10.96	6.50	0.32	12.40	5.76	0.31	13.63
NGC4578	26.15	0.21	13.98	10.03	0.29	12.46	13.34	0.25	13.01	12.96	0.24	14.02
NGC4608	26.63	0.22	13.76	7.97	0.28	11.31	12.21	0.25	12.77	10.33	0.24	13.99
NGC4710	11.74	0.53	9.03	6.53	0.56	6.47	8.29	0.54	7.22	6.08	0.49	10.88
NGC5475	5.83	0.24	12.93	3.13	0.27	7.21	2.78	0.25	10.26	2.61	0.22	11.88

Table A.3: Results for the near-infrared fits using an order 10 multiplicative polynomial.

	BC03		FSPS		V16		M11	
Galaxy	$\chi^2_{\rm red}$	$t_{\rm av}$	$\chi^2_{\rm red}$	$t_{\rm av}$	$\chi^2_{\rm red}$	$t_{\rm av}$	$\chi^2_{\rm red}$	$t_{\rm av}$
IC0719	6.24	6.51	7.13	3.69	1.96	12.66	4.53	5.52
NGC3032	4.03	4.02	3.57	12.99	1.11	8.24	2.76	3.04
NGC3098	4.36	4.19	3.91	12.25	1.23	12.08	2.76	4.78
NGC3156	4.31	3.93	3.68	10.69	1.41	8.62	3.12	4.69
NGC3182	3.18	3.72	3.88	12.38	1.22	11.50	2.32	4.14
NGC3301	5.07	3.82	4.44	10.21	1.46	12.27	3.11	4.76
NGC3489	7.29	4.59	5.34	10.08	2.17	11.01	5.03	4.32
NGC4379	4.95	4.26	3.98	10.00	1.48	12.67	3.60	4.83
NGC4578	5.28	3.02	5.70	12.88	1.54	11.55	4.32	3.65
NGC4608	4.71	2.74	4.08	13.26	1.15	9.71	3.82	3.55
NGC4710	5.11	4.48	4.02	4.91	1.46	9.57	3.57	3.76
NGC5475	5.95	4.77	4.60	8.76	1.48	11.98	3.88	3.16

Table A.4: Results for the optical fits using a multiplicative polynomial.

	BC03		FSPS		V16		M11	
Galaxy	$\chi^2_{\rm red}$	$t_{\rm av}$	$\chi^2_{\rm red}$	$t_{\rm av}$	$\chi^2_{\rm red}$	$t_{\rm av}$	$\chi^2_{\rm red}$	$t_{\rm av}$
IC0719	5.57	13.34	2.29	7.14	2.20	9.39	2.23	13.00
NGC3032	4.84	1.00	5.49	1.00	4.25	1.00	5.43	1.00
NGC3098	7.06	9.79	3.00	4.76	3.71	6.18	3.14	8.69
NGC3156	4.08	1.00	2.57	1.00	1.89	1.00	6.13	1.00
NGC3182	12.49	14.06	4.13	12.33	4.69	12.99	5.22	14.05
NGC3301	9.33	7.27	2.98	4.10	4.30	5.69	3.28	5.24
NGC3489	6.49	13.09	2.23	7.00	1.91	8.98	3.09	9.37
NGC4379	11.47	13.57	4.37	10.39	5.52	12.05	4.48	14.13
NGC4578	22.67	14.24	6.21	12.73	8.74	13.36	9.07	14.40
NGC4608	24.01	14.02	6.80	10.89	9.78	12.74	7.59	14.34
NGC4710	8.11	10.39	4.19	4.51	4.77	5.97	4.48	6.55
NGC5475	5.20	13.31	2.68	6.28	1.99	8.97	2.53	11.21

Table A.5: Results of updated FSPS models with Calzetti extinction curve

	Padova			MIST		
	Near-IR		Optical	Near-IR		Optical
Galaxy	$\chi^2_{\rm red}$	$t_{\rm av}$	$t_{\rm av}$	$\chi^2_{\rm red}$	$t_{\rm av}$	$t_{\rm av}$
IC0719	4.26	11.47	9.71	4.25	12.97	10.33
NGC3032	4.07	8.41	1.08	4.15	3.72	3.32
NGC3098	2.92	7.60	5.57	2.97	7.67	6.21
NGC3156	3.49	6.48	1.19	3.48	4.10	1.50
NGC3182	4.0	12.19	12.00	4.05	13.02	12.18
NGC3301	5.95	5.68	4.14	6.06	11.18	4.63
NGC3489	11.00	6.65	6.50	11.30	11.59	8.73
NGC4379	7.32	12.00	9.43	7.40	13.33	10.69
NGC4578	5.29	12.98	12.08	5.31	13.26	12.23
NGC4608	2.25	11.25	11.29	2.35	11.06	11.84
NGC4710	2.91	4.64	5.57	2.93	3.46	6.61
NGC5475	3.62	6.98	9.84	3.72	8.26	10.84

Table A.6: Line strengths measured in the data, at $R \approx 500$

Galaxy	CN1.1 (mag)	Na1.14 (Å)	CN1.4 (mag)	C_2 (mag)	Na 2.21 (Å)	⟨Fe⟩ (Å)	Ca (Å)	Mg (Å)	CO (mag)
IC0719	0.072±0.004	0.943±0.282	0.097±0.004	0.053±0.005	3.115 ±0.277	1.13±0.238	2.161±0.582	0.567±0.3	1.197±0.004
NGC3032	0.112±0.003	2.254±0.303	0.12±0.004	0.049±0.005	5.056 ±0.307	0.977±0.272	3.913±0.618	0.798±0.334	1.219±0.005
NGC3098	0.107±0.003	1.189±0.232	0.094±0.003	0.04±0.004	2.82± 0.241	0.793±0.206	2.375±0.457	0.898±0.262	1.192±0.004
NGC3156	0.074±0.003	0.798±0.257	0.103±0.003	0.042±0.004	2.559 ±0.257	0.551±0.22	2.256±0.498	0.151±0.266	1.198±0.004
NGC3182	0.088±0.004	1.323±0.285	0.094±0.004	0.041±0.005	3.347 ±0.284	1.048±0.248	2.831±0.566	0.704±0.298	1.202±0.005
NGC3301	0.106±0.003	1.066±0.261	0.11±0.004	0.041±0.005	2.797 ±0.278	0.91±0.224	3.081±0.54	0.689±0.278	1.211±0.004
NGC3489	0.08±0.002	0.722±0.193	0.121±0.002	0.047±0.003	2.929 ±0.196	1.007±0.164	2.398±0.403	0.614±0.211	1.206±0.003
NGC4379	0.041±0.003	0.364±0.247	0.099±0.003	0.052±0.005	3.589 ±0.262	0.568±0.225	1.577±0.49	0.746±0.302	1.184±0.004
NGC4578	0.052±0.003	1.253±0.225	0.101±0.003	0.05±0.004	4.121 ±0.234	1.057±0.197	2.377±0.449	0.792±0.247	1.208±0.004
NGC4608	0.065±0.004	0.838±0.28	0.105±0.003	0.056±0.005	2.972 ±0.296	0.939±0.237	2.913±0.547	1.273±0.289	1.186±0.004
NGC4710	0.07±0.005	0.555±0.346	0.062±0.004	0.032±0.005	3.234 ±0.358	1.115±0.282	2.68±0.641	0.943±0.362	1.204±0.005
NGC5475	0.118±0.003	1.045±0.222	0.116±0.003	0.052±0.004	3.742 ±0.233	1.147±0.185	3.143±0.442	1.017±0.237	1.211±0.003

B

Appendix B: Inferences on MUSE galaxy sample for the various dynamical models from Chapter 4

Table B.1: MGEs of the mass density for each galaxy, including measured M/L variation due to age and metallicity gradients, but assuming a constant Salpeter IMF.

NGC 2698			NGC 4684			NGC 5507		
count	σ	q	count	σ	q	count	σ	q
88929.4	0.984591	0.651399	58311.5	0.409859	0.684490	171393.	0.318471	0.700000
26701.0	2.06285	0.737128	4460.98	1.65865	1.00000	39572.4	0.876226	0.950000
4418.61	3.68446	0.850000	4310.47	6.79360	0.368980	7960.30	1.53479	0.450000
3376.01	5.19929	0.467101	1371.02	12.2295	0.431055	16187.2	2.10548	0.777583
2336.78	12.6048	0.300000	204.211	25.3720	0.500789	2382.89	3.79907	0.950000
1015.64	12.9197	0.467866	545.193	29.0740	0.300000	3310.30	5.00080	0.835136
188.221	26.0843	0.850000	87.5500	55.4878	0.309939	418.636	9.50350	0.896721
370.627	26.0843	0.344950				883.645	20.2237	0.450000

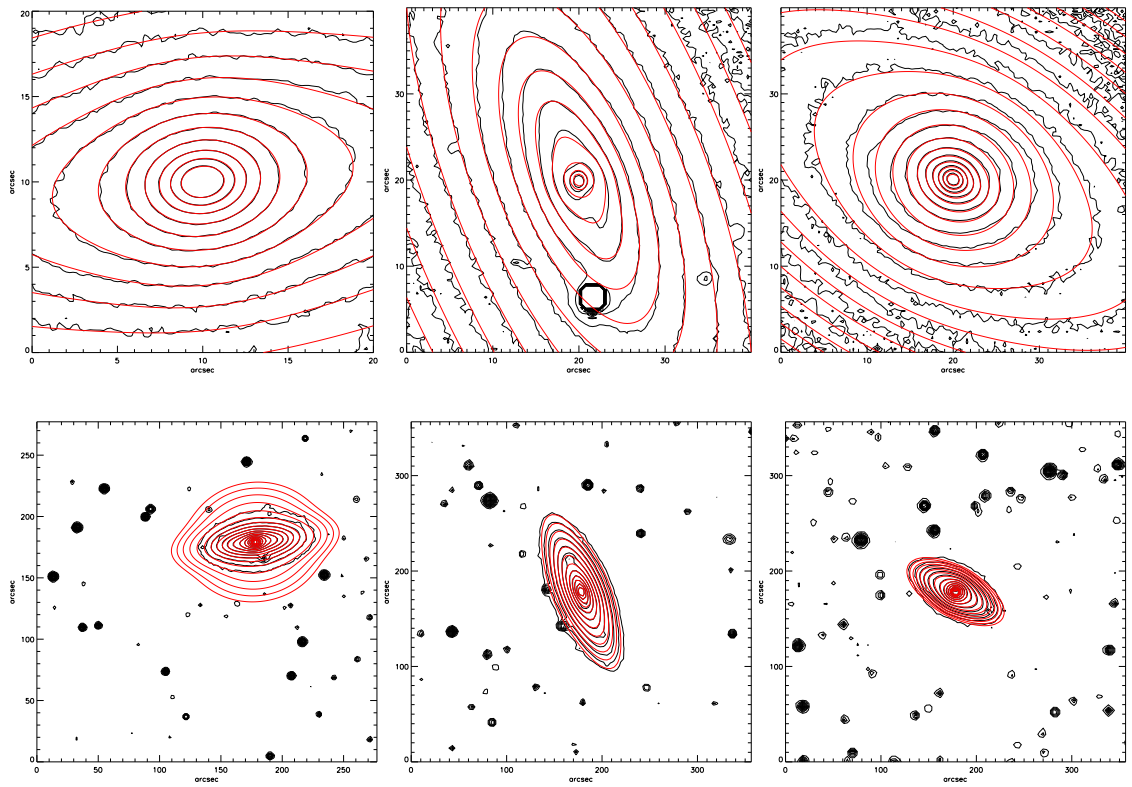

(a) NGC 2698 (b) NGC 4684 (c) NGC 5507

Figure B.1: Mass MGEs for each galaxy. Images are converted from light to mass using stellar population modelling assuming a constant (Salpeter) IMF. Black contours are the mass images, and red contours are the best-fitting MGE models. For each galaxy, we show the central region (top) and the entire galaxy (bottom).

Table B.2: MGEs of the mass density for each galaxy including measured M/L variation due to age and metallicity gradients, plus that due to the IMF gradients measured by van Dokkum et al. (2017).

NGC 2698			NGC 4684			NGC 5507		
count	σ	q	count	σ	q	count	σ	q
144436.	0.938680	0.575889	48987.3	0.318471	0.900000	236273.	0.318471	0.750000
44139.3	2.00194	0.644937	21432.3	0.577154	0.900000	37779.0	0.880250	1.00000
3838.54	3.80105	0.759536	6025.62	1.52422	0.900000	32156.4	0.988042	0.500000
530.000	4.81139	0.950000	2328.83	3.73630	0.665303	14830.6	1.98718	0.726660
7712.53	5.05730	0.300000	4702.48	7.28078	0.311629	13957.8	2.34795	0.500000
1927.82	10.9568	0.314301	2043.77	8.22231	0.440693	2037.46	3.30063	1.00000
253.823	19.8006	0.737009	244.279	15.6676	0.569923	2316.27	5.21821	0.838981
722.641	19.8006	0.332838	434.487	22.9649	0.300000	135.986	8.47996	1.00000
			187.258	40.4490	0.300000	370.055	16.0705	0.500000
			48.6836	41.2471	0.573903	369.678	22.4798	0.500000

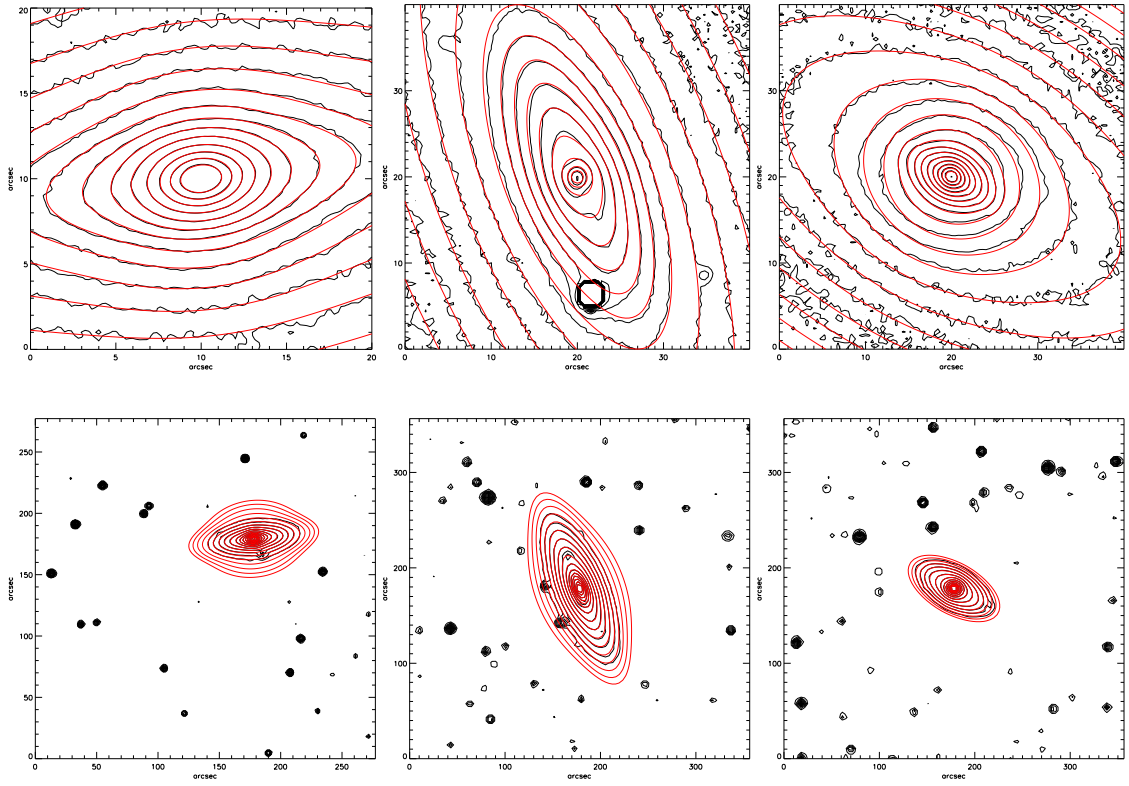

(a) NGC 2698 (b) NGC 4684 (c) NGC 5507

Figure B.2: Mass MGEs for each galaxy. Images are converted from light to mass by measuring the gradients in age and metallicity using stellar population models, and adding on the effects of a spatially varying IMF as measured by van Dokkum et al. (2017). Black contours are the mass images, and red contours are the best-fitting MGE models. For each galaxy, we show the central region (top) and the entire galaxy (bottom).

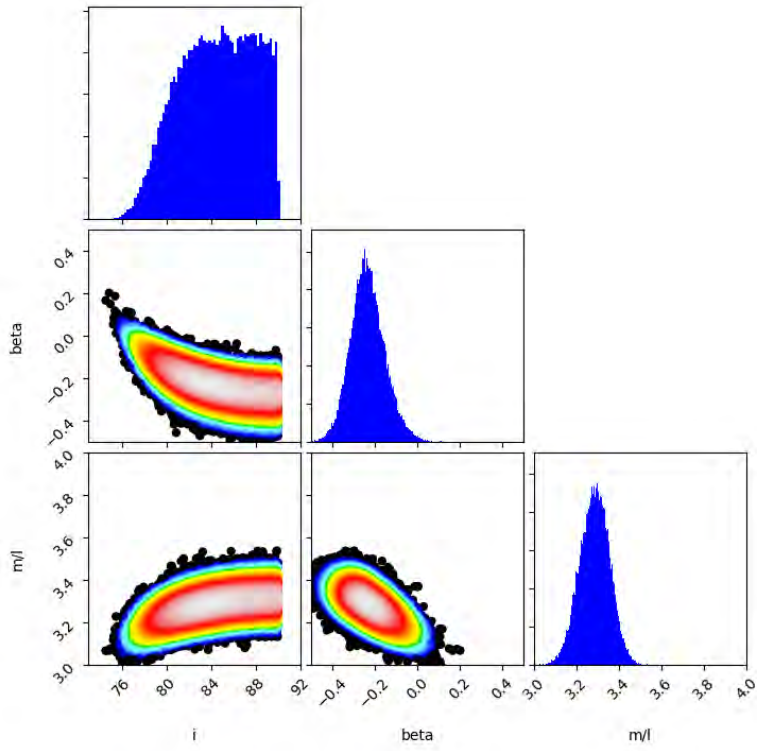

Figure B.3: Our posterior distributions in the mass-follows-light case (model a) for NGC 4684. Free parameters are inclination, anisotropy and total mass-to-light ratio.

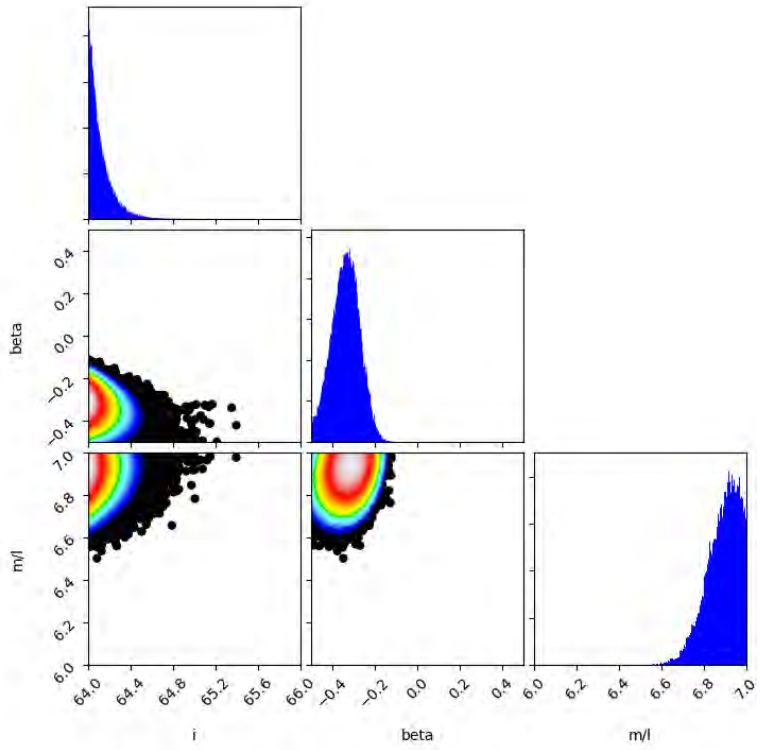

Figure B.4: Our posterior distributions in the mass-follows-light case (model a) for NGC 5507

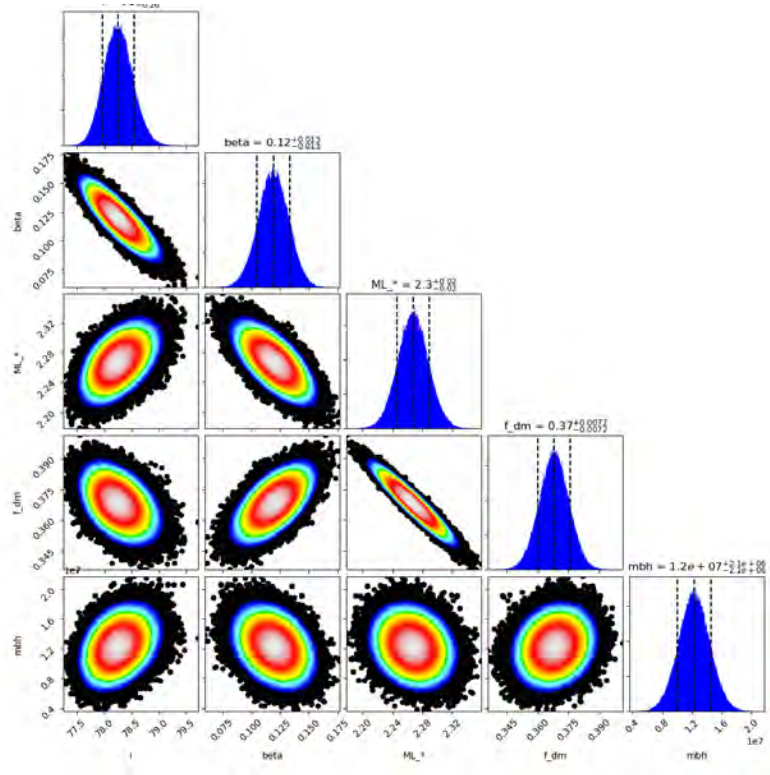

Figure B.5: Our posterior distributions in the stars+NFW halo case (model b) for NGC 4684. Free parameters are inclination, anisotropy, stellar mass-to-light ratio, dark matter fraction and black hole mass.

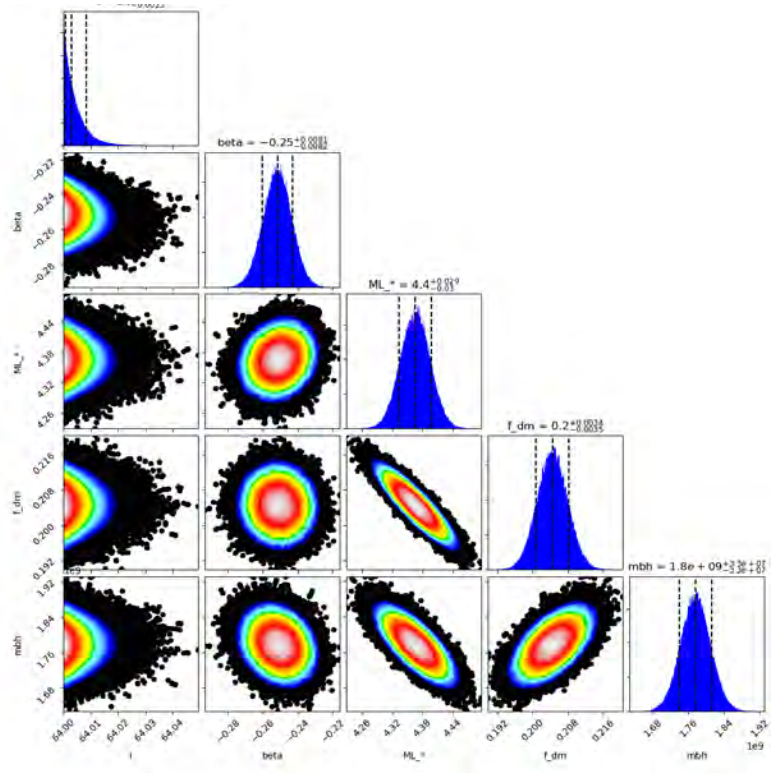

Figure B.6: Our posterior distributions in the stars+NFW halo case (model b) for NGC 5507

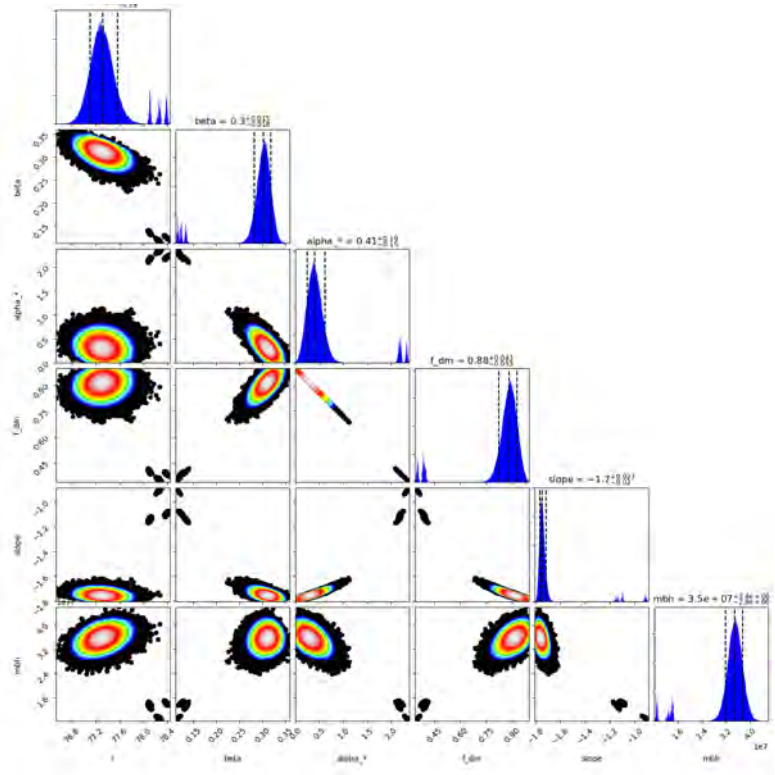

Figure B.7: Our posterior distributions in the stars+gNFW halo case (model c) for NGC 4684. Free parameters are inclination, anisotropy, stellar mass-to-light ratio, dark matter fraction, inner slope of dark matter halo, and black hole mass.

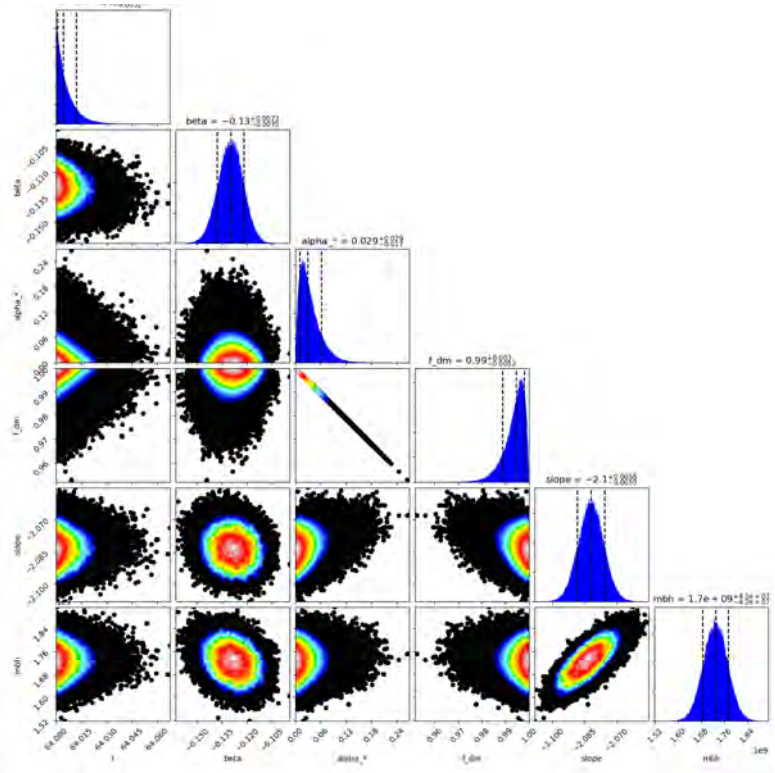

Figure B.8: Our posterior distributions in the stars+gNFW halo case (model c) for NGC 5507

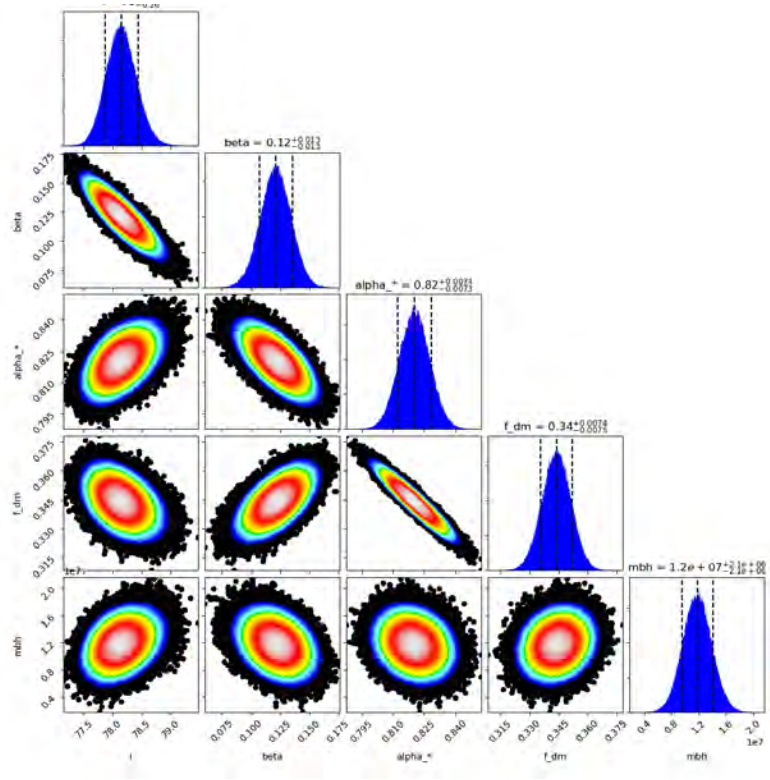

Figure B.9: Our posterior distributions in the rescaled stars+NFW halo case assuming a Salpeter IMF (model d:i) for NGC 4684. Free parameters are inclination, anisotropy, stellar mass scale factor, dark matter fraction and black hole mass.

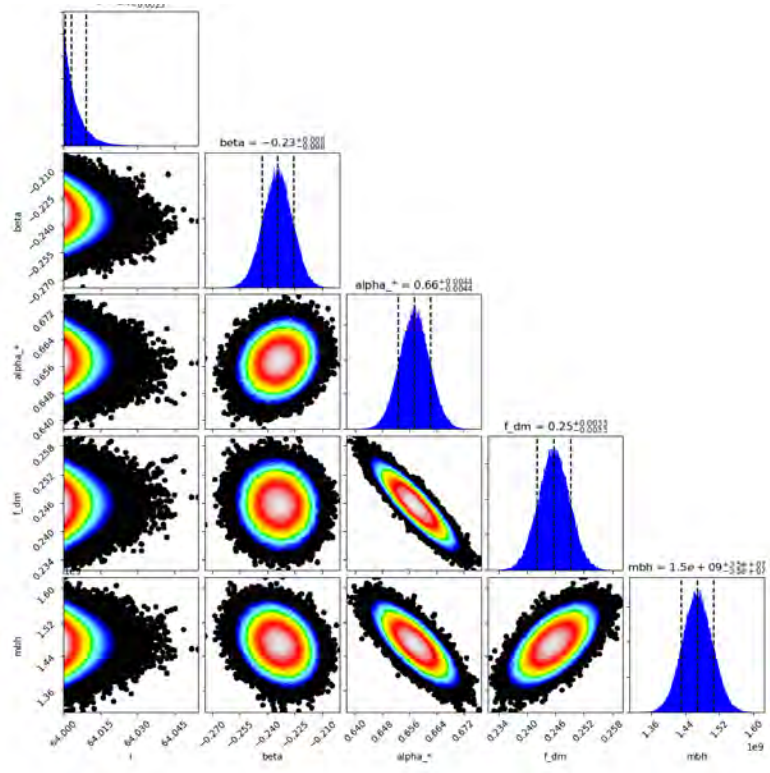

Figure B.10: Our posterior distributions in the rescaled stars+NFW halo case assuming a Salpeter IMF (model d:i) for NGC 5507

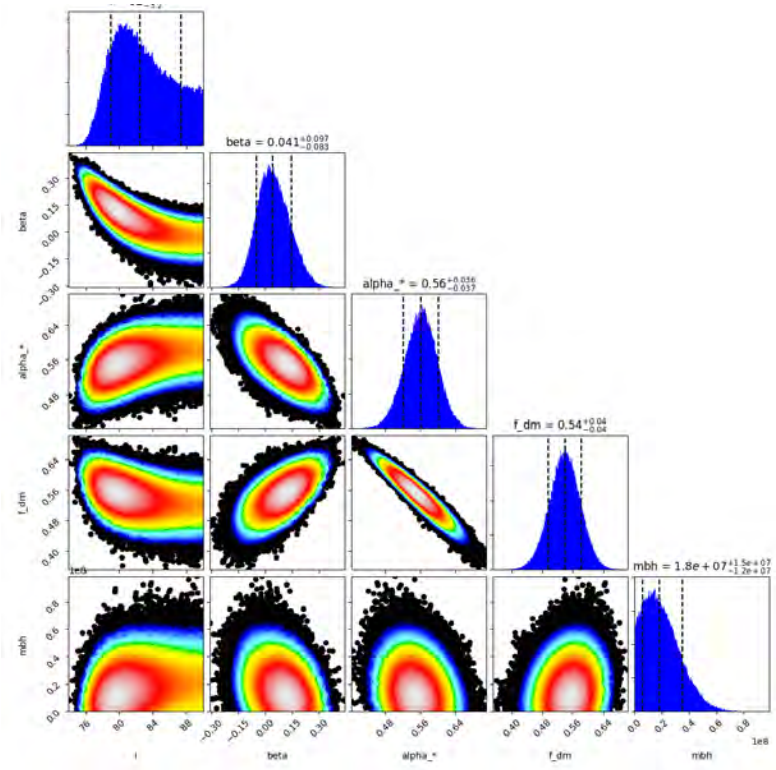

Figure B.11: Our posterior distributions in the rescaled stars+NFW halo case assuming a varying IMF from VD17 (model d:ii) for NGC 4684

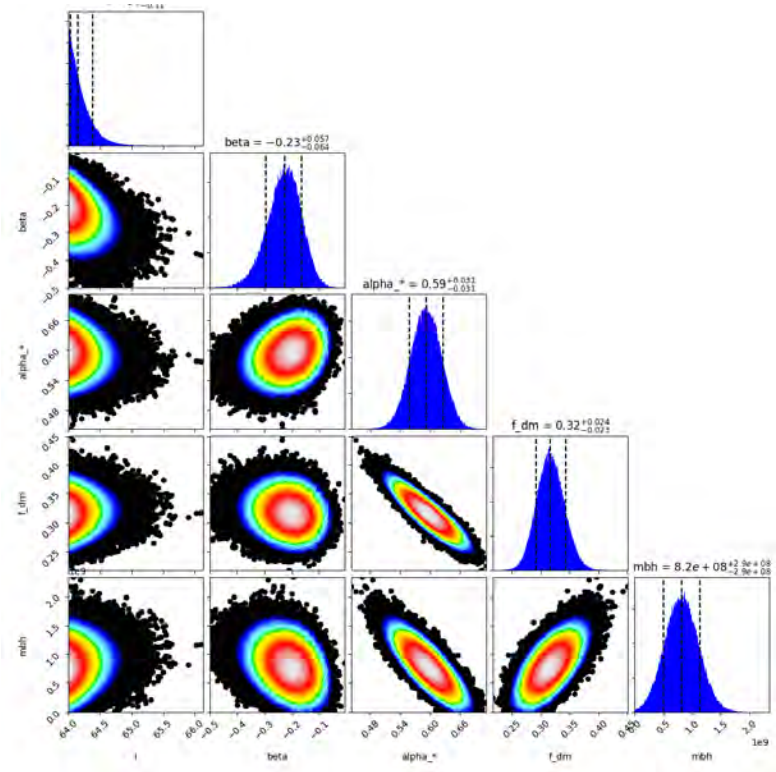

Figure B.12: Our posterior distributions in the rescaled stars+NFW halo case assuming a varying IMF from VD17 (model d:ii) for NGC 5507

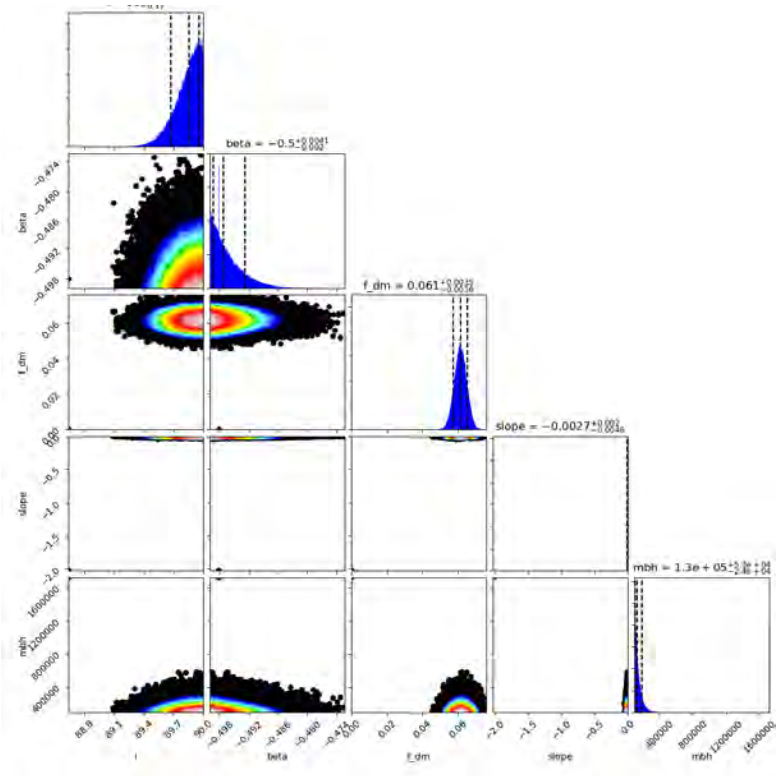

Figure B.13: Our posterior distributions in the stars+gNFW halo case assuming a varying IMF from VD17 (model e) for NGC 4684

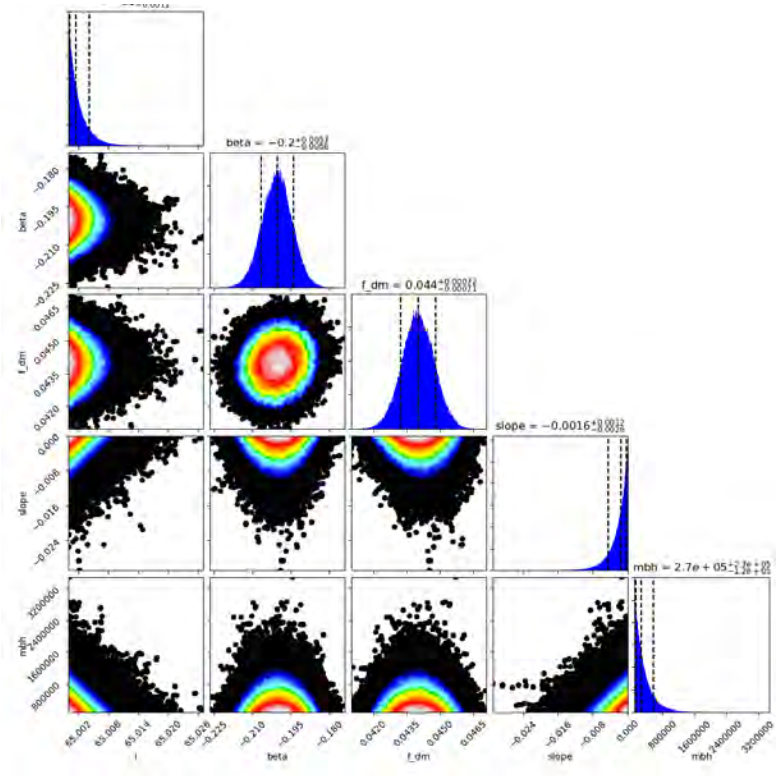

Figure B.14: Our posterior distributions in the stars+gNFW halo case assuming a varying IMF from VD17 (model e) for NGC 5507

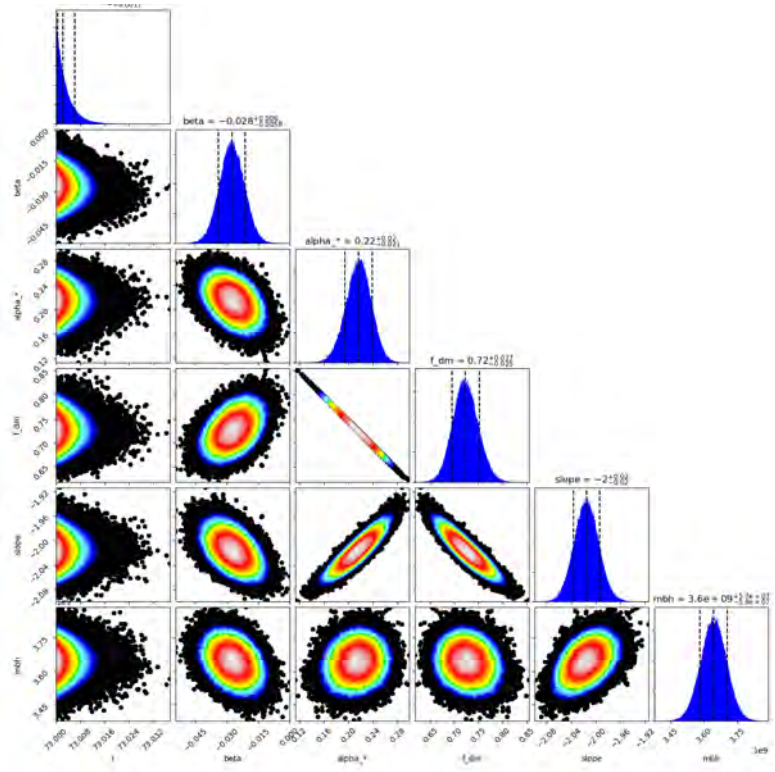

Figure B.15: Our posterior distributions in the stars+gNFW halo case assuming a constant Salpeter IMF (model d) for NGC 2698

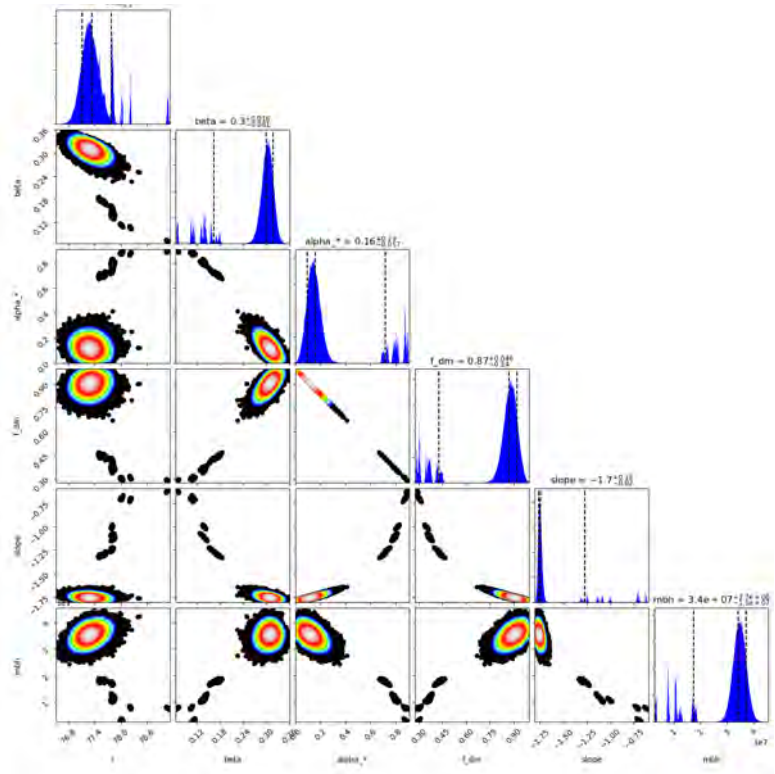

Figure B.16: Our posterior distributions in the stars+gNFW halo case assuming a constant Salpeter IMF (model d) for NGC 4684

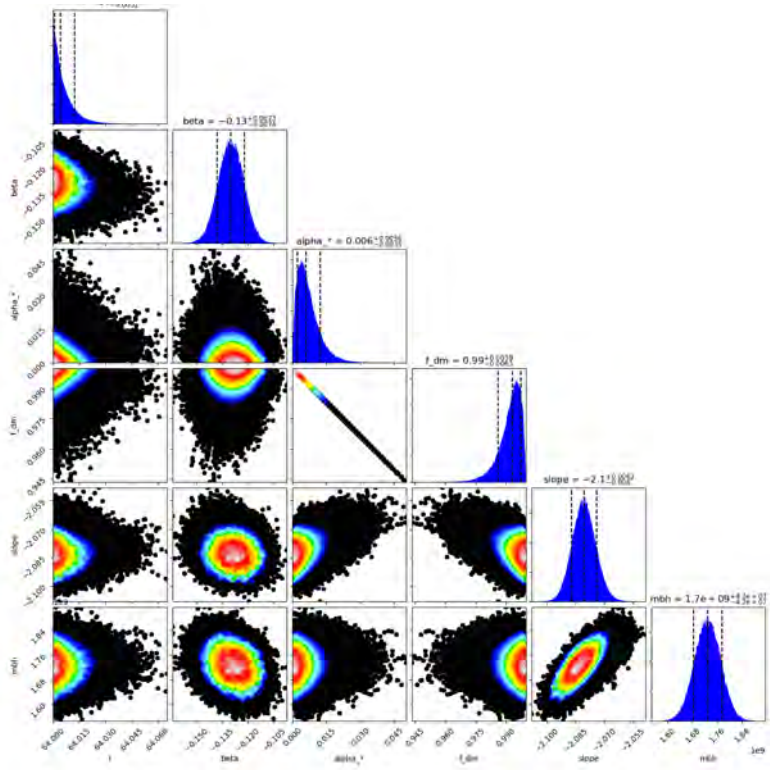

Figure B.17: Our posterior distributions in the stars+gNFW halo case assuming a constant Salpeter IMF (model d) for NGC 5507

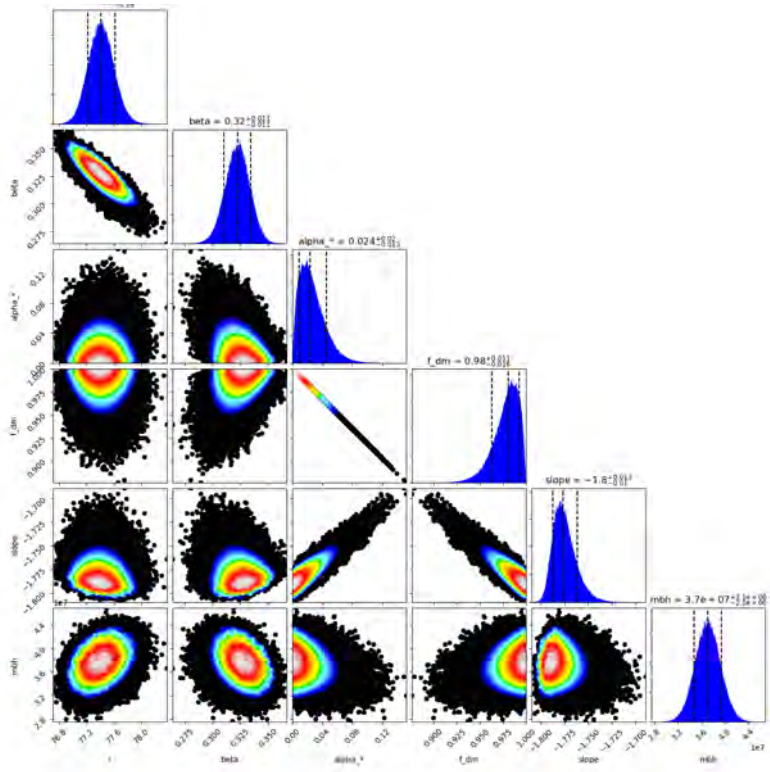

Figure B.18: Our posterior distributions in the stars+gNFW halo case assuming a VD varying IMF (model d) for NGC 4684

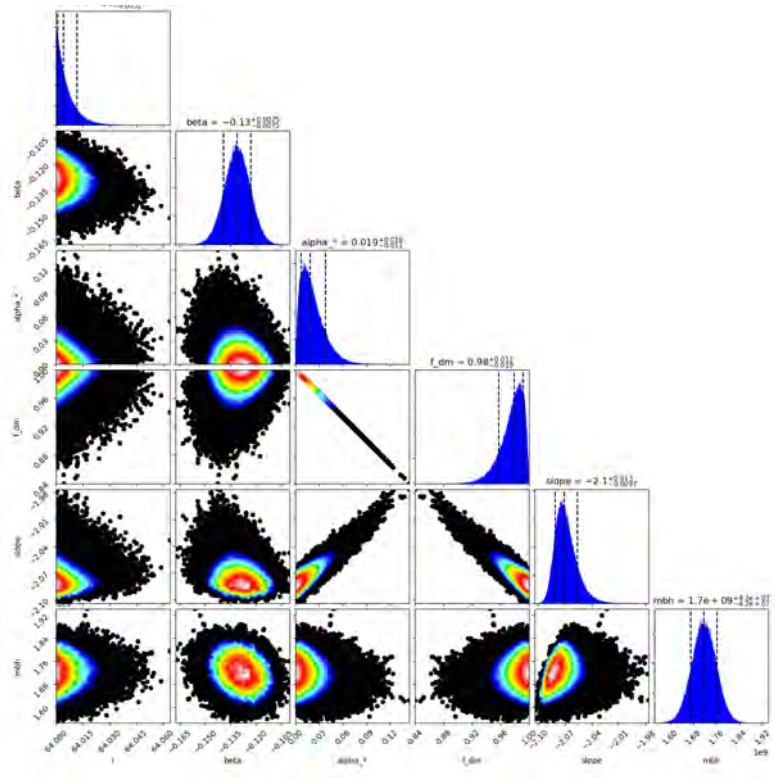

Figure B.19: Our posterior distributions in the stars+gNFW halo case assuming a VD varying IMF (model d) for NGC 5507

C

Appendix C: Inferences on the MUSE galaxy sample using PyStaff

Table C.1: MGEs of the mass density for each galaxy assuming varying age, metallicity and IMF, all measured directly from the data.

NGC 2698			NGC 4684			NGC 5507		
count	σ	q	count	σ	q	count	σ	q
81042.8	0.921369	0.630537	118301.	0.318471	0.583678	258537.	0.318471	0.700000
25649.5	1.85023	0.759746	29491.6	0.692295	0.300000	27039.5	0.908516	0.450000
8436.22	3.48999	0.772121	5407.71	1.31789	0.867357	31821.8	0.936847	0.950000
292.936	7.53714	0.950000	1546.51	3.40747	0.725773	12387.1	1.65574	0.450000
2451.84	10.0330	0.350000	1780.59	6.35236	0.300000	13460.3	2.13521	0.770153
1543.09	15.6139	0.378368	860.371	9.04053	0.300000	3019.10	3.90896	0.950000
267.153	29.0756	0.364836	855.208	9.95530	0.469809	1902.69	5.25914	0.837589
			173.287	17.0366	0.571000	472.910	8.67302	0.808127
			412.054	23.6068	0.300000	98.0882	16.9044	0.950000
			167.761	40.8711	0.300000	776.526	21.1411	0.450000
			46.0323	42.5078	0.557071			

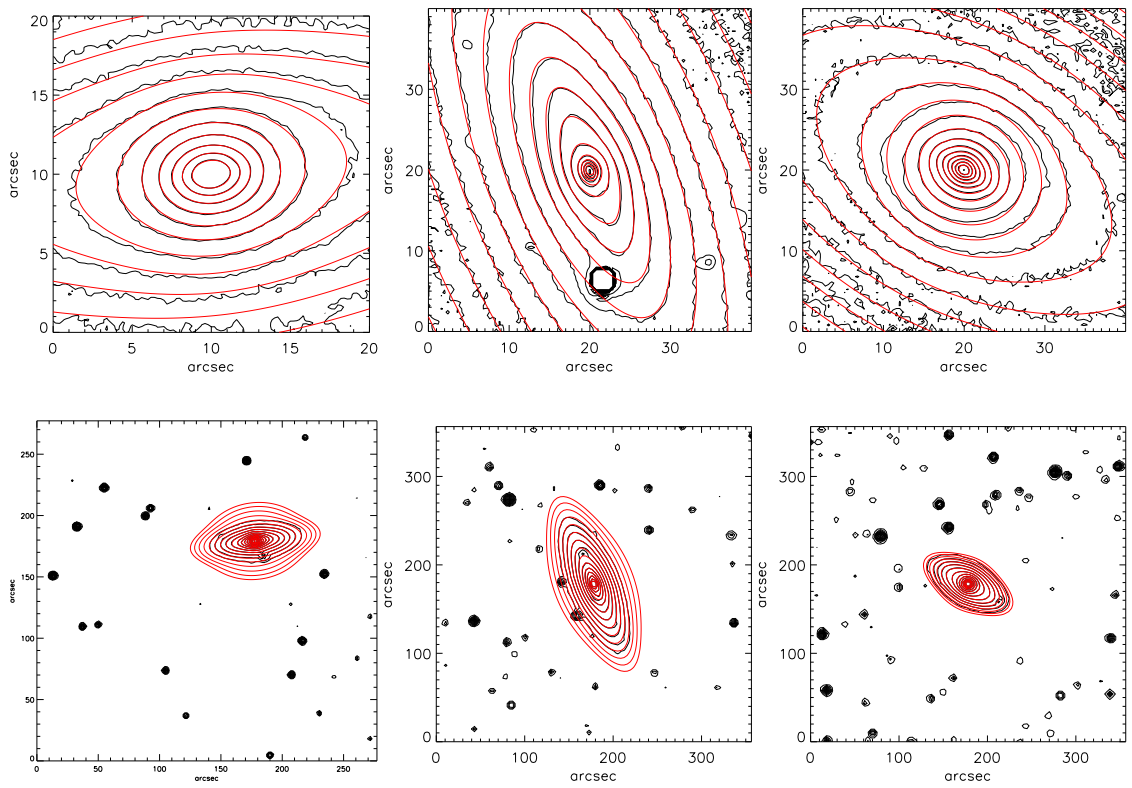

(a) NGC 2698 (b) NGC 4684 (c) NGC 5507

Figure C.1: Mass MGEs for each galaxy. Images are converted from light to mass by measuring the gradients in age metallicity and IMF directly from the data using stellar population models. Black contours are the photometry, and red contours are the best-fitting MGE models. For each galaxy, we show the central region (top) and the entire galaxy (bottom).

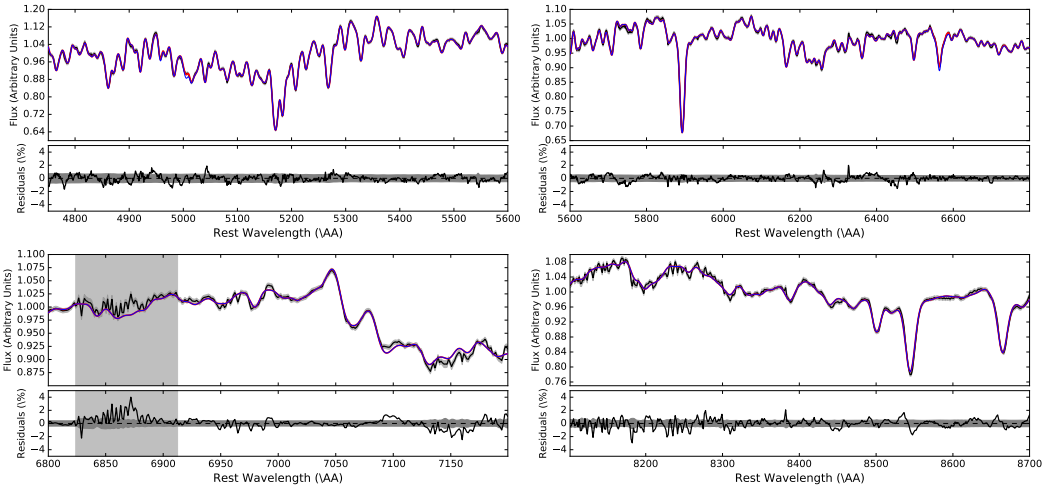

Figure C.2: The Voronoi binned spectra (black) and best fitting model (blue) for the central Voronoi bin for NGC 2698. The residuals are shown beneath each panel. Shaded grey regions are regions of strong telluric contamination and are excluded from the fit.

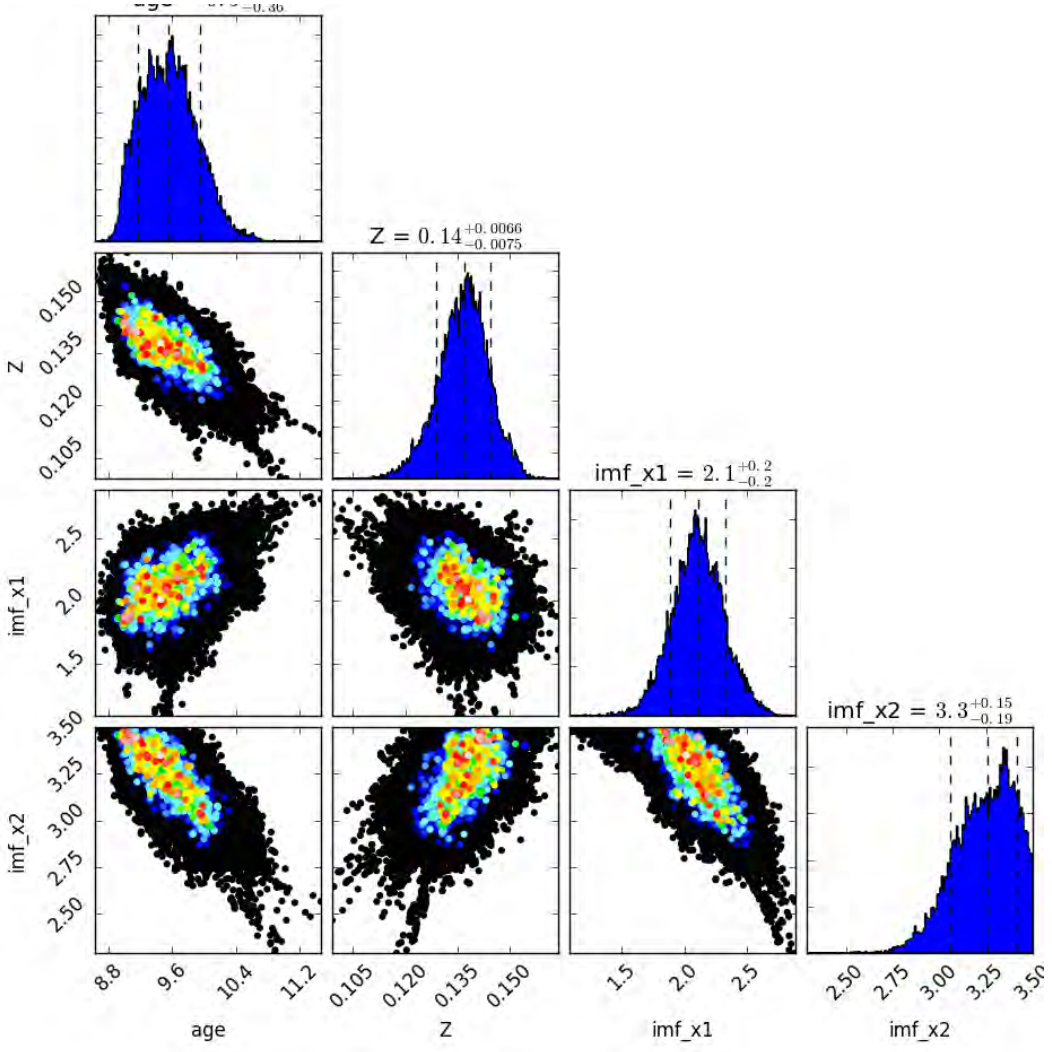

Figure C.3: The posterior distribution of our parameters of interest for NGC 2698, central Voronoi bin.

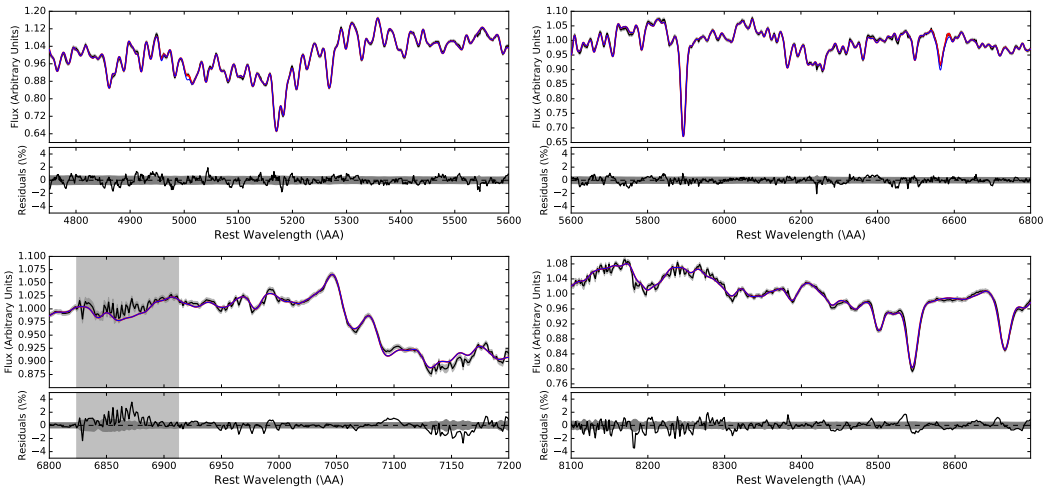

Figure C.4: As in Figure C.2, for Voronoi bin at $r_\epsilon \sim 5''$.

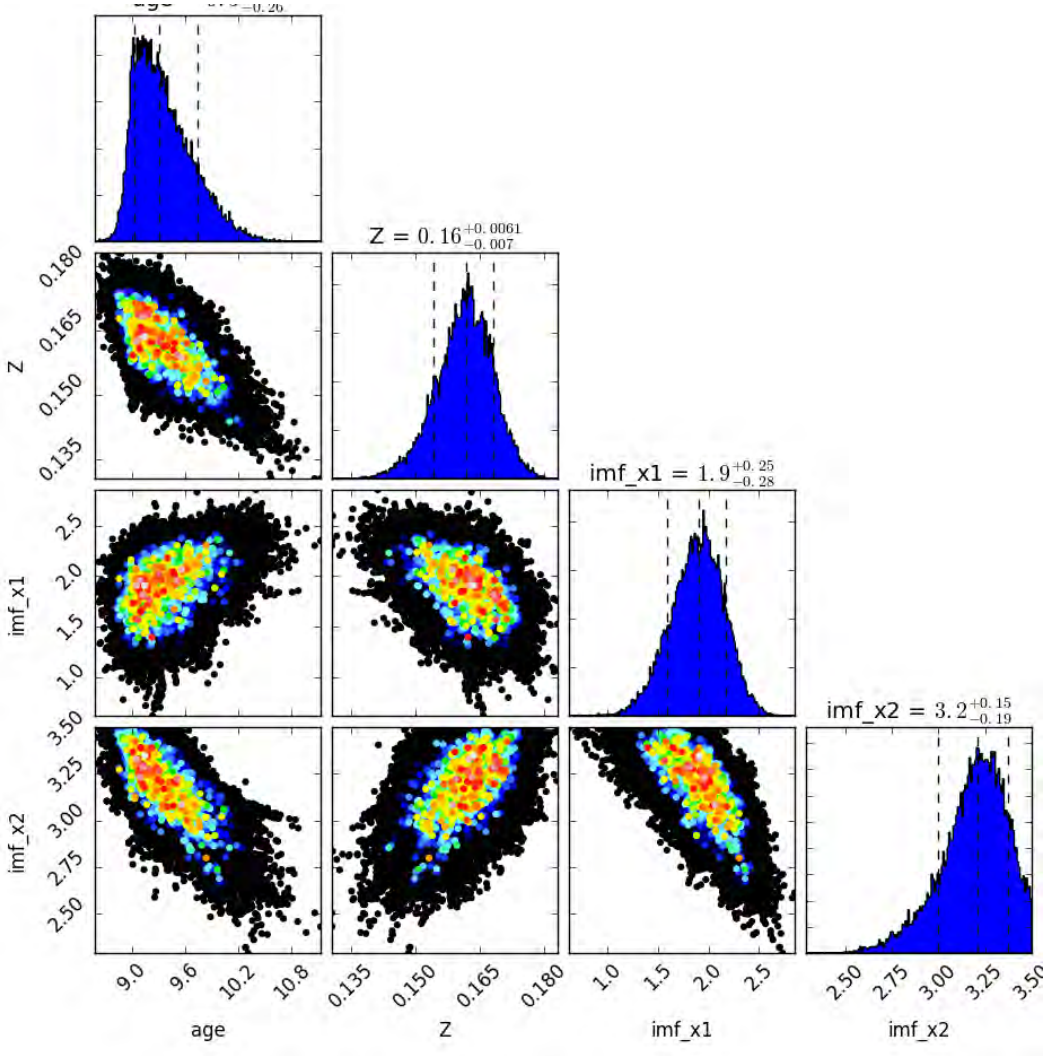

Figure C.5: As in Figure C.3, for Voronoi bin at $r_\epsilon \sim 5''$.

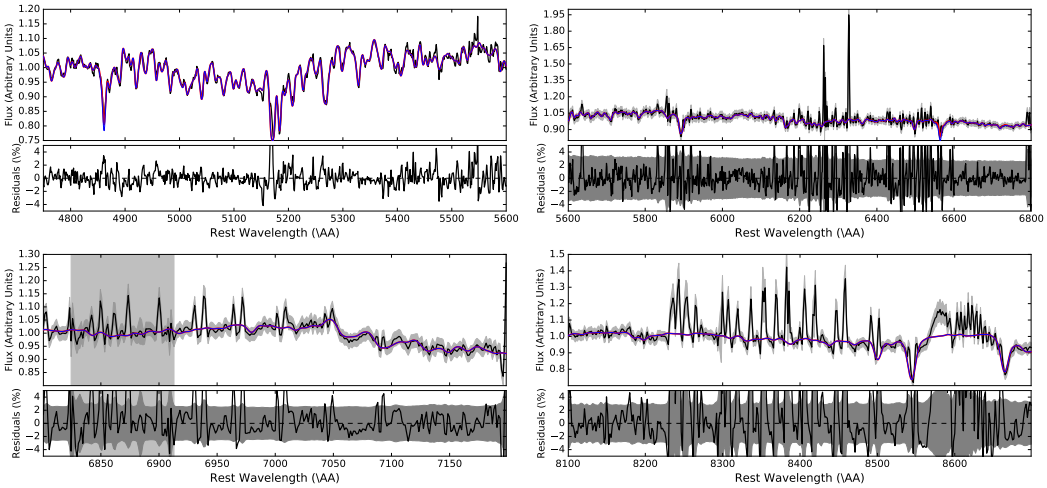

Figure C.6: As in Figure C.2, or Voronoi bin at $r_\epsilon \sim 17''$.

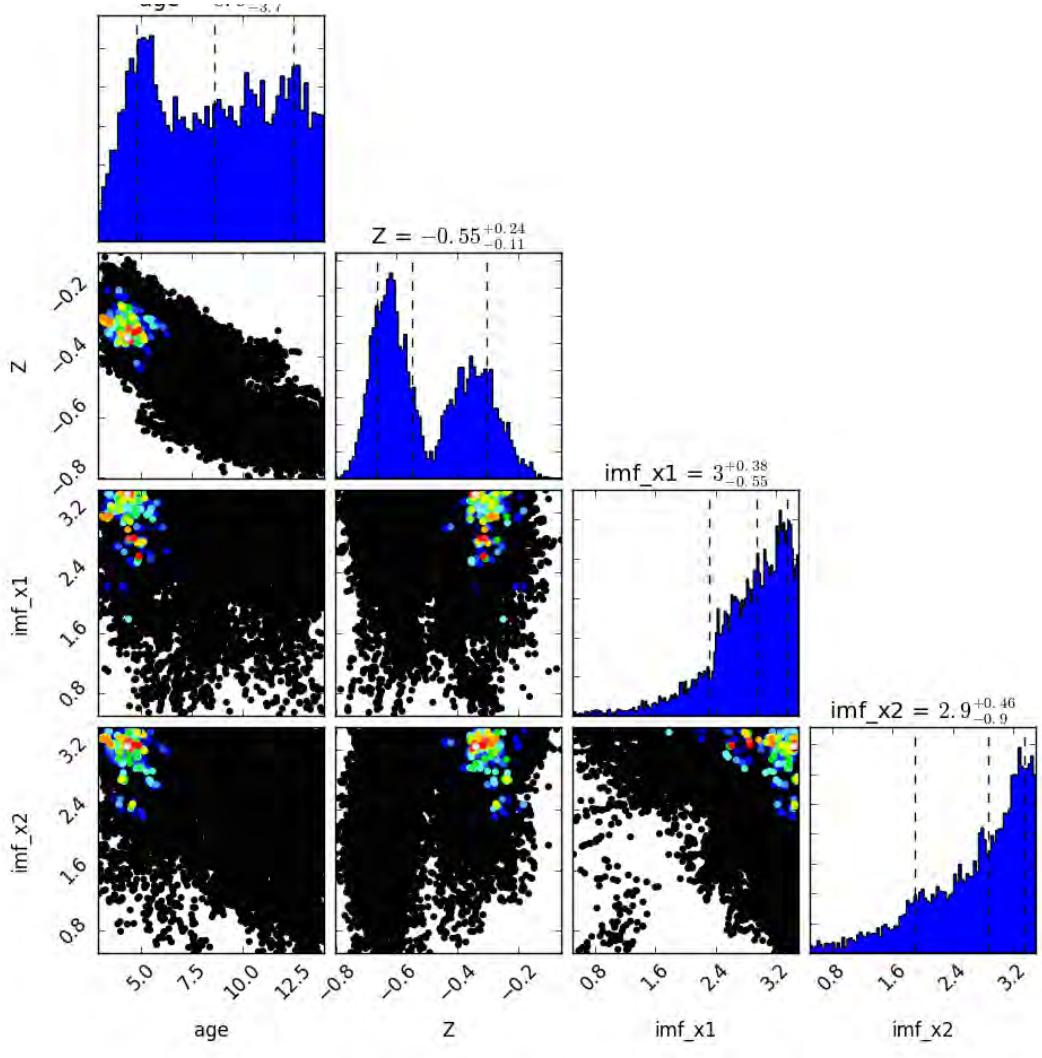

Figure C.7: As in Figure C.3, or Voronoi bin at $r_\epsilon \sim 17''$.

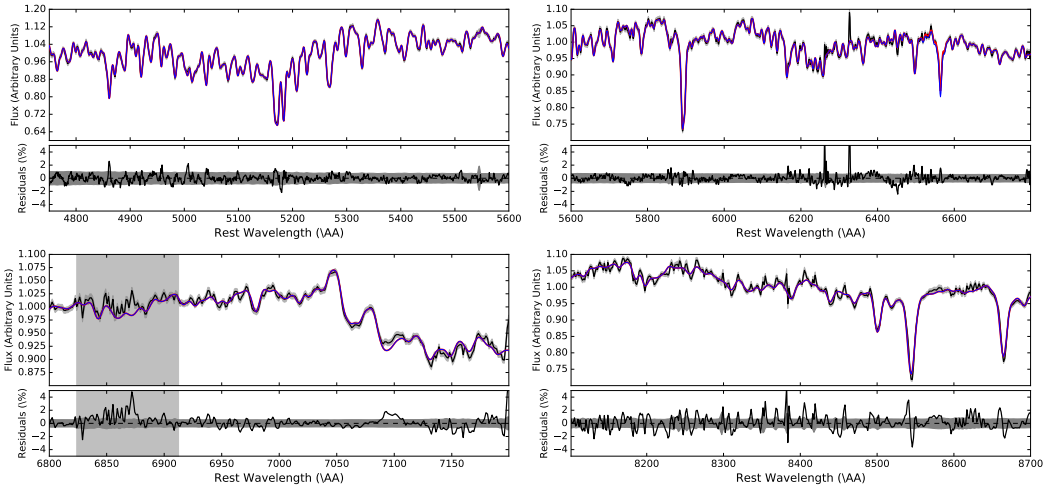

Figure C.8: As in Figure C.2, or Voronoi bin at $r_\epsilon \sim 30''$.

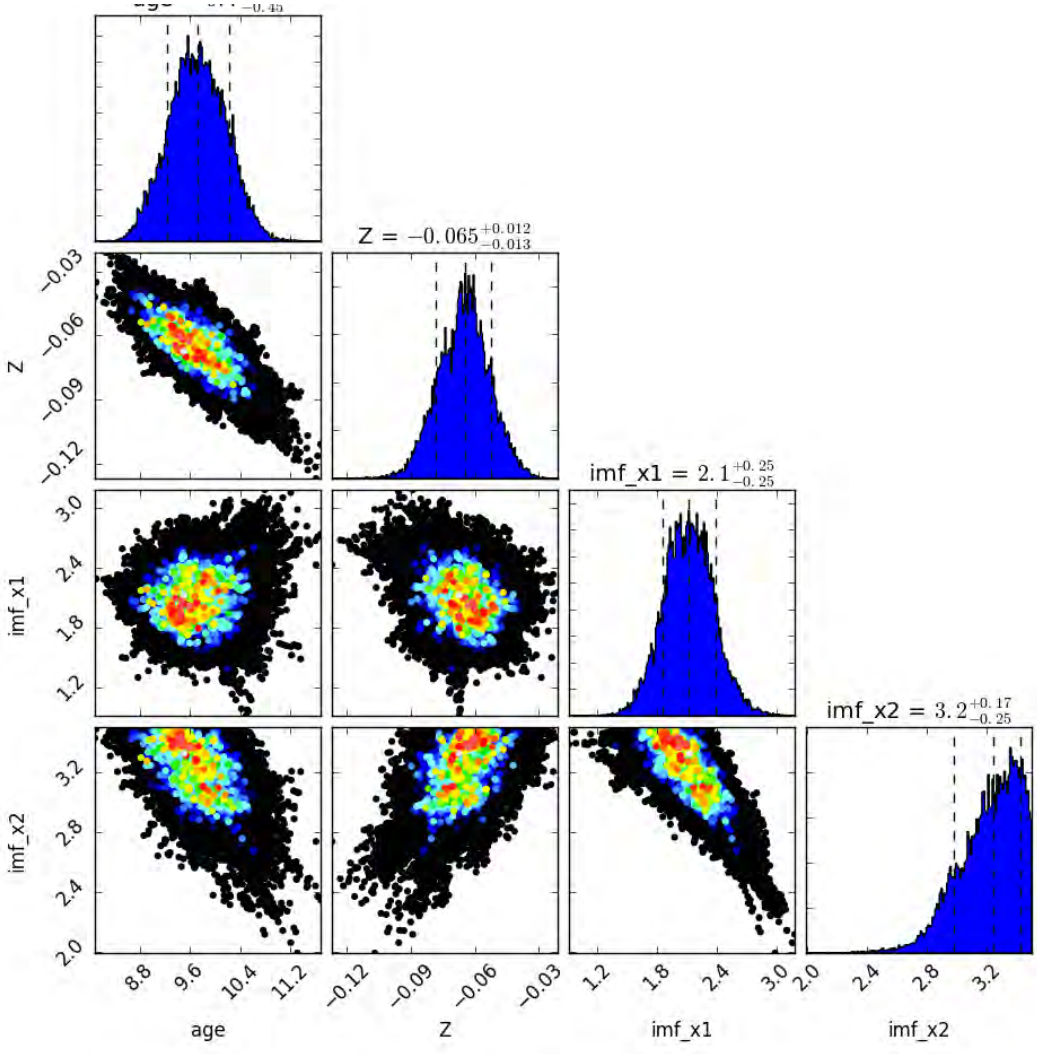

Figure C.9: As in Figure C.3, or Voronoi bin at $r_\epsilon \sim 30''$.

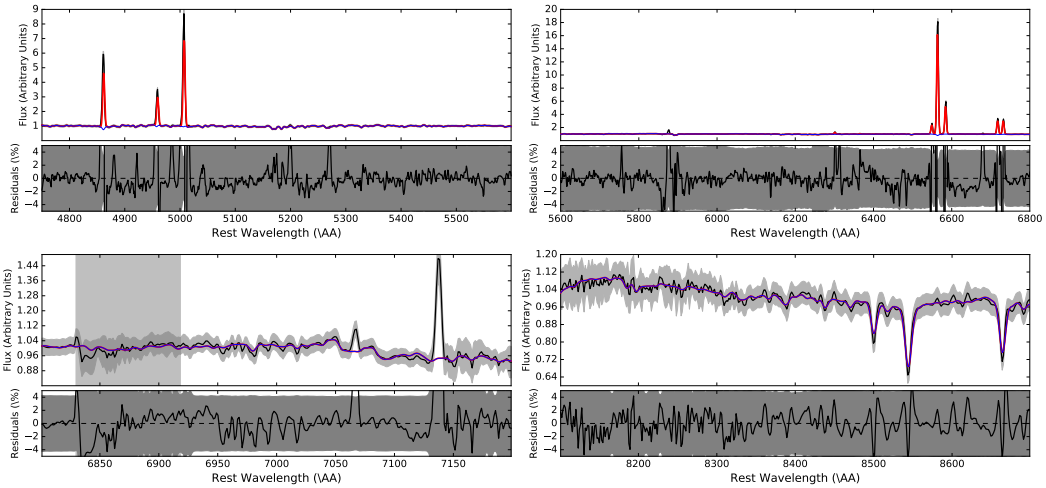

Figure C.10: The Voronoi binned spectra (black) and best fitting model (blue) for the central Voronoi bin for NGC 4684. The residuals are shown beneath each panel. Shaded grey regions are regions of strong telluric contamination and are excluded from the fit.

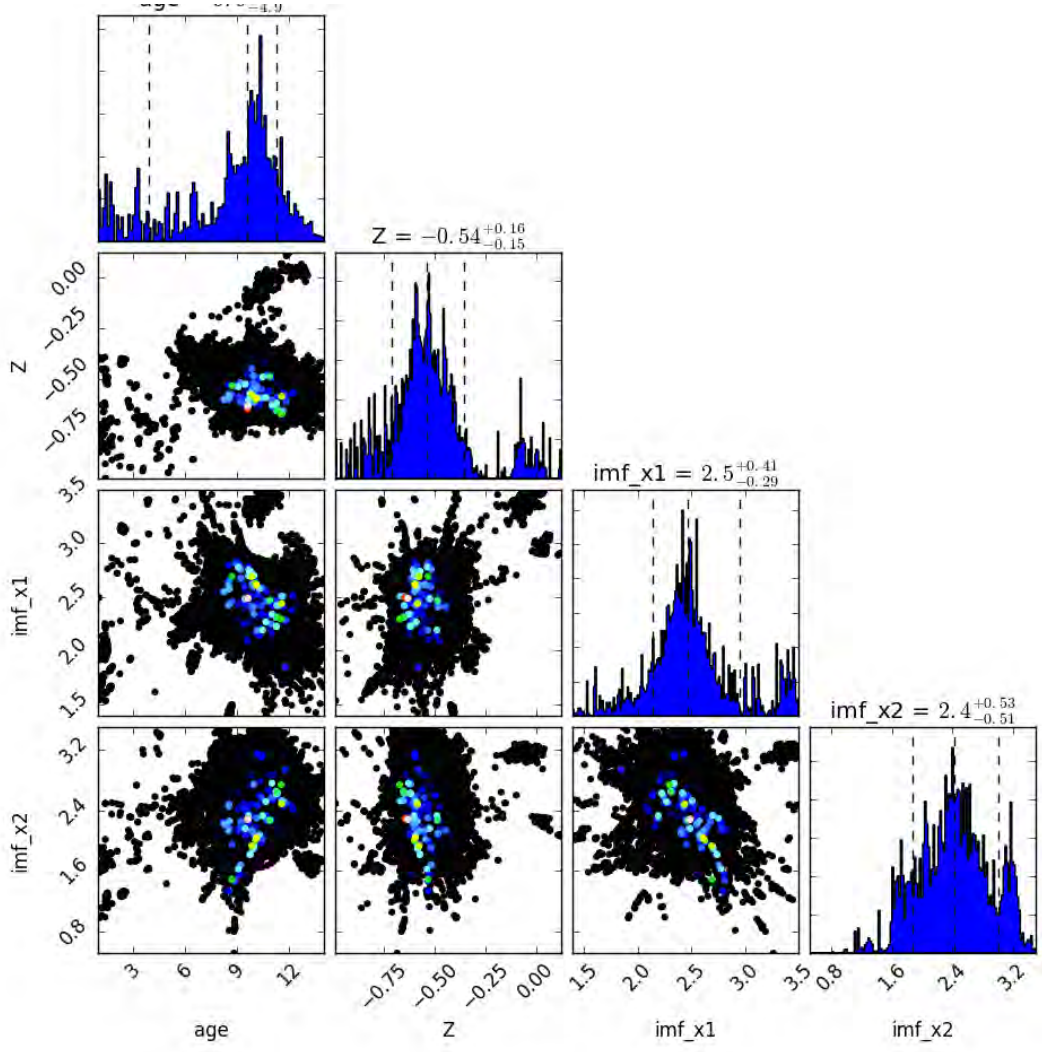

Figure C.11: The posterior distribution of our parameters of interest for NGC 4684, central Voronoi bin.

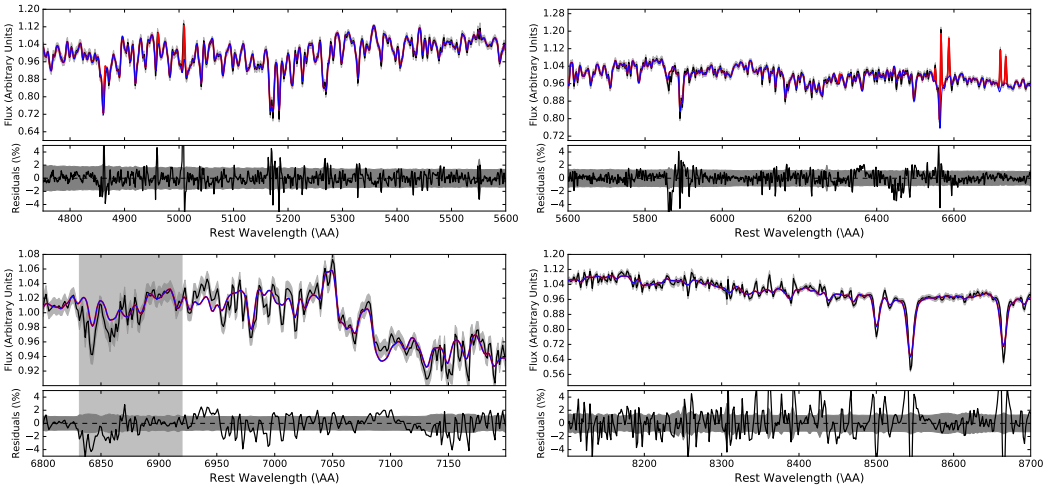

Figure C.12: As in Figure C.10, for Voronoi bin at $r_\epsilon \sim 14''$.

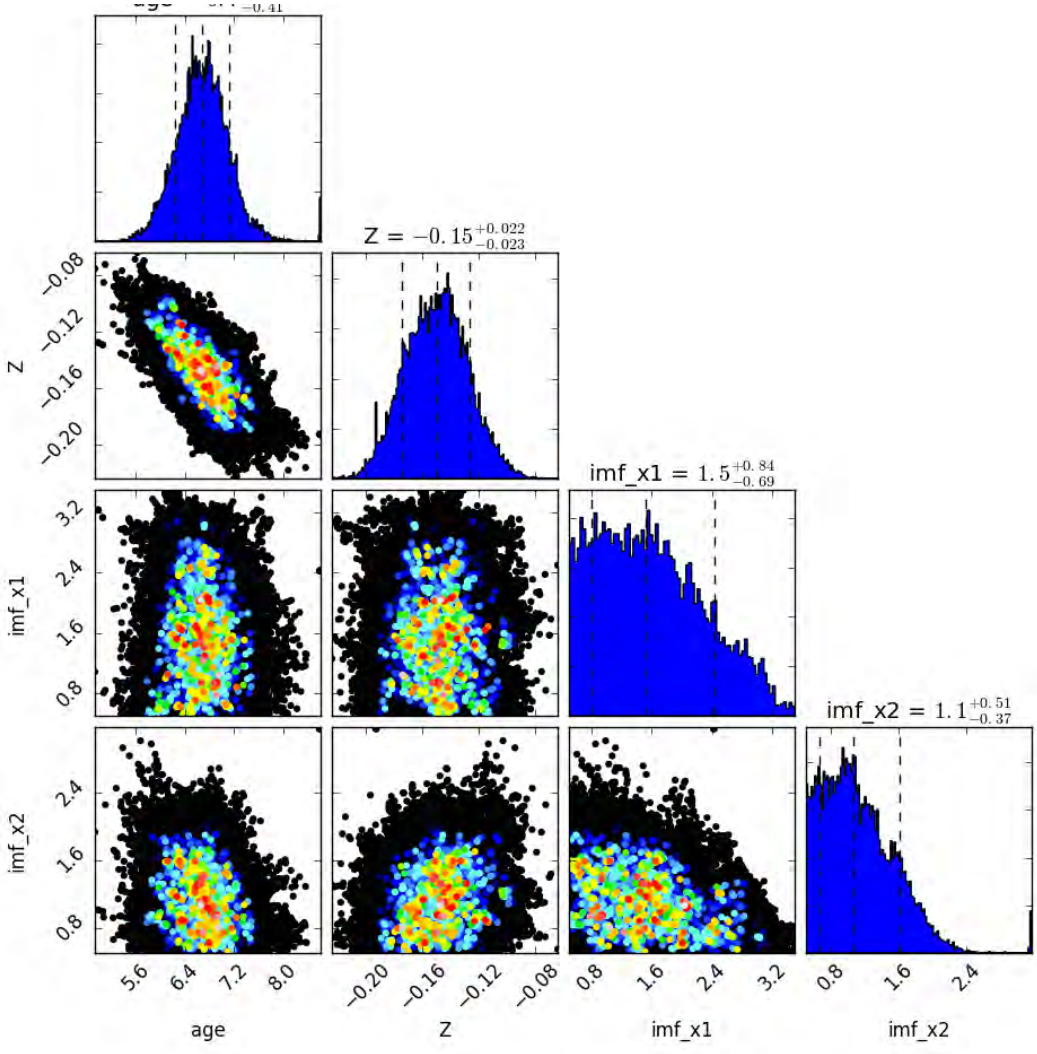

Figure C.13: As in Figure C.11, for Voronoi bin at $r_\epsilon \sim 14''$).

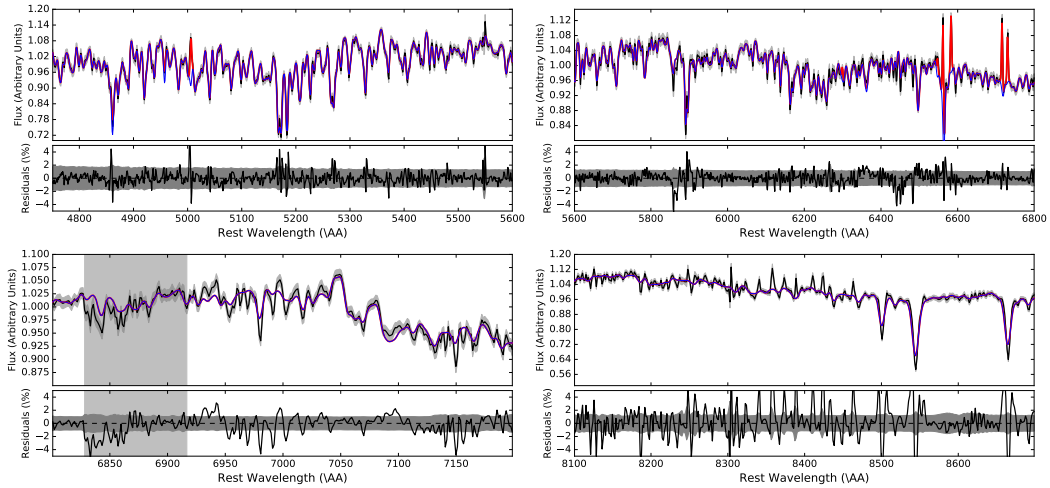

Figure C.14: As in Figure C.10, for Voronoi bin at $r_\epsilon \sim 20''$.

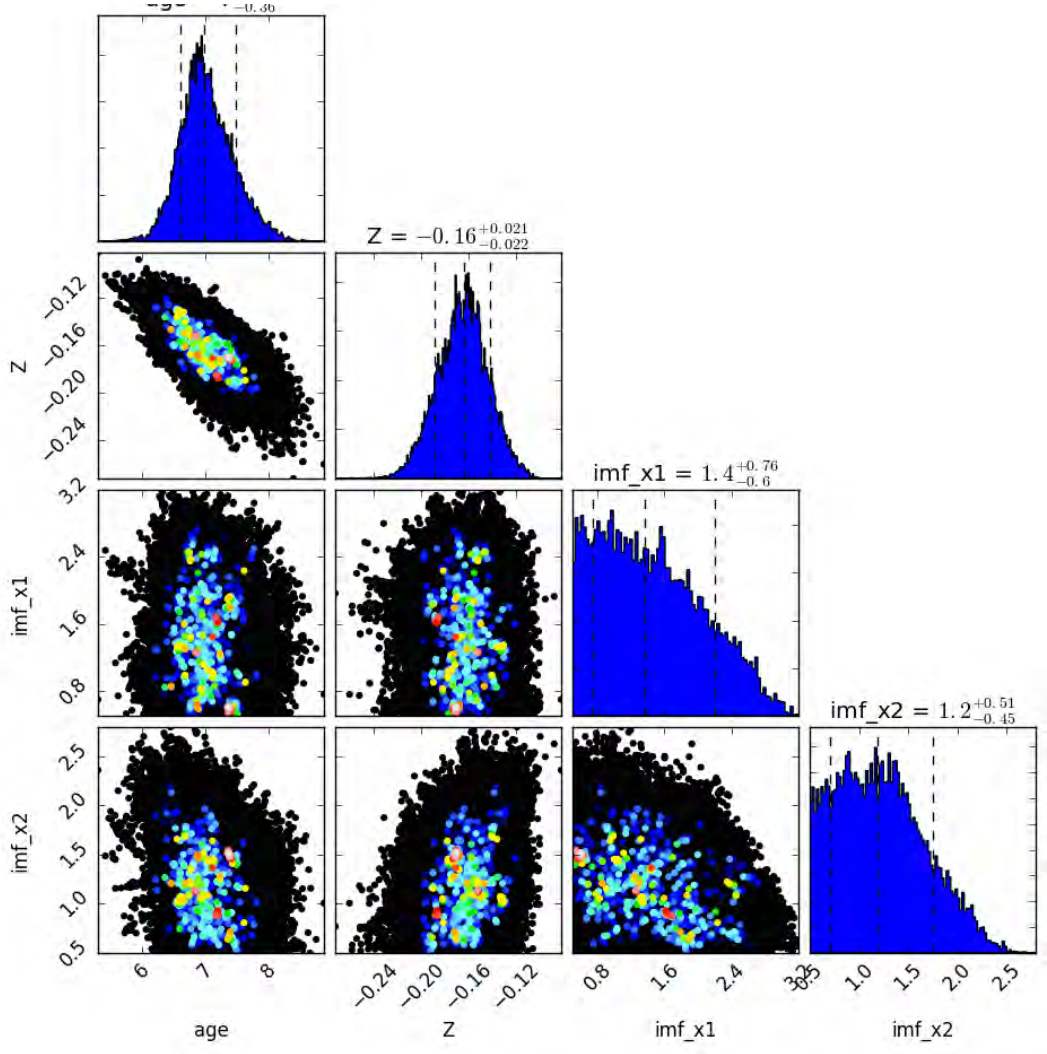

Figure C.15: As in Figure C.11, for Voronoi bin at $r_\epsilon \sim 20''$.

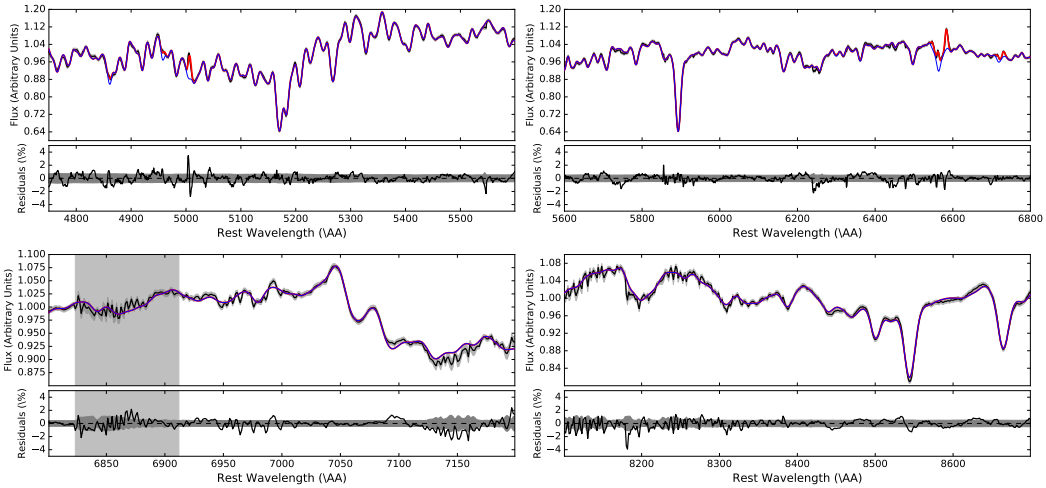

Figure C.16: The Voronoi binned spectra (black) and best fitting model (blue) for the central Voronoi bin for NGC 5507. The residuals are shown beneath each panel. Shaded grey regions are regions of strong telluric contamination and are excluded from the fit.

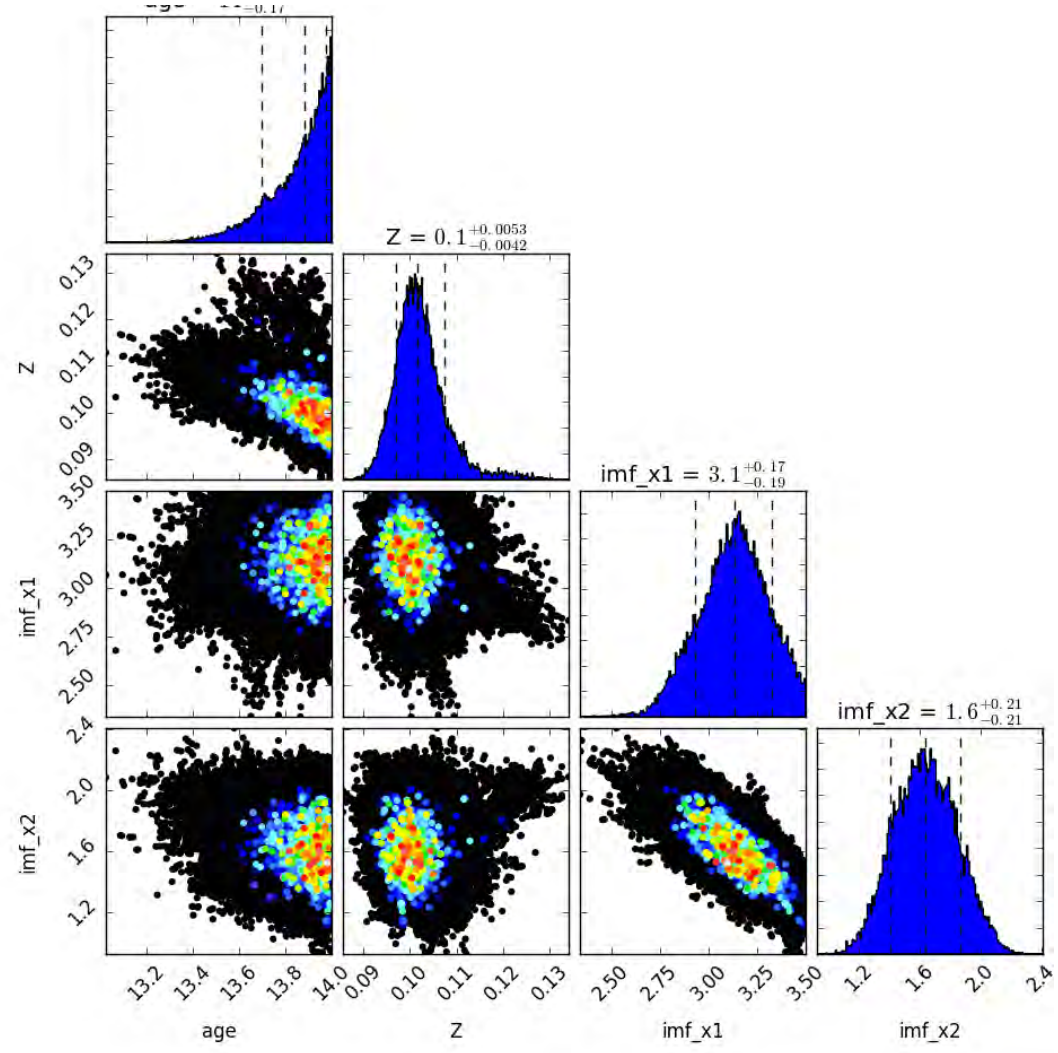

Figure C.17: The posterior distribution of our parameters of interest for NGC 5507, central Voronoi bin.

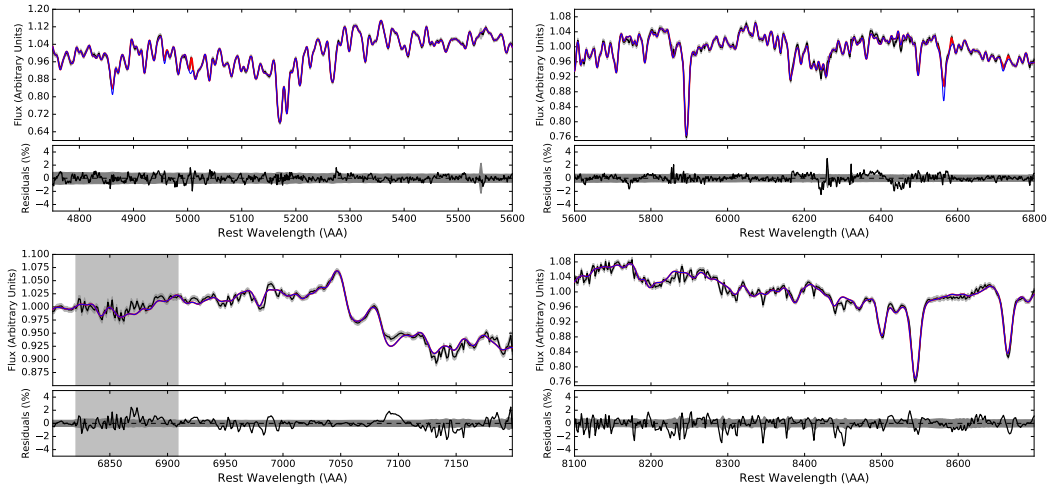

Figure C.18: As in Figure C.16, for Voronoi bin at $r_\epsilon = 5.0$.

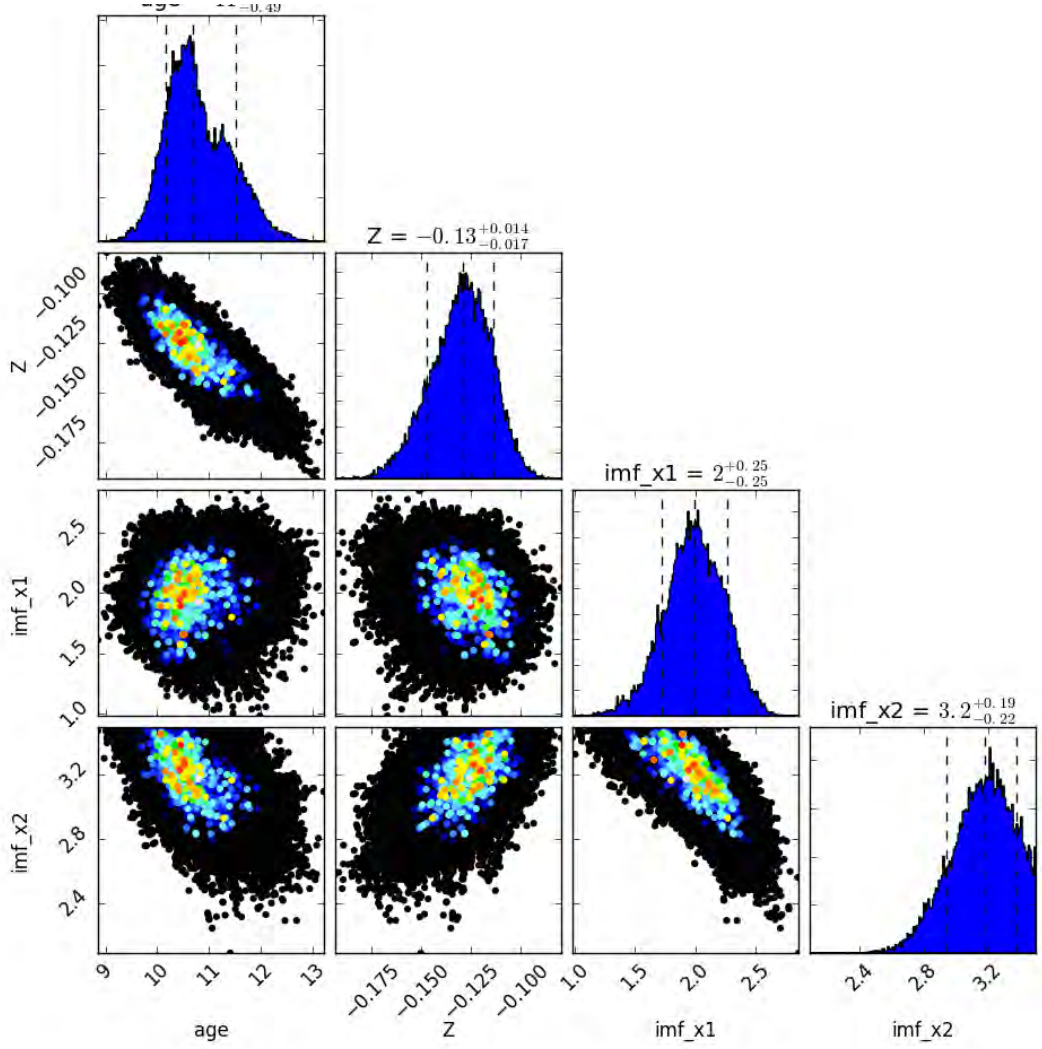

Figure C.19: As in Figure C.17, for Voronoi bin at $r_\epsilon = 5.0$.

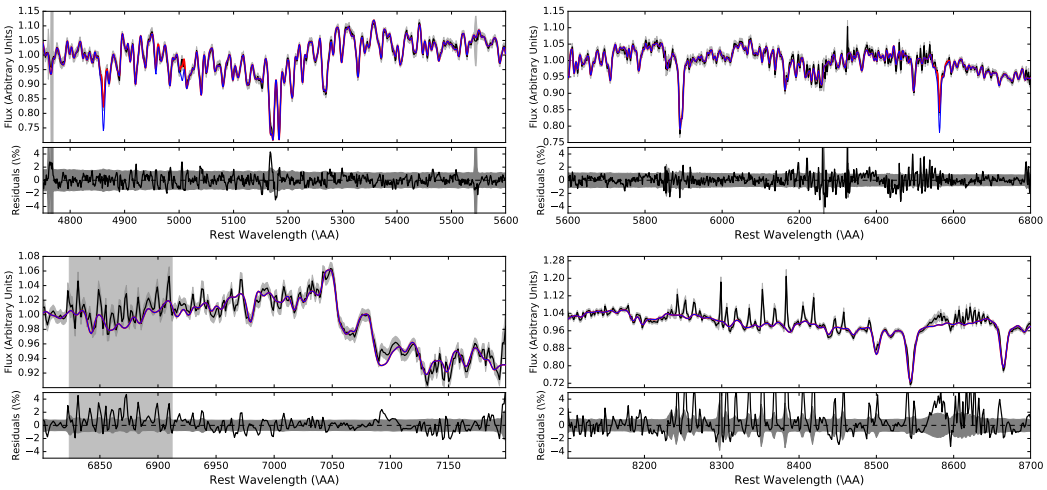

Figure C.20: As in Figure C.16, or Voronoi bin at $r_\epsilon = 19.3$.

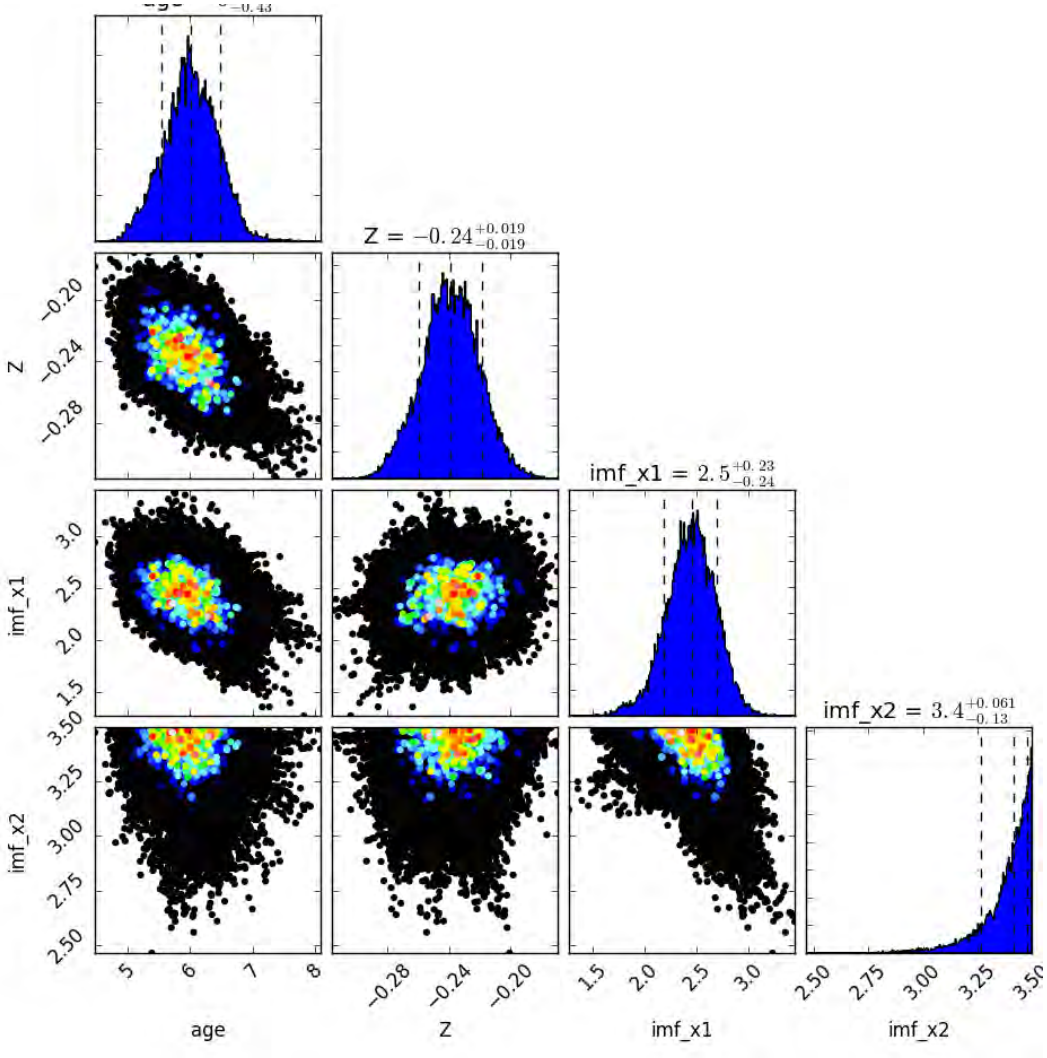

Figure C.21: As in Figure C.17, or Voronoi bin at $r_\epsilon = 19.3$.

References

Abadi M. G., Navarro J. F., Fardal M., Babul A., Steinmetz M., 2010, MNRAS, 407, 435

Abazajian K. N., et al., 2009, ApJS, 182, 543

Alongi M., Bertelli G., Bressan A., Chiosi C., Fagotto F., Greggio L., Nasi E., 1993, A&AS, 97, 851

Alton P. D., Smith R. J., Lucey J. R., 2017, arXiv:1702.05485 [astro-ph]

Andreon S., 2003, A&A, 409, 37

Auger M. W., Treu T., Gavazzi R., Bolton A. S., Koopmans L. V. E., Marshall P. J., 2010, The Astrophysical Journal Letters, 721, L163

Bacon R., et al., 2001, MNRAS, 326, 23

Bacon R., et al., 2010. p. 773508, doi:10.1117/12.856027, http://ads.nao.ac.jp/abs/2010SPIE.7735E..08B

Baldwin C. M., McDermid R. M., Kuntschner H., Maraston C., Conroy C., 2017, preprint, 1709, arXiv:1709.09300

Barbera F. L., Carvalho R. R. d., Gal R. R., Busarello G., Merluzzi P., Capaccioli M., Djorgovski S. G., 2005, ApJ, 626, L19

Bastian N., Covey K. R., Meyer M. R., 2010, ARA&A, 48, 339

Bell E. F., McIntosh D. H., Katz N., Weinberg M. D., 2003, ApJS, 149, 289

Bender R., Saglia R. P., Gerhard O. E., 1994, MNRAS, 269, 785

Bernardi M., et al., 2003, AJ, 125, 1866

Bernardi M., Sheth R. K., Dominguez-Sanchez H., Fischer J.-L., Chae K.-H., Huertas-Company M., Shankar F., 2018, MNRAS, 477, 2560

Blanton M. R., Moustakas J., 2009, ARA&A, 47, 159

Blanton M. R., Roweis S., 2007, AJ, 133, 734

Blumenthal G. R., Faber S. M., Primack J. R., Rees M. J., 1984, Nat, 311, 517

Blumenthal G. R., Faber S. M., Flores R., Primack J. R., 1986, ApJ, 301, 27

Bressan A., Fagotto F., Bertelli G., Chiosi C., 1993, Astronomy and Astrophysics Supplement Series, 100, 647

Bruzual G., Charlot S., 2003, MNRAS, 344, 1000

Bundy K., et al., 2014, ApJ, 798, 7

Bureau M., Athanassoula E., 1999, ApJ, 522, 686

Calzetti D., Armus L., Bohlin R. C., Kinney A. L., Koornneef J., Storchi-Bergmann T., 2000, ApJ, 533, 682

Capozzi D., Maraston C., Daddi E., Renzini A., Strazzullo V., Gobat R., 2016, Monthly Notices of the Royal Astronomical Society, 456, 790

Cappellari M., 2002, Monthly Notices of the Royal Astronomical Society, 333, 400

Cappellari M., 2008, Monthly Notices of the Royal Astronomical Society, 390, 71

Cappellari M., Copin Y., 2003, Monthly Notices of the Royal Astronomical Society, 342, 345

Cappellari M., Emsellem E., 2004, Publications of the Astronomical Society of the Pacific, 116, 138

Cappellari M., et al., 2006, MNRAS, 366, 1126

Cappellari M., et al., 2010. eprint: arXiv:1001.3233, pp 211–214, doi:10.1063/1.3458489, http://ads.nao.ac.jp/abs/2010AIPC.1240..211C

Cappellari M., et al., 2011, MNRAS, 413, 813

Cappellari M., et al., 2012, Nature, 484, 485

Cappellari M., et al., 2013a, MNRAS, 432, 1709

Cappellari M., et al., 2013b, MNRAS, 432, 1862

Cappellari M., et al., 2015, The Astrophysical Journal, 804, L21

Cassisi S., Castellani M., Castellani V., 1997, A&A, 317, 108

Cenarro A. J., et al., 2007, MNRAS, 374, 664

Chabrier G., 2003, PASP, 115, 763

Chen Y.-P., Trager S. C., Peletier R. F., Lançon A., Vazdekis A., Prugniel P., Silva D. R., Gonneau A., 2014, A&A, 565, A117

Chilingarian I., Prugniel P., Sil'Chenko O., Koleva M., 2007. eprint: arXiv:0709.3047, pp 175–176, doi:10.1017/S1743921307007752, http://ads.nao.ac.jp/abs/2007IAUS..241..175C

Choi J., Dotter A., Conroy C., Cantiello M., Paxton B., Johnson B. D., 2016, ApJ, 823, 102

Cid Fernandes R., Mateus A., Sodré L., Stasińska G., Gomes J. M., 2005, Monthly Notices of the Royal Astronomical Society, 358, 363

Colless M., Saglia R. P., Burstein D., Davies R. L., McMahan R. K., Wegner G., 2001, MNRAS, 321, 277

Combes F., Young L. M., Bureau M., 2007, MNRAS, 377, 1795

Conroy C., Gunn J. E., 2010, ApJ, 712, 833

Conroy C., van Dokkum P. G., 2012, ApJ, 760, 71

Conroy C., Gunn J. E., White M., 2009, ApJ, 699, 486

Conroy C., White M., Gunn J. E., 2010, ApJ, 708, 58

Conroy C., van Dokkum P. G., Villaume A., 2017, The Astrophysical Journal, 837, 166

Conroy C., Villaume A., van Dokkum P., Lind K., 2018, arXiv:1801.10185 [astro-ph]

Cooke A., Rodgers B., 2005, in Astronomical Data Analysis Software and Systems XIV. p. 514, http://adsabs.harvard.edu/full/2005ASPC..347..514C

Cortese L., et al., 2016, MNRAS, 463, 170

Cowie L. L., Songaila A., Hu E. M., Cohen J. G., 1996, AJ, 112, 839

Croom S. M., et al., 2012, MNRAS, 421, 872

Davis T. A., et al., 2014, Monthly Notices of the Royal Astronomical Society, 444, 3427

Djorgovski S., Davis M., 1987, ApJ, 313, 59

Dotter A., 2016, The Astrophysical Journal Supplement Series, 222, 8

Dressler A., Lynden-Bell D., Burstein D., Davies R. L., Faber S. M., Terlevich R., Wegner G., 1987, ApJ, 313, 42

Eggen O. J., Lynden-Bell D., Sandage A. R., 1962, ApJ, 136, 748

Emsellem E., Monnet G., Bacon R., 1994, Astronomy and Astrophysics, 285, 723

Emsellem E., et al., 2011, Monthly Notices of the Royal Astronomical Society, 414, 888

Fagotto F., Bressan A., Bertelli G., Chiosi C., 1994, A&AS, 104, 365

Falcón-Barroso J., Sánchez-Blázquez P., Vazdekis A., Ricciardelli E., Cardiel N., Cenarro A. J., Gorgas J., Peletier R. F., 2011, A&A, 532, A95

Ferré-Mateu A., Vazdekis A., Trujillo I., Sánchez-Blázquez P., Ricciardelli E., de la Rosa I. G., 2012, MNRAS, 423, 632

Ferreras I., La Barbera F., de la Rosa I. G., Vazdekis A., de Carvalho R. R., Falcón-Barroso J., Ricciardelli E., 2013, Monthly Notices of the Royal Astronomical Society, 429, L15

Foreman-Mackey D., Hogg D. W., Lang D., Goodman J., 2013, Publications of the Astronomical Society of the Pacific, 125, 306

Freudling W., Romaniello M., Bramich D. M., Ballester P., Forchi V., García-Dabló C. E., Moehler S., Neeser M. J., 2013, A&A, 559, A96

García-Benito R., et al., 2015, A&A, 576, A135

Gerhard O. E., 1993, MNRAS, 265, 213

Girardi L., Bressan A., Bertelli G., Chiosi C., 2000, A&AS, 141, 371

Gnedin O. Y., Kravtsov A. V., Klypin A. A., Nagai D., 2004, ApJ, 616, 16

Goddard D., et al., 2017, Monthly Notices of the Royal Astronomical Society, 465, 688

Gonneau A., et al., 2016, Astronomy and Astrophysics, 589, A36

Goodman J., Weare J., 2010, Communications in Applied Mathematics and Computational Science, Vol. 5, No. 1, p. 65-80, 2010, 5, 65

Gustafsson B., Edvardsson B., Eriksson K., Jørgensen U. G., Nordlund å., Plez B., 2008, Astronomy and Astrophysics, 486, 951

Guth A. H., 1981, Phys. Rev. D, 23, 347

Heavens A. F., Jimenez R., Lahav O., 2000, MNRAS, 317, 965

Hopkins P. F., Bundy K., Murray N., Quataert E., Lauer T. R., Ma C.-P., 2009, MNRAS, 398, 898

Horne K., 1986, Publications of the Astronomical Society of the Pacific, 98, 609

Hubble E. P., 1926, ApJ, 64, 321

Hudson M. J., Lucey J. R., Smith R. J., Steel J., 1997, MNRAS, 291, 488

Hutchinson T. A., et al., 2016, The Astronomical Journal, 152, 205

Kaviraj S., et al., 2008, MNRAS, 388, 67

Koleva M., Prugniel P., Ocvirk P., Le Borgne D., Soubiran C., 2008, Monthly Notices of the Royal Astronomical Society, 385, 1998

Kormendy J., Ho L. C., 2013, ARA&A, 51, 511

Krajnović D., McDermid R. M., Cappellari M., Davies R. L., 2009, MNRAS, 399, 1839

Krajnović D., et al., 2011, Monthly Notices of the Royal Astronomical Society, 414, 2923

Kriek M., et al., 2010, ApJ, 722, L64

Kroupa P., 2001, Monthly Notices of the Royal Astronomical Society, 322, 231

Kuntschner H., 2004, A&A, 426, 737

Kuntschner H., et al., 2010, MNRAS, 408, 97

Kurucz R. L., 1970, SAO Special Report, 309, 309

Kurucz R., 1993, ATLAS9 Stellar Atmosphere Programs and 2 km/s grid. Kurucz CD-ROM No. 13. Cambridge, Mass.: Smithsonian Astrophysical Observatory, 1993., 13

La Barbera F., Ferreras I., Vazdekis A., de la Rosa I. G., de Carvalho R. R., Trevisan M., Falcon-Barroso J., Ricciardelli E., 2013, MNRAS, 433, 3017

La Barbera F., Vazdekis A., Ferreras I., Pasquali A., Cappellari M., Martín-Navarro I., Schönebeck F., Falcón-Barroso J., 2016, MNRAS, 457, 1468

Lançon A., 1998, arXiv preprint astro-ph/9810474

Lançon A., Mouhcine M., 2002, A&A, 393, 167

Larson R. B., 1975, MNRAS, 173, 671

Larson R. B., Tinsley B. M., 1978, ApJ, 219, 46

Le Borgne J.-F., et al., 2003, A&A, 402, 433

Lejeune T., Schaerer D., 2001, A&A, 366, 538

Lejeune T., Cuisinier F., Buser R., 1997, A&AS, 125, 229

Lejeune T., Cuisinier F., Buser R., 1998, A&AS, 130, 65

Lemson G., Consortium t. V., 2006, arXiv:astro-ph/0608019

Leung G. Y. C., et al., 2018, MNRAS, 477, 254

Li H., Li R., Mao S., Xu D., Long R. J., Emsellem E., 2016, MNRAS, 455, 3680

Lord S., 1992, ATRAN

Lyubenova M., Kuntschner H., Rejkuba M., Silva D. R., Kissler-Patig M., Tacconi-Garman L. E., 2012, A&A, 543, A75

Lyubenova M., et al., 2016, arXiv:1606.07448 [astro-ph]

MacArthur L. A., McDonald M., Courteau S., González J. J., 2010, ApJ, 718, 768

Madau P., Dickinson M., 2014, ARA&A, 52, 415

Maksym W. P., Ulmer M. P., Roth K. C., Irwin J. A., Dupke R., Ho L. C., Keel W. C., Adami C., 2014, MNRAS, 444, 866

Maraston C., 1998, MNRAS, 300, 872

Maraston C., 2005, MNRAS, 362, 799

Maraston C., Strömbäck G., 2011, MNRAS, 418, 2785

Maraston C., Daddi E., Renzini A., Cimatti A., Dickinson M., Papovich C., Pasquali A., Pirzkal N., 2006, ApJ, 652, 85

Marigo P., Girardi L., 2007, Astronomy and Astrophysics, 469, 239

Marigo P., Girardi L., Bressan A., Groenewegen M. A. T., Silva L., Granato G. L., 2008, A&A, 482, 883

Mármol-Queraltó E., Cardiel N., Cenarro A. J., Vazdekis A., Gorgas J., Pedraz S., Peletier R. F., Sánchez-Blázquez P., 2008, A&A, 489, 885

Martin-Navarro I., Barbera F. L., Vazdekis A., Falcon-Barroso J., Ferreras I., 2014, MNRAS, 447, 1033

Martín-Navarro I., Barbera F. L., Vazdekis A., Falcón-Barroso J., Ferreras I., 2015, MNRAS, 447, 1033

McConnell N. J., Lu J. R., Mann A. W., 2016, The Astrophysical Journal, 821, 39

McDermid R. M., et al., 2014, ApJ, 792, L37

McDermid R. M., et al., 2015, MNRAS, 448, 3484

Mentz J., et al., 2016, MNRAS, 463, 2819

Mitzkus M., Cappellari M., Walcher C. J., 2017, Monthly Notices of the Royal Astronomical Society, 464, 4789

Monnet G., Bacon R., Emsellem E., 1992, A&A, 253, 366

Naab T., Johansson P. H., Ostriker J. P., 2009, ApJL, 699, L178

Navarro J. F., Eke V. R., Frenk C. S., 1996, MNRAS, 283, L72

Navarro J. F., Frenk C. S., White S. D. M., 1997, The Astrophysical Journal, 490, 493

Ocvirk P., Pichon C., Lançon A., Thiébaut E., 2006, MNRAS, 365, 46

Origlia L., Oliva E., 2000a, arXiv preprint astro-ph/0003131

Origlia L., Oliva E., 2000b, New Astronomy Reviews, 44, 257

Parikh T., et al., 2018, MNRAS, 477, 3954

Pecaut M. J., Mamajek E. E., 2013, ApJS, 208, 9

Peletier R. F., Valentijn E. A., 1989, Astrophysics and Space Science, 156, 127

Peletier R. F., Valentijn E. A., Moorwood A. F. M., Freudling W., Knapen J. H., Beckman J. E., 1995, A&A, 300, L1

Pickles A. J., 1998, Publications of the Astronomical Society of the Pacific, 110, 863

Pietrinferni A., Cassisi S., Salaris M., Castelli F., 2004, ApJ, 612, 168

Pietrinferni A., Cassisi S., Salaris M., Percival S., Ferguson J. W., 2009, ApJ, 697, 275

Poci A., Cappellari M., McDermid R. M., 2017, Monthly Notices of the Royal Astronomical Society, 467, 1397

Press W. H., Teukolsky S. A., Vetterling W. T., Flannery B. P., 1992, Numerical recipes in FORTRAN. The art of scientific computing. http://adsabs.harvard.edu/abs/1992nrfa.book.....P

Prugniel P., Soubiran C., Koleva M., Le Borgne D., 2007, ArXiv Astrophysics e-prints, p. 3658

Rayner J. T., Cushing M. C., Vacca W. D., 2009, ApJS, 185, 289

Renzini A., 1981, Ann. de Phys., 6, 87

Riffel R., Ruschel-Dutra D., Pastoriza M. G., Rodríguez-Ardila A., Santos Jr J. F. C., Bonatto C. J., Ducati J. R., 2011, MNRAS, 410, 2714

Riffel R., et al., 2015, Monthly Notices of the Royal Astronomical Society, 450, 3069

Roberts M. S., Haynes M. P., 1994, ARA&A, 32, 115

Röck B., Vazdekis A., Peletier R. F., Knapen J. H., Falcón-Barroso J., 2015, MNRAS, 449, 2853

Röck B., Vazdekis A., Ricciardelli E., Peletier R. F., Knapen J. H., Falcón-Barroso J., 2016, A&A, 589, A73

Rosani G., Pasquali A., La Barbera F., Ferreras I., Vazdekis A., 2018, MNRAS, 476, 5233

Sánchez-Blázquez P., et al., 2006, MNRAS, 371, 703

Sánchez S. F., et al., 2012, A&A, 538, A8

Sarzi M., Spiniello C., La Barbera F., Krajnović D., van den Bosch R., 2018, MNRAS, 478, 4084

Saunders W., et al., 1991, Nat, 349, 32

Schiavon R. P., 2007, ApJS, 171, 146

Schlafly E. F., Finkbeiner D. P., 2011, ApJ, 737, 103

Scott N., et al., 2009, MNRAS, 398, 1835

Scott N., et al., 2013, Monthly Notices of the Royal Astronomical Society, 432, 1894

Searle L., Sargent W. L. W., Bagnuolo W. G., 1973, ApJ, 179, 427

Serra P., Trager S. C., 2007, MNRAS, 374, 769

Shectman S. A., Landy S. D., Oemler A., Tucker D. L., Lin H., Kirshner R. P., Schechter P. L., 1996, ApJ, 470, 172

Silva D. R., Kuntschner H., Lyubenova M., 2008, ApJ, 674, 194

Skrutskie M. F., et al., 2006, The Astronomical Journal, 131, 1163

Smith R. J., 2014, MNRAS, 443, L69

Smith R. J., Alton P., Lucey J. R., Conroy C., Carter D., 2015, Monthly Notices of the Royal Astronomical Society, 454, L71

Soto K. T., Lilly S. J., Bacon R., Richard J., Conseil S., 2016, MNRAS, 458, 3210

Spergel D. N., Steinhardt P. J., 2000, Phys. Rev. Lett., 84, 3760

Spiniello C., Trager S. C., Koopmans L. V. E., Chen Y. P., 2012, ApJL, 753, L32

Spiniello C., Trager S., Koopmans L. V. E., Conroy C., 2014, Monthly Notices of the Royal Astronomical Society, 438, 1483

Thater S., et al., 2017, A&A, 597, A18

Thomas D., Greggio L., Bender R., 1999, MNRAS, 302, 537

Thomas D., Maraston C., Bender R., Mendes de Oliveira C., 2005, ApJ, 621, 673

Thomas J., et al., 2011, MNRAS, 415, 545

Tinsley B. M., 1968, ApJ, 151, 547

Tortora C., Romanowsky A. J., Napolitano N. R., 2013, ApJ, 765, 8

Trager S. C., Faber S. M., Worthey G., González J. J., 2000a, The Astronomical Journal, 119, 1645

Trager S. C., Faber S. M., Worthey G., González J. J., 2000b, The Astronomical Journal, 120, 165

Treu T., Auger M. W., Koopmans L. V. E., Gavazzi R., Marshall P. J., Bolton A. S., 2010, ApJ, 709, 1195

Vassiliadis E., Wood P. R., 1993, ApJ, 413, 641

Vassiliadis E., Wood P. R., 1994, ApJS, 92, 125

Vaughan S. P., Houghton R. C. W., Davies R. L., Zieleniewski S., 2016, arXiv:1612.00364 [astro-ph]

Vaughan S. P., Davies R. L., Zieleniewski S., Houghton R. C. W., 2018, MNRAS, 479, 2443

Vazdekis A., 1999, ApJ, 513, 224

Vazdekis A., Sánchez-Blázquez P., Falcón-Barroso J., Cenarro A. J., Beasley M. A., Cardiel N., Gorgas J., Peletier R. F., 2010, Monthly Notices of the Royal Astronomical Society, 404, 1639

Vazdekis A., Ricciardelli E., Cenarro A. J., Rivero-González J. G., Díaz-García L. A., Falcón-Barroso J., 2012, Monthly Notices of the Royal Astronomical Society, 424, 157

Vazdekis A., et al., 2015, Monthly Notices of the Royal Astronomical Society, 449, 1177

Vazdekis A., Koleva M., Ricciardelli E., Röck B., Falcón-Barroso J., 2016, Monthly Notices of the Royal Astronomical Society, 463, 3409

Villaume A., Conroy C., Johnson B., Rayner J., Mann A. W., van Dokkum P., 2017, ApJS, 230, 23

Westera P., Lejeune T., Buser R., Cuisinier F., Bruzual G., 2002, A&A, 381, 524

White S. D. M., Rees M. J., 1978, MNRAS, 183, 341

Wilkinson D. M., et al., 2015, MNRAS, 449, 328

Worthey G., 1994, ApJS, 95, 107

Worthey G., Faber S. M., Gonzalez J. J., Burstein D., 1994, ApJS, 94, 687

Young L. M., et al., 2011, MNRAS, 414, 940

Young L. M., et al., 2014, Monthly Notices of the Royal Astronomical Society, 444, 3408

Zhang F., Li L., Han Z., Zhuang Y., Kang X., 2013, MNRAS, 428, 3390

Zibetti S., Gallazzi A., Charlot S., Pierini D., Pasquali A., 2013, MNRAS, 428, 1479

Zieleniewski S., Houghton R. C. W., Thatte N., Davies R. L., Vaughan S. P., 2017, MNRAS, 465, 192

de Zeeuw P. T., et al., 2002, MNRAS, 329, 513

van Dokkum P. G., Conroy C., 2010, Nature, 468, 940

van Dokkum P. G., et al., 2008, ApJL, 677, L5

van Dokkum P., Conroy C., Villaume A., Brodie J., Romanowsky A. J., 2017, ApJ, 841, 68

van der Marel R. P., Franx M., 1993, ApJ, 407, 525